COMPARATIVE MECHANICAL PROPERTY EVALUATION OF ULTRA-HIGH-PERFORMANCE CONCRETE REINFORCED WITH HIGH-STRENGTH STEEL STRAIGHT AND HOOKED FIBERS

by

SUJAN KUMAR SINGH

Presented to the Faculty of the Graduate School of

The University of Texas at Arlington in Partial Fulfillment

of the Requirements

for the Degree of

MASTER OF SCIENCE IN CIVIL ENGINEERING

THE UNIVERSITY OF TEXAS AT ARLINGTON

August 2023

ACKNOWLEDGEMENTS

I would like to express my deepest appreciation to my supervising Professor Shih-Ho (Simon) Chao, for his unparalleled support, guidance, motivation, and encouragement throughout my Master's study at the University of Texas at Arlington. It would never have been possible without his invaluable suggestions and technical supervision. It has been an absolute pleasure and honor to work with him. I want to extend my deepest gratitude to Dr. Surendra P. Shah and Dr. Warda Ashraf for their invaluable time serving my thesis committee.

I would like to sincerely thank Bhupendra Raj Acharya for guiding me at the beginning of my research work. Thanks to Dr. Kyoungsub Park for his continuous guidance and encouragement in my laboratory work. I also had the great pleasure of working with Suman Rijal, Vesal Shakibaie, Rushabh Munot, Chandra Sekhar Cherukuri, Meetkumar Lakhani, Shashidhar R Bontha, Abhishek Odela, Devi Vara Prasad Bitla in some of my research work. I would also like to acknowledge the UTA CELB technician, Mr. Ebner Gary, for the technical support in the lab.

I am deeply grateful to my family for their unrelenting encouragement and support for my decision to pursue an MS degree abroad. Last but not the least, I would like to recognize the help and support of my friends for their everyday call and moral support.

August 2023

ABSTRACT

COMPARATIVE MECHANICAL PROPERTY EVALUATION OF ULTRA-HIGH-PERFORMANCE CONCRETE REINFORCED WITH HIGH-STRENGTH STEEL STRAIGHT AND HOOKED FIBERS

Sujan Kumar Singh, MS

The University of Texas at Arlington, 2023

Supervising Professor: Shih-Ho Chao

This study investigates the tensile properties and ductility of ultra-high-performance concrete (UHPC) reinforced with high-strength steel hooked fibers with a tensile strength of 445 ksi (3,070 MPa) and compares its tensile performance to that of UHPC reinforced with commonly used high-strength smooth steel microfibers with a tensile strength of 2,160 MPa (313 ksi). The research is based on a proprietary mix developed at the University of Texas at Arlington and investigates the mechanical properties of UHPC with varying fiber volume fractions of 1.5%, 2%, 2.25%, and 2.4%. The experimental results indicate that UHPC reinforced with high strength hooked fibers generally exhibits superior tensile strength and ductility compared to UHPC reinforced with straight, smooth steel fibers, except for the 1.5% fiber volume fraction. Moreover, this study examines the improvement of UHPC flowability through the inclusion of specific constituents such as spherical-shaped silica fume, sands, or fly ash. Enhancing flowability is crucial for facilitating the production of UHPC-based SIFCON (UHP-

SIFCON). Additionally, the study investigates the influence of varying curing regimes on UHPC mechanical properties by examining factors like heat treatment temperature (60°C and 90°C) and delay time for heat treatment (immediately after casting or after a 24-hour delay). To determine the tensile strength of UHPC, direct tensile test (DTT) is performed, complemented by the four-point loading flexure test and double punch test (DPT) for comparison purposes. Furthermore, analytical investigations are performed to evaluate the accuracy of the assumptions in the ASTM 1609 beam test standard, while the DPT results are confirmed with the DTT results to ascertain their reliability in measuring tensile response. The outcomes of this study will contribute to the understanding of the mechanical bonding effect of hooked fibers on the tensile performance of UHPC and UHP-SIFCON, as well as contribute to the development of a more reliable testing method for evaluating UHPC properties.

TABLE OF CONTENTS

List of Figures

List of Tables

1 INTRODUCTION

1.1 Background

Ultra-High-Performance Concrete (UHPC) is a novel class of concrete offering superior characteristics such as enhanced tensile strength, improved compressive strength, and heightened durability compared to conventional concrete. The inclusion of fibers in the UHPC mix enhances tensile properties, regulates crack development, facilitates even stress distribution, and improves concrete's ductility and durability. Prior research underscores the critical role that the steel fiber's shape, utilized in the concrete mix, plays in defining its tensile property and ductility. Straight microfibers, owing to their ease of mixing and higher steel volume fraction allowance, are regularly used in the UHPC mixture. Nonetheless, hooked fibers, despite challenges such as fiber entanglement and complex mixing, are perceived to possess advantages over straight fibers. This study aims to scrutinize these assumptions by incorporating hooked fibers into the mix design and comparing their tensile strength with straight fibers. To evaluate the concrete mix's overall performance, a single fiber pullout test is employed, which is critical in this research as it allows for an accurate assessment of the fiber's bonding characteristics within the concrete matrix, ultimately influencing the composite's durability and strength.

The composition of UHPC doesn't adhere to a definite mixed proportion, and its properties largely depend on the constituent materials and their proportions in the mix, aiming for optimal packing density. In this research, a proprietary concrete mixture developed at the University of Texas at Arlington (Aghdasi et al., 2016) was employed as the foundation for all comparisons of mechanical properties. This base mix was subjected

to an array of tests, including compression test, direct tensile test, ASTM beam test (ASTM C1609), and double punch tests (DPT), to thoroughly examine and compare its characteristics. Flowability, a critical factor in Ultra-High-Performance Concrete (UHPC) design, influences the permissible fiber dosage and water-to-cement ratio (w/cm ratio), both of which significantly impact the mix's mechanical properties. Consequently, this study emphasizes the inclusion of spherical-shaped components, such as silica sand and silica fume, as a strategy to enhance the mix's flowability. Also, a preliminary investigation of the impact of silica fume purity on the mechanical properties of the UHPC mixture and flowability was conducted. In the construction industry, situations often arise where the designated strength must be attained earlier in the lifespan of Ultra-High-Performance Concrete (UHPC) due to tight construction timelines. As such, this research focused on enhancing UHPC's compressive strength by using heat treatment as a curing protocol considering factors like curing temperature and the delay before initiating the curing process. Additionally, the study examined the effect of varying curing protocols on the ultimate strength gain at 28 days for a comprehensive comparison.

Assessing the compressive strength of UHPC is straightforward, yet the industry lacks a standard method for determining its direct tensile strength or evaluating the post-cracking stage of Fiber Reinforced Concrete (FRC). The Direct Tensile Test (DTT) is commonly utilized in both academia and industry, but it has limitations such as inconsistencies in specimen gripping, test setup, and crack formation. Despite certain limitations of the Direct Tension Test (DTT), it provides a direct measure of tensile behavior, making it valuable in this research where it is used to compare the tensile properties of straight and hooked fibers. Moreover, its results are cross verified with the ASTM C1609 test and the

Double Punch Test (DPT), as this study aims to ascertain the credibility of these latter tests in accurately determining tensile behavior. The study critically evaluates certain assumptions within the (ASTM C1609, ASTM 2021) formulation, such as linear strain at a section and zero shear between the loading points. The validity of these assumptions is assessed through an analytical investigation. Double Punch Test (DPT) has a simpler test setup and has been demonstrated to accurately measure the tensile behavior of FRC (Mollins et al., 2009, Chao et al., 2011, Pujadas et al., 2012, Blanco et al., 2014). The results obtained from Double Punch Test (DPT) are cross verified with Direct Tensile Test (DTT) to validate its efficacy in correctly measuring tensile behavior.

1.2 Objectives

The objectives of the research are as follows:

1. Compare UHPC reinforced with high strength steel hooked fibers to the commonly used straight steel microfibers.
2. Single fiber pullout performance of the hooked fibers.
3. Initial study of the effect of silica fume purity on flowability and compressive strength of UHPC.
4. Study of the effect of heat treatment as a curing process factoring in elements, like delay time and temperature of curing on the ultimate strength of UHPC.
5. Comparison of tensile strength results from DTT, flexure test, and DPT.
6. Analytical investigation of shortcomings in ASTM standards of the four-point flexure test.

1.3 Organization of Thesis

The thesis is divided into 5 chapters, and they are summarized below.

Chapter 1 provides an introduction and objectives of the thesis.

Chapter 2 defines the literature review on the effect of fiber shape (hooked and straight) on the tensile strength of UHPC, the effect of silica fume purity on mechanical properties of UHPC, effect of heat treatment on the ultimate strength of UHPC and the comparison of four-point flexure loading test (ASTM C1609) and Double Punch Test (DPT) against Direct Tensile Test (DTT). This chapter also includes literature review concerning analytical investigation of the problematic assumptions on the ASTM standard for the ASTM flexure test.

Chapter 3 is the experimental program focusing on the details of the experiment.

Chapter 4 summarizes the test results obtained from the study.

4.1 comparison of tensile strength using hooked and straight fibers. This subtopic also includes a single fiber pullout test of hooked fibers.

4.2 comparison of DTT with the results obtained from flexure test and DPT.

4.3 The study involves the improvement of mechanical properties of the UHPC mix by altering different constituent properties, and the comparison of various curing regimes on mechanical properties of UHPC.

Chapter 5 presents an analytical investigation of the ASTM C1609 beam, challenging its underlying assumptions by scrutinizing the strain diagram, and shear force and moment diagram.

Chapter 6 includes the conclusion of the thesis backed up by experimental and analytical investigation.

2 LITERATURE REVIEW

2.1 Overview of UHPC

Concrete is the most widely used construction material globally, yet it is not without its shortcomings, including relatively low tensile strength and inherent brittleness. These limitations have prompted considerable research into the development of cementitious composites possessing exceptionally high compressive strengths. The end result was the creation of an ultra-high-performance concrete (UHPC).

Initially, efforts to boost compressive strength were centered around the use of specific materials or treatments, such as vacuum mixing, high temperature curing, and high-pressure treatment. However, these approaches eventually paved the way for the development of ultra-high-performance cementitious composites (UHPCCs). Wille et al. (2011) presented a UHPC variant with a compressive strength surpassing 200 MPa (29 ksi), crafted from locally sourced materials and without resorting to a special mixer or heat treatment. Azmee & Shafiq (2018) underlined the foundational principles of UHPC design when they achieved optimal particle packing density, thereby lowering the water-to-cement (w/cm) ratio. They eliminated coarse aggregates for homogeneity and enhanced ductility and crack control through the incorporation of a sufficient volume representing a specific fraction of steel fibers and post-curing heat treatment.

Despite its superior properties, the cost of UHPC remains approximately 20 times higher than conventional concrete, which is priced around \$100/yd^3 (\$130/m^3) (Wille & Boisvert-Cotulio, 2013). Owing to its proprietary nature, stringent quality control requirements, and high material costs, UHPC has seen limited adoption in U.S.

infrastructure projects. Nevertheless, research by Wille & Boisvert-Cotulio (2013) resulted in a nonproprietary mix exhibiting a compressive strength exceeding 22 ksi and incorporating 1.5% steel fibers, thereby reducing the cost of UHPC to $850/yd^3 ($1,110/m^3). Furthermore, research conducted by El-Tawil et al. (2016) unveiled a nonproprietary mix with a compressive strength of 25 ksi costing $266/yd^3 for the cementitious mix, excluding the cost of steel fibers, which approximates to $516/yd^3 for every 1% increase in fiber content by volume.

Table 2-1 Nonproprietary Mix (El-Tawil et al., 2016)

Type	UHPC Ratio	kg/m^3
Cement	1	775
Silica Fume	0.25	194
Water	0.22	165
High Range Water	0.0054	10
Fine Sand I	0.26	245
Fine Sand II	1.03	975

The ACI Committee 239 (2012) first defined UHPC as:

> "Ultra-High Performance Concrete (UHPC) is a "concrete that has a minimum specified compressive strength of 22 ksi (150 MPa) with specified durability, tensile ductility and toughness requirements; fibers are generally included to achieve specified requirements." (ACI Committee 239, 2018;).

In this research, the proprietary mix design developed by Aghdasi et al. (2016) at the University of Texas at Arlington was used to investigate the mechanical properties of ultra- high-performance fiber reinforced concrete (UHP-FRC) further. The mix design was based on optimizing the particle packing density of sand, silica fume, glass powder, fly ash, and cement by selecting particle size ranges and varying the matrix proportions and compositions, as well as the spread value and the amount of entrapped

air. Comprehensive information about UTA-UHPC, including the constituent materials and the mix design, is provided in Chapter 3, Section 3.1 of this thesis.

2.2 The University of Texas at Arlington's (UTA's) Applications of UHPC

Ultra-high-performance concrete (UHPC) is a robust construction material known for its excellent compressive and tensile strength and unique tensile strain behaviors. These qualities enable UHPC to improve the durability and sustainability of various construction components, making it a valuable option in the field. In this chapter, we will delve into the exploration of some applications of UHPC that have been developed at the University of Texas at Arlington (UTA).

Kaka et al. (2016) utilized UHPC's superior compressive strength, high tensile strength, and workability to create intricate non-Euclidean geometries. The resultant branching columnar structures and hexagonal cross sections were cut out using a computer numerical control (CNC) machine. This research opened new avenues for architectural and structural innovation. UHPC's impressive mechanical properties, such as high compressive and tensile strengths and ductility, eliminates the need for conventional reinforcement. Furthermore, the high flowability of UHPC makes it an ideal material for detailed geometric designs. Fig. 2-1 shows the UTA research team successfully showcasing the significant potential of this innovative material.

(a) (b)

Figure 2-1 Load testing at The University of Texas at Arlington's Civil Engineering Laboratory Building (CELB):(a) Column #1 and (b) Column #3 (Kaka et al., 2016)

Kaka et al. (2016) found that UHPC with its elevated compressive ductility can significantly enhance the flexural capacity of structures. This is achieved by allowing a maximum usable compressive strain (ε_{cu}) of 0.015, as opposed to the traditional limit of 0.003 for plain concrete, leading to an increased load-carrying capacity.

Venkatesh & Chao (2018) introduced a novel approach to replace prestressed concrete structures with non-prestressed ultra-high-performance fiber-reinforced concrete (UHPC), circumventing issues associated with prestressed concrete such as high unit costs, camber-related problems, and long-term prestress losses. By exploiting the greater maximum usable compressive strain of UHPC, they demonstrated enhanced flexural capacity, increased cracking resistance, and reduced deflection, culminating in the proposal of a modified deck bulb tee (DBT) girder with comparable cracking resistance to prestressed DBT but without the camber issue.

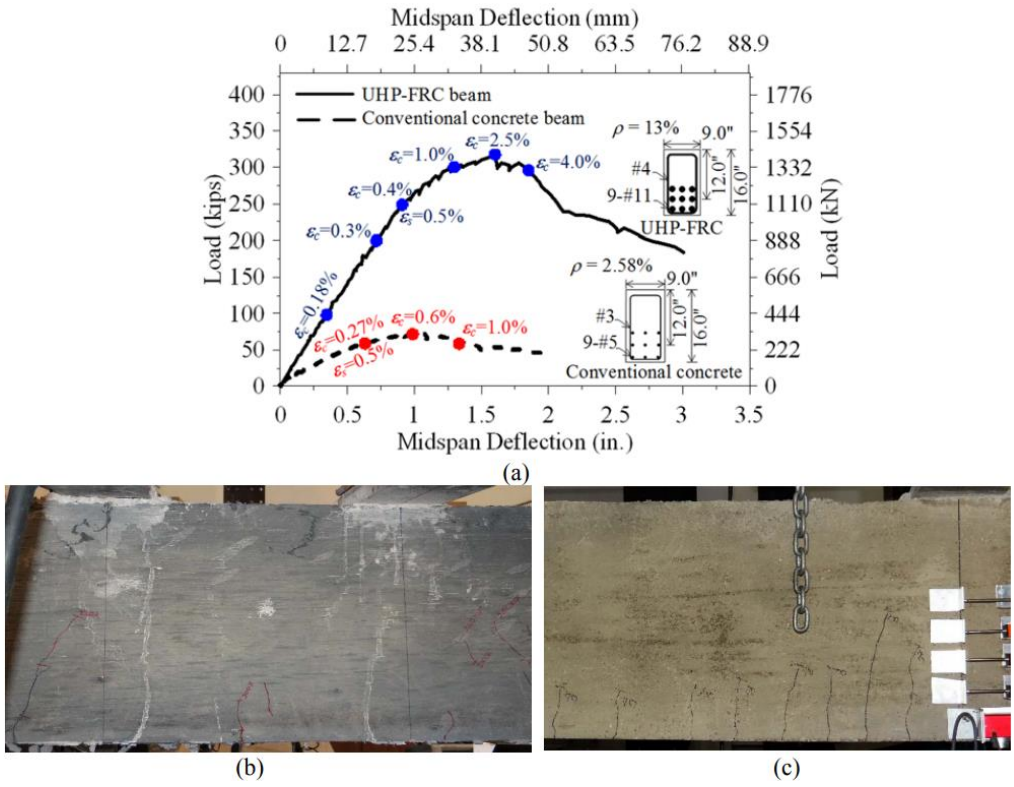

Figure 2-2 (a) Load vs. mid-span deflection responses of RC and UHPC #1 beams, (b) observed cracks in UHPC #1 beam at 300-kip (1334 kN) load, and (c) observed cracks in RC beam at 70-kip (311 kN) load (Venkatesh & Chao, 2018)

In their innovative study, Karmacharya & Chao (2019) explored a novel approach to concrete repair by combining the use of precast UHPC panels with cast-in-place repair of pavements, thereby eliminating the need for dowel bars. They proposed that dowel bars can be effectively substituted with a roughened interface, since the dowels were originally used to prevent faulting even though they contributed minimally to the interface load transfer at peak loads. The method has several advantages over conventional repair techniques, including rapid completion times (overnight as compared to extended closures) and enhanced quality control through precasting. The installation of precast UHPC panels with cast-in-place repair of pavements also reduced labor and

downtime and facilitated faster repairs. This conclusion was based on tests showing an early high early strength of UHPC, and an improved durability leading to decreased life-cycle costs (Karmacharya & Chao, 2019).

Karmacharya et al. (2023) later demonstrated their novel combination of UHPC panels with cast-in-place pavement repair by implementation at Dallas/Fort Worth International Airport. By using a minimal amount of cast-in-place UHPC and excluding the need for dowel bars, increased sustainability and a longer service life of concrete structures is expected. The new method is more cost-effective than conventional cast-in place concrete—about 45 times more effective than the concrete found in a 50-year life cycle.

Figure 2-3 Implementing UHPC precast panels, surface roughening, and onsite UHPC joint grouting (Karmacharya et al., 2023)

UHPC introduces innovative solutions for the construction of earthquake-resistant structures because of its exceptional mechanical properties (i.e., enhanced compressive and shear strength, improved ductility, and superior bonding and confinement characteristics). The inclusion of high-strength steel microfibers mitigates the issue of congestion typically associated with high-strength concrete. The microfibers also promote ductility, and maintain self-consolidation. Chao et al. (2021) conducted cyclical

loading tests on column and beam specimens made of both conventional reinforced concrete (RC) and UHPC. The differences in traditional RC and UHPC provided a stark contrast based on their performance. Remarkably, the column test produced no visible concrete damage in the plastic hinge region of the UHPC columns throughout the tests, thereby enabling the ultimate yielding capacity of the longitudinal reinforcement without buckling. The beam test for RC beam specimens showed severe cracking due to high shear demand and the relatively weak shear capacity of conventional concrete, resulting in degradation of the concrete's confinement and shear resistance. In contrast, UHPC beam specimens remained almost undamaged up to high drift ratios even in the absence of transverse reinforcement. These results indicate a change that could be brought into the seismic design provisions as defined by ACI 318 (2019) when UHPC is utilized. Specifically, there could be a reduction in confining requirements and the amount of transverse reinforcement necessary for columns constructed with concrete demonstrating a compressive strength above 10,000 psi (70 MPa).

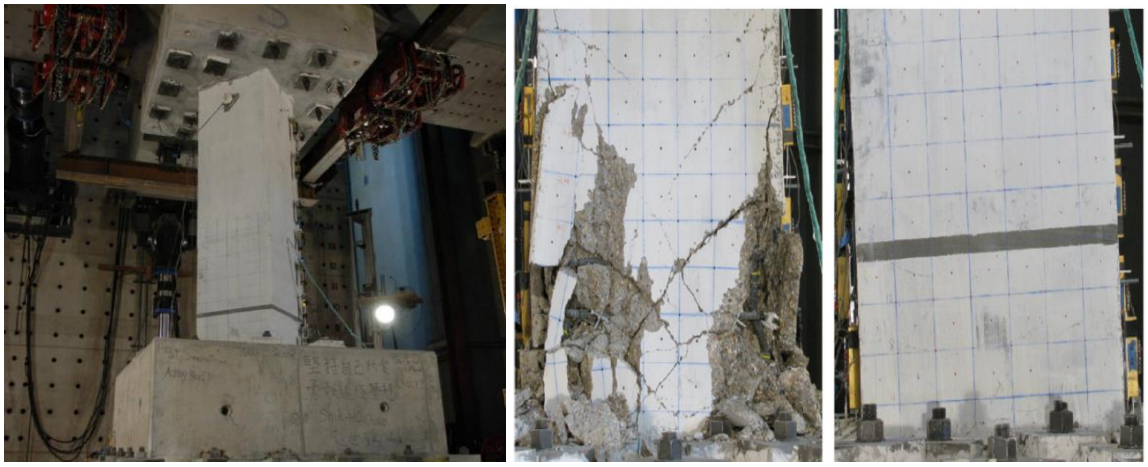

(a) (b) (c)

Figure 2-4 (a) UHPC specimen before testing and (b) extent of damage for RC column and (c) extent of damage for UHPC column at 5.25% drift (Chao et al., 2021)

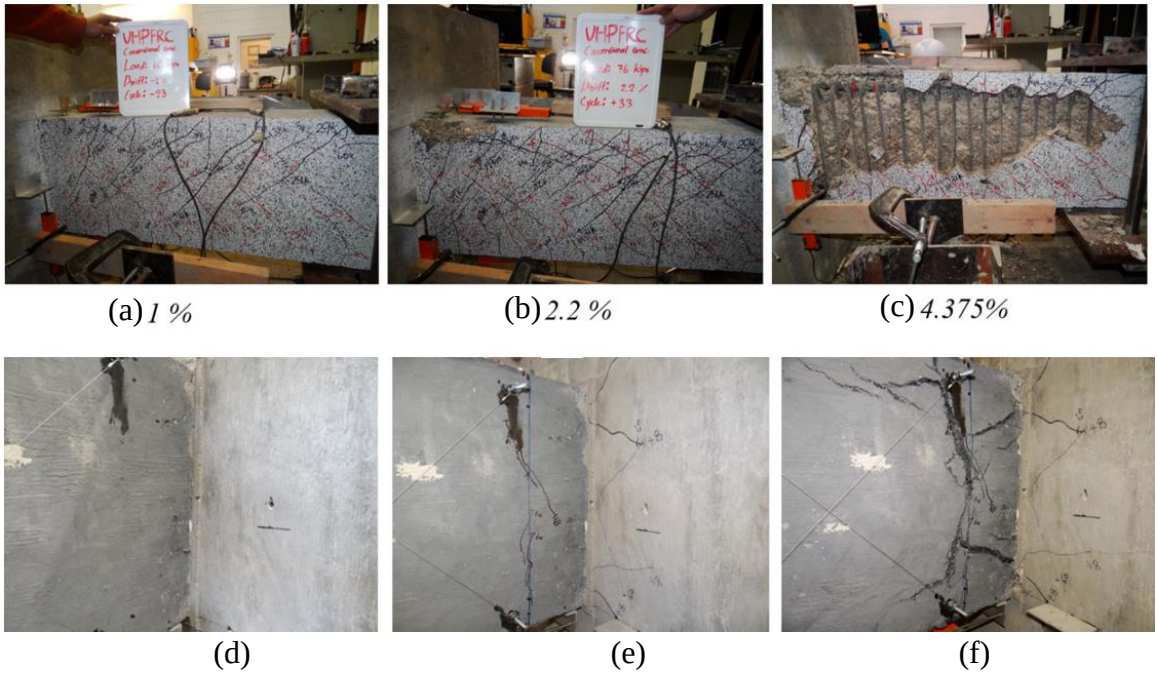

(a) *1 %* (b) *2.2 %* (c) *4.375%*

(d) (e) (f)

Figure 2-5 Comparison of damage patterns between RC specimens (a)-(c) and UHPC beams shown in (d)-(f) (Chao et al., 2021)

2.3 Compressive strength of UHPC

Unlike conventional concrete, which has definitive mix proportions, ultra-high-performance concrete (UHPC) does not adhere to a specific mix design for its mechanical attributes. Instead, the compressive strength of UHPC is largely affected by packing density, which is dictated by the mix proportions and the materials incorporated into the mix. Notably, UHPC tends to exhibit remarkable compressive strength, typically surpassing 120 MPa (17.4 ksi) (Zhang et al., 2018). It is important to recognize that as the compressive strength of UHPC increases, so does its brittleness. To counteract this brittleness and to boost tensile strength, fibers are added to the UHPC mix. However, the inclusion of fibers does not have a significant impact on compressive strength. For

example, decreasing the volume fraction of steel fibers from 2% to 1.5% only resulted in a marginal 5% reduction in compressive strength (Tai & El-Tawil, 2020).

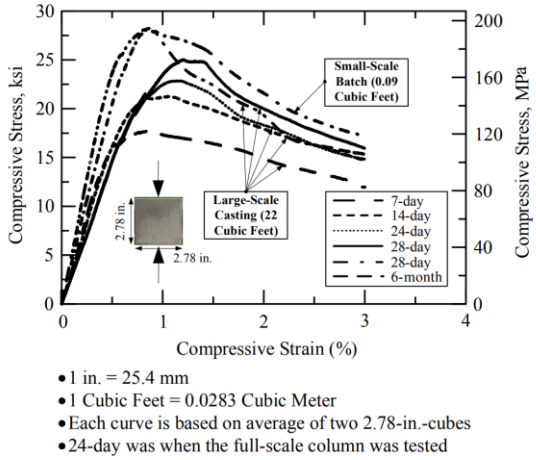

Figure 2-6 Compressive stress-strain curves for UHPC specimens (Aghdasi et al., 2016)

Figure 2-6 shows the compressive stress-strain curve of different UHPC mix developed at UTA research (Aghdasi et al., 2016).

We conducted a compressive strength test on UHPC mixes with variable fiber content and different fiber shapes. These tests helped establish a more comprehensive understanding of how compressive stress and compressive strain affects the overall mechanical behavior of UHPC.

2.4 Material Composition

UHPC formulation involves a precise combination of materials. In this case, the materials are: cement, sand, silica fume, fly ash, glass powder, superplasticizer, and water. These materials are part of the mix design integrated in specific proportions and based on a proprietary formulation developed at the University of Texas- Arlington. According to Haber et al. (2018), there exists no universally accepted definition for ultra-high-

performance concrete (UHPC), and the mechanical properties of UHPC exhibit variations contingent upon the specific types of constituent materials employed.

Two significant scenarios have been probed in recent research. First, the impact of the purity of silica fume on the mechanical characteristics of the UHPC mixtures was explored. Silica fume is known to be a substantial component in UHPC, especially since its purity can potentially affect the performance of the concrete. Second, a comparative analysis was conducted between two different types of fine sand based on their separate abilities to facilitate UHPC flowability, which is an important UHPC property. Insufficient flowability in concrete can lead to defects and adversely affect its strength and durability. To enhance flowability while maintaining strength, researchers have explored an additional approach involving the shape of component particles. In the UHPC mix, both sands and cement typically consist of angular particles. However, introducing sand particles with a more spherical shape promotes roll over during the mixing stage. This roll-over effect reduces inter-particle friction and facilitates improved flowability by allowing the particles to move more easily. Consequently, the overall flowability of the concrete mixture is enhanced.

2.4.1 Effect of Silica Fume Purity on UHPC Mix

Because of silica fume's extremely fine particles (1/100 the size of a cement grain), it is commonly utilized in UHPC mixtures to effectively fill the voids between larger particles within the UHPC matrix (Hanson, 2017). Its incorporation improves both the mechanical and durability properties of concrete (Li et al., 2022). Furthermore, the addition of silica fumes to hardened concrete enhances its impermeability, resulting in a reduced permeation of fluids (Ramezanianpour et al., 2013). ASTM C1240-20 regulates the use

of silica fume in concrete mixtures by requiring a silicon dioxide content of 85% (ASTM C1240, 2020). Several research studies have investigated the impact of silica fumes on UHPC properties. Carey et al. (2022) conducted a study exploring the effects of silica fume purity (percentage of silicon dioxide) on thermal setting time, maximum temperature generated during hydration, and compressive strength. Additionally, they observed a statistically significant interaction between the concentration of silicon dioxide (SiO_2) and the water-to-cementitious materials ratio (w/cm) based on the concrete's mechanical properties, which is the basis for further study on silica fume purity.

In this paper, we present a preliminary study investigating the impact of three different silica fumes with varying levels of purity on the flowability and compressive strength of UHPC. The aim is to further elucidate the relationship between silica fume characteristics, especially purity and UHPC performance.

2.5 Tensile Strength of UHPC Mix

UHPC exhibits distinct mechanical properties that set it apart from conventional concrete. Notably, UHPC demonstrates high tensile strength, strain hardening, and post-cracking behavior, surpassing that of traditional concrete (Qi et al., 2016). Typically, the tensile strength of UHPC is two to three times greater than that of conventional concrete.

For example, Wille et al. (2011) achieved a tensile strength of 2.9 ksi (20 MPa) using steel fibers with a volume fraction of 3%, while Aghdasi et al. (2016) reported a tensile strength of 1.21 ksi (8.3 MPa) in different UHPC matrices. This enhanced tensile strength was achieved through fiber reinforcement and contributed to crack control under service

conditions, while providing tensile ductility during strength (Villavicencio & Sebastian, 2021).

The presence of fibers in UHPC mixtures plays a crucial role in improving crack resistance and enhancing tensile ductility. These characteristics not only increase material tensile strength but also allow optimization of structural design in ways that are not feasible with traditional concrete.

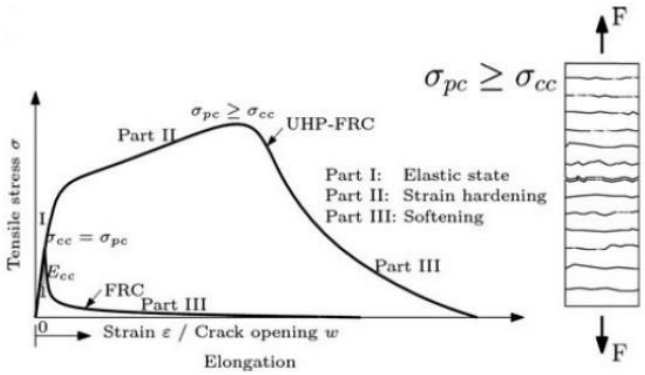

Figure 2-7 UHPC tensile stress-strain curve under three states and multiple cracking (Wille et al., 2011)

UHPC possesses exceptional mechanical properties, particularly in terms of sustained post-cracking tensile strength. However, quantifying this tensile property has presented challenges, as there are no standardized methods for conventional concrete. There is, however the ASTM E8/E8M for structural steel. When it comes to directly evaluating the tensile strength of concrete, no standard exists due to the relatively low tensile strength of conventional concrete.

Several methods have been proposed for assessing tensile strength. The flexural bending test and the split tensile test have been used to evaluate the tensile performance of traditional fiber-reinforced concrete (Choi & Yuan, 2005). However, the indirect nature

of these methods raises concerns about overestimating the peak tensile strength (Nilson et al., 2010).

To address the need for direct tensile strength assessment, the uniaxial tensile test has been employed. Since no standard testing method for fiber reinforced concrete exists, the mold shape and testing method developed by Chao et al. (2011) were utilized for the direct tension test (DTT). Nonetheless, direct tension tests have drawbacks that can yield variable results due to eccentricity, secondary bending moments, and other factors (Zheng et al., 2001).

Both the split tensile test and flexural test are indirect measures of tensile strength, as specimens are not purely subjected to tension, resulting in overestimated values due to relative rotation and complex stress states. The response of the uniaxial direct tensile test reflects the behavior of an FRC member under direct tension or pure shear (diagonal tension), while the responses of the third point loading bending test indicate the behavior of members under uniaxial and biaxial bending (Chao et al., 2011). Comparing these two methods directly does not lead to a proper conclusion due to the different load-carrying mechanisms involved.

Moreover, both the uniaxial direct tensile test and the third point loading bending test exhibit high coefficients of variation in their post-cracking responses due to the lack of crack control position and uneven fiber distribution. To obtain reliable results and reduce variations in testing, a more precise testing procedure for fiber-reinforced concrete materials is required.

In this thesis, a comparison between the direct tensile test (DTT), double punch test (DPT), and ASTM C1609 beam flexural test has been conducted to assess their suitability

for evaluating the post-cracking performance of UHPC and to achieve more reliable and consistent results.

2.6 Direct Tensile Test for UHPC

While ASTM standards for direct tensile tests on concrete are not available, recommendations from organizations such as the Federal Highway Administration (FHWA) and the Japan Society of Civil Engineers (JSCE) offer guidelines on conducting uniaxial tensile tests. These guidelines are provided by Graybeal & Baby (2019) for FHWA and JSCE (2008), and they both outline procedures for performing a direct tensile test.

The primary advantage of a direct tensile test is that it eliminates the need for backward calculation of material tensile response. Instead, it provides a comprehensive representation of the material's tensile behavior across all stages, as illustrated in in Figure 2-8. This direct assessment of tensile behavior is a valuable aid to understanding the performance of the tested concrete material.

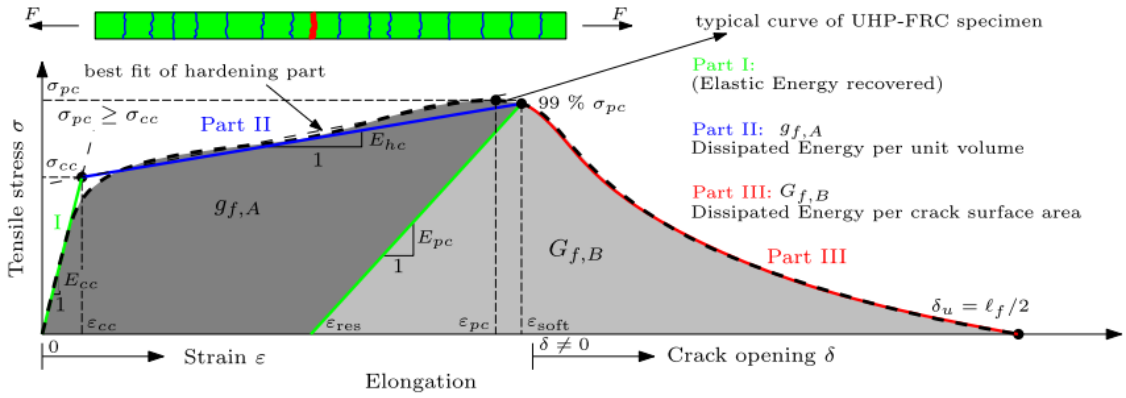

Figure 2-8 Strain hardening tensile response of the UHPC (Wille et al., 2014)

2.6.1 DTT setup and results for UHPC

The direct tension test faces challenges in achieving uniformly distributed stresses across the cross-section and maintaining a stable load versus displacement response (Wille et al., 2014). Two factors affect the tensile response observed in the three parts of the stress-strain curve. They are: 1) boundary conditions (fixed or rotating) and 2) specimen shape (e.g., dog bone-shaped, notched) (Naaman et al., 2014). To capture the strain-hardening behavior accurately, a dog bone-shaped specimen is considered more effective (Wille et al., 2014). Researchers have employed adhesives to simulate fixed support conditions, but this approach often leads to non-uniform failure due to local stress concentrations near the adhered surface.

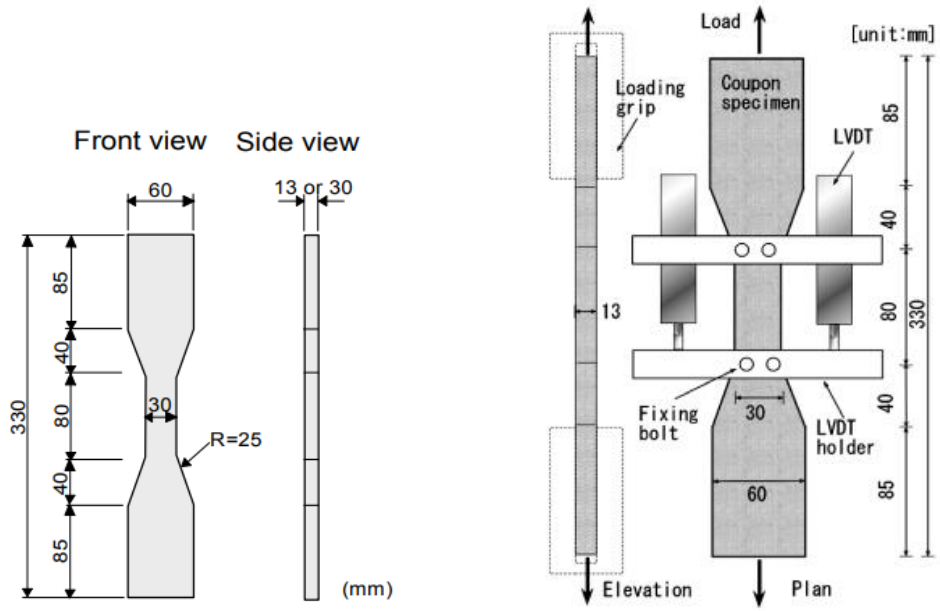

Figure 2-9 Test specimen and the setup for DTT (JSCE, 2008)

Graybeal & Baby (2013) employed two types of prismatic specimens with 2 $in.^2$ cross-sections. These specimens differ in length. The one on the left is 12 inches long and the one on the right is 17 inches long. Both specimens contained a fiber volume of 2%. The longer specimen length was recommended over the shorter one due to the reduced magnitude of bending stress imparted during the initial gripping stage.

Two types of fibers were used in this study: One type had a length of 13 mm (0.5 inches) and a diameter of 0.2 mm (0.008 inches), while the other type had a length of 20 mm (0.8 inches) and a diameter of 0.3 mm (0.012 inches). These variations in fiber length and diameter helped the research team to determine their effect on the tensile behavior of the UHPC specimens.

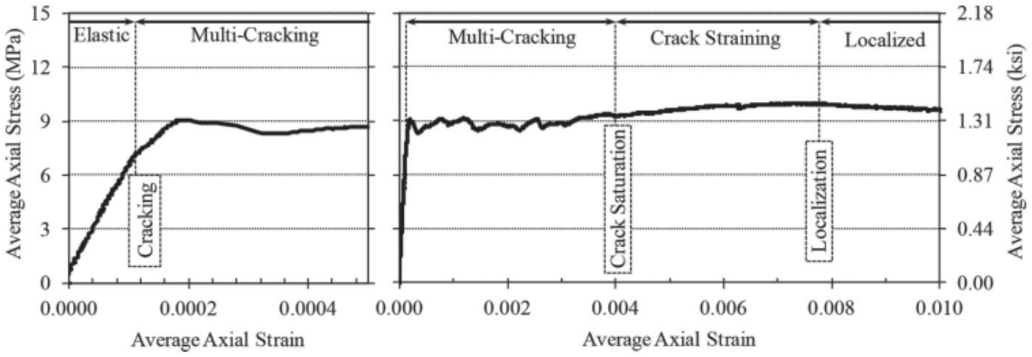

Figure 2-10 Uniaxial tensile stress-strain response (Graybeal & Baby, 2013)

The Federal Highway Administration (FHWA) undertook a comprehensive project to evaluate various test methods for measuring tensile strength, as reported by Graybeal & Baby (2019). The FHWA study adopted an experimental setup similar to a previous research effort conducted by Graybeal & Baby (2013). Specifically, the FHWA project

involved conducting 43 direct tension tests (DTTs) using the same configuration and parameters as described in the earlier Graybeal & Baby (2013) study.

(a)

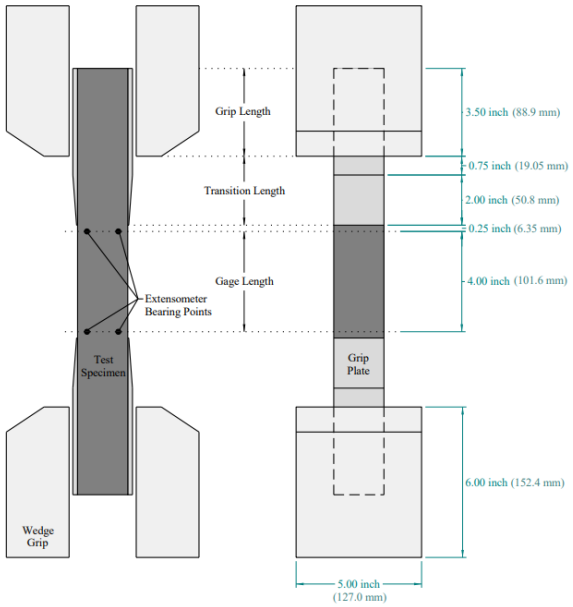

Source: FHWA.

(b)

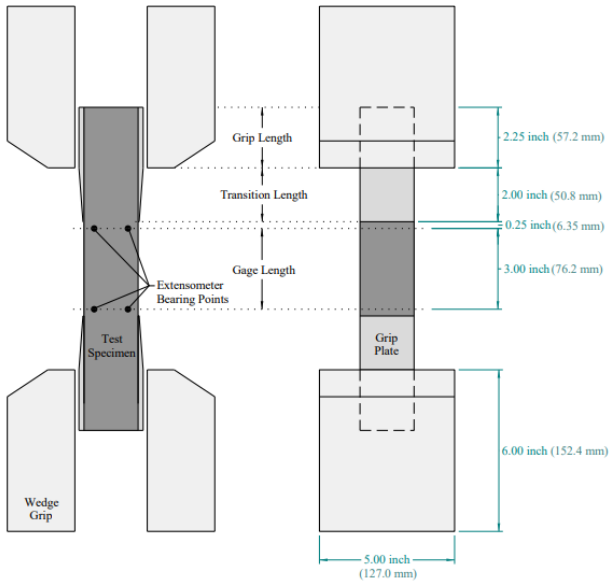

Source: FHWA.

Figure 2-11 DTT setup from FHWA direct tensile specification: (a) a 17-inch specimen and (b) a 12-inch specimen (Graybeal & Baby, 2019)

The DTTs conducted by (Graybeal & Baby, 2019) revealed impressive mechanical properties for the tested UHPC specimens. The elastic modulus exceeded 54 GPa (7,832 ksi), indicating the material's stiffness and ability to withstand deformation under tensile forces. The tensile cracking strength surpassed 7.6 MPa (1.1 ksi), highlighting the concrete's resistance to crack initiation. Moreover, the maximum tensile strength exceeded 8.3 MPa (1.2 ksi), demonstrating its ability to withstand high tensile stresses. The UHPC specimens also exhibited a significant tensile strain at crack localization, surpassing 0.0034, indicating its ductile behavior and capacity to sustain deformation even after cracking. These results show the exceptional mechanical properties of the tested UHPC, highlighting its potential for structural applications requiring high strength and durability.

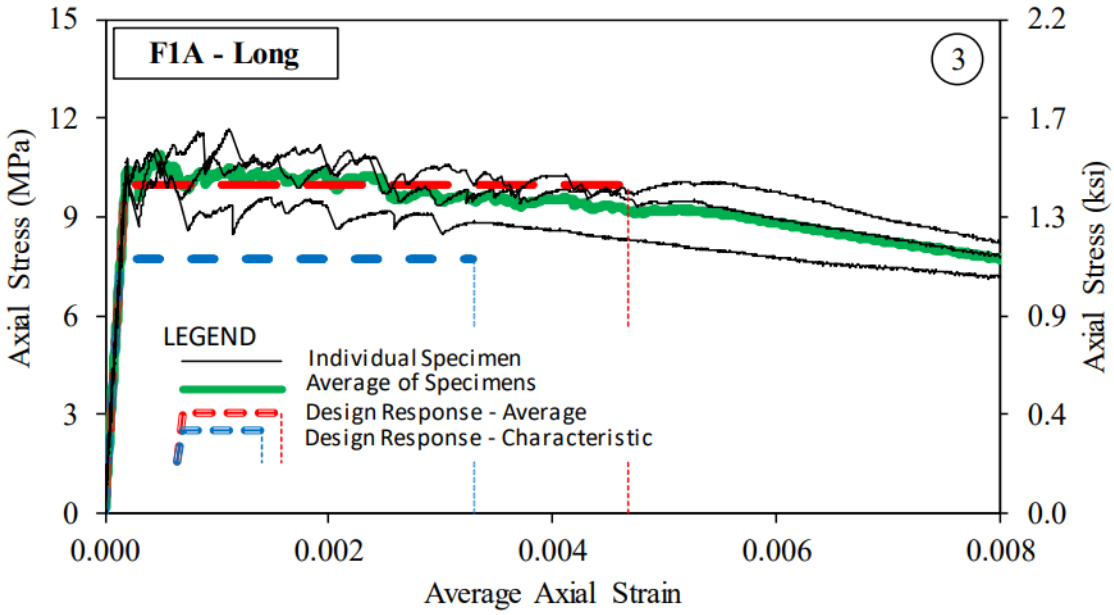

Source: FHWA.

Figure 2-12 DTT stress-strain results after testing 17-inch specimen (Graybeal & Baby, 2019)

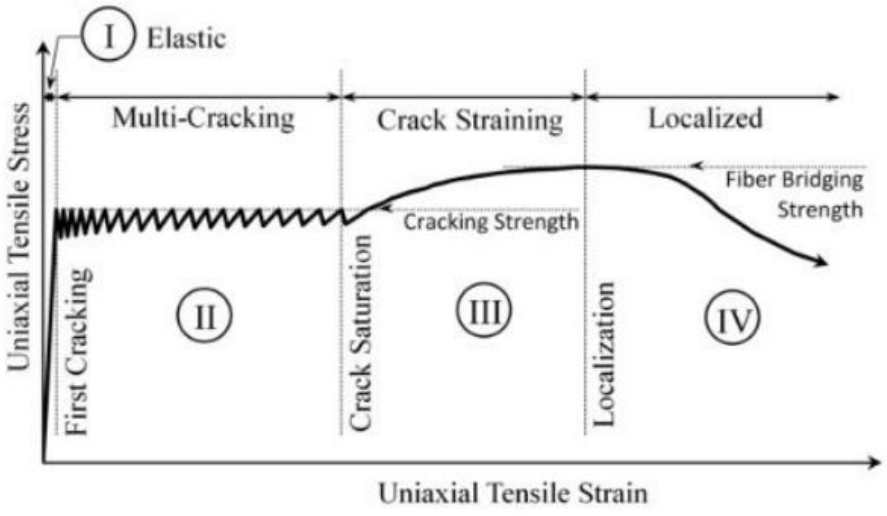

Figure 2-13 Idealized tensile response for UHPC.

The uniaxial tensile response of UHPC is segmented into four primary stages. Initially, in the elastic phase, strain is exerted on the cement-based composite until the occurrence of the first crack. This is followed by the multicracking phase where stress remains stable while multiple cracks are observed. This continues until the initiation of the crack-straining phase, which is marked by a slight escalation in stress as pre-existing, individual cracks broaden. The final stage, referred to as the localization phase, begins when an individual crack starts to expand, and is characterized by the debonding and pull-out of fibers from the matrix.

Qiao & Zhou (2018) employed the finite element analysis (FEA) model to adapt a dogbone-shaped specimen, ensuring an appropriate tensile response in all phases (i.e., the elastic, multicracking, crack straining, and localized stages). The middle section of their specimen boasted a 2-inch square cross-section and a gauge length of six inches. As per the findings of Nguyen et al. (2014), a slight decrease occurs in tensile strength as the gauge length of the central portion increases. Despite UHPC generally being considered a homogeneous material, it is actually an inhomogeneous composite. Consequently, a

longer specimen, being more susceptible to defects, flaws, and subsequent failure, tends to demonstrate lower tensile strength. The ASTM C1609/C1609M-19a, 2019 specification (ASTM, 2019) necessitates that the specimen's width and depth exceed three times the fiber length. Using a similar assumption for the direct tensile test, using 30 mm (1.18 in.) fibers in the test justifies a 4-inch width.

Wille et al. (2011) proposed that superior tensile strength and strain capacity could be achieved even with a lower fiber content. This can be attained using deformed steel fibers (hooked and twisted), as opposed to short, straight steel fibers. The specifics of the specimen and the type of steel fibers they employed for their DTT are listed in Table 2-2.

Table 2-2 Fibers used in the study and their properties (Wille et al., 2011)

Notation	Form	Number of twists	d_f (mm)	ℓ_f (mm)	ℓ_f/d_f	Tensile strength (MPa (ksi))
S	Straight (S)	0	0.20	13	65	≈2600 (377)
H	Hooked (H)	0	0.38	30	79	≈2900 (420)
T_1	High twisted (T_1)	16	0.30[a]	30	100	≈2100 (304)
T_2	Low twisted (T_2)	6–8	0.30[a]	30	100	≈3100 (449)

[a] Manufactured out of round wire with $d_f = 0.30$ mm, shaped into prism a/b = 0.24/0.30 mm

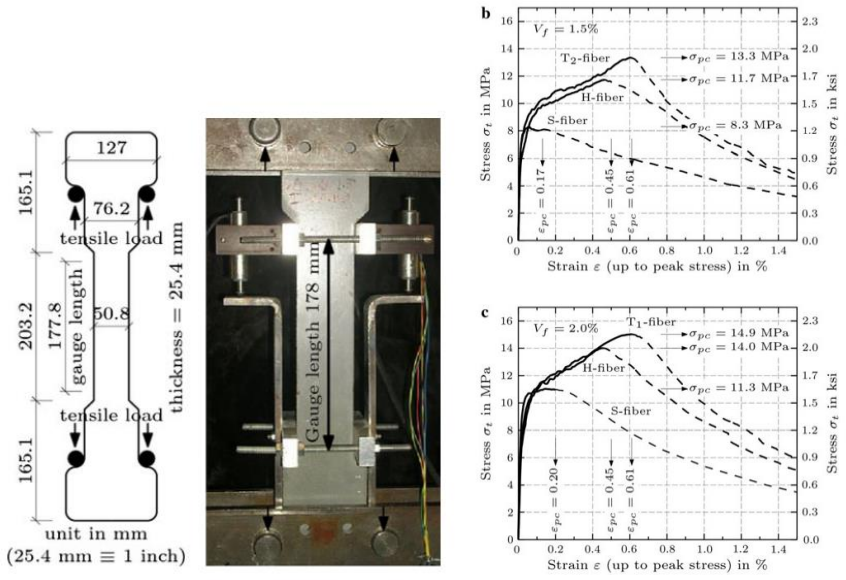

Figure 2-14 Test setup and DTT response of UHPC (Wille et al., 2011)

Wille et al. (2014) identified only minor variations in tensile strength, notwithstanding their use of diverse fiber shapes such as hooked, straight, and twisted steel fibers. It is postulated that these minimal differences could be attributed to the smaller size of the specimens tested. The specific test setup and the types of fibers used are in Table 2-2 on the previous page.

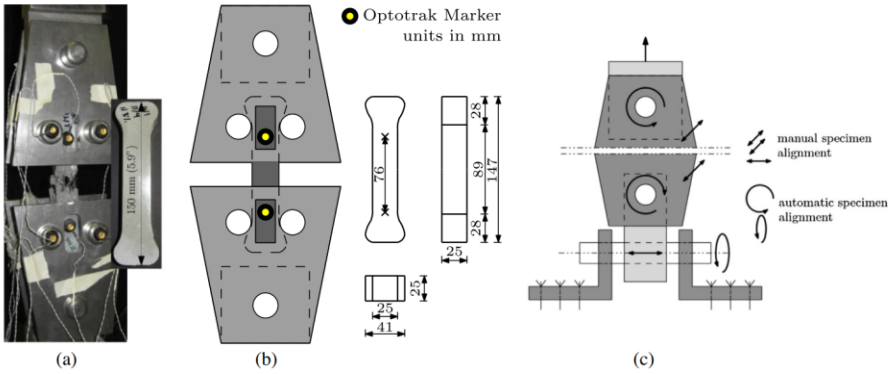

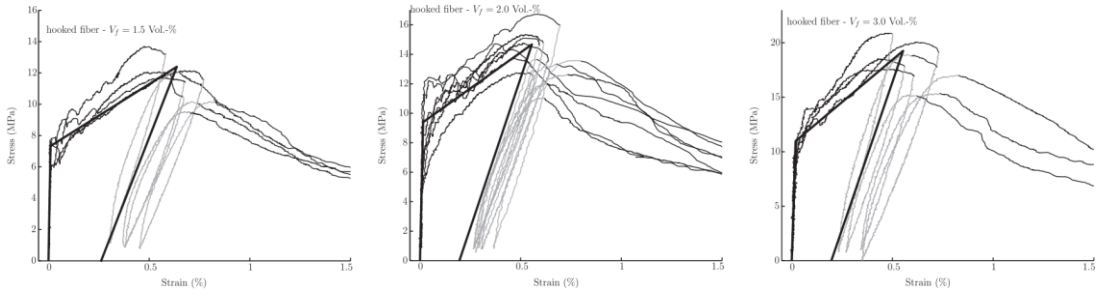

(a)

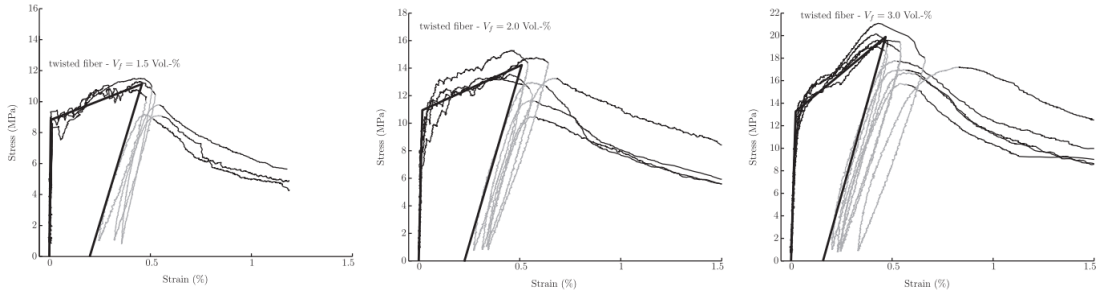

(b)

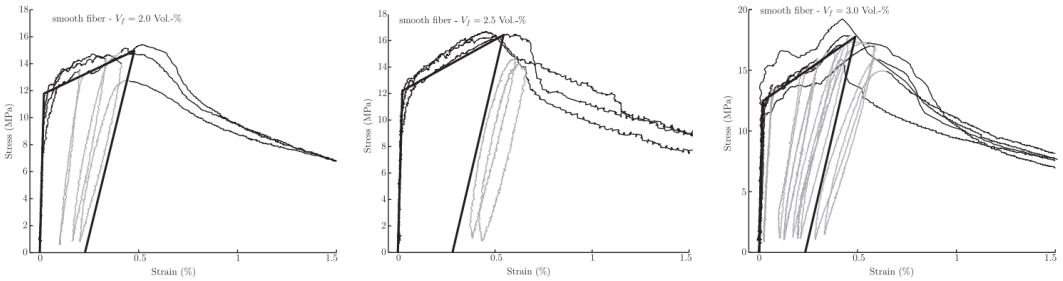

(c)

Figure 2-15 DTT specimens' tensile response with (a) hooked, (b) twisted, and (c) smooth steel fibers (Wille et al., 2014)

The bulk of the preceding research relied heavily on small-scale tensile tests, which may not authentically depict the realistic behavior of UHPC members used in construction. In light of this, Aghdasi et al. (2016) conducted large-scale tensile tests to examine the actual tensile behavior of the UHP-FRC members.

In their experiment, Aghdasi et al. (2016) utilized short straight microfibers, 12.5 mm (0.49 in.) in length and 0.175 mm (0.007 in.) in diameter, and twisted microfibers, 14 mm (0.55 in.) in length and 0.5 mm (0.02 in.) in diameter. The larger tensile specimen used had a cross-sectional area of 16 in^2, which is eight times larger than the one used by Wille et al. (2011). Additionally, they cast a specimen with a smaller cross-sectional area of 2 in^2 to observe any possible effects on specimen size.

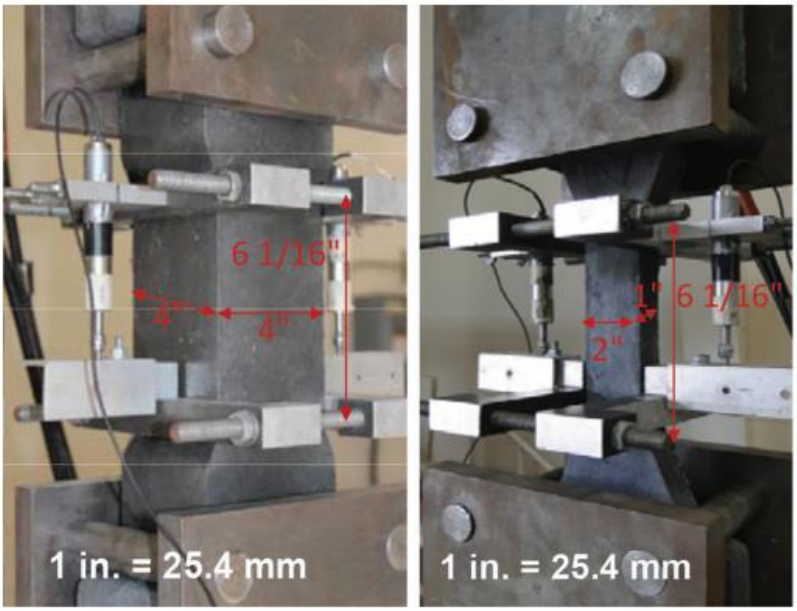

Figure 2-16 Tensile specimen: (a). Large-scale (16 in^2) and (b) small-scale (2 in^2) (Aghdasi et al., 2016)

Aghdasi et al. (2016) uncovered a critical finding revealing that the dimensions of the test specimen significantly affected the tensile strength and ductility measurements of UHPC specimens subjected to direct tensile tests. They cautioned that tensile strength data obtained from smaller test specimens should be applied to larger structural members with care, given the disparities observed during the study. Specifically, their results indicated that smaller-scale specimens demonstrated substantially higher tensile strength, exhibiting increases between 30 and 60% compared to larger-scale specimens, and these smaller specimens displayed a moderate increased hardening response.

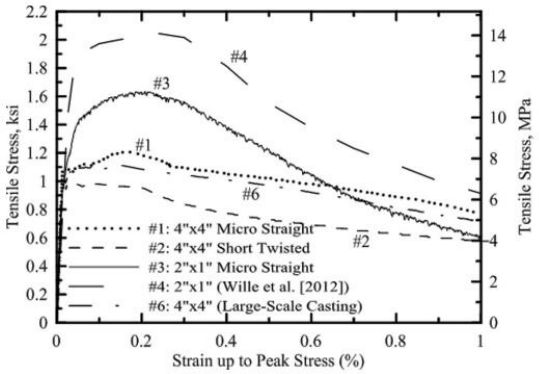

Figure 2-17 DTT tensile response of UHPC (Aghdasi et al., 2016)

In the absence of a standardized method for conducting direct tensile tests, Qiu et al. (2022)undertook a comprehensive approach, testing six different setups. However, they primarily employed Method VI, utilizing a dogbone-shaped specimen with a cross-sectional dimension of 100 × 50 mm (3.94 × 1.97 in.) and a gauge length of 200 mm (7.87 in.). Because this method is more refined, it can address the limitations inherent in other test methods and has been used to elucidate the tensile responses of UHPC.

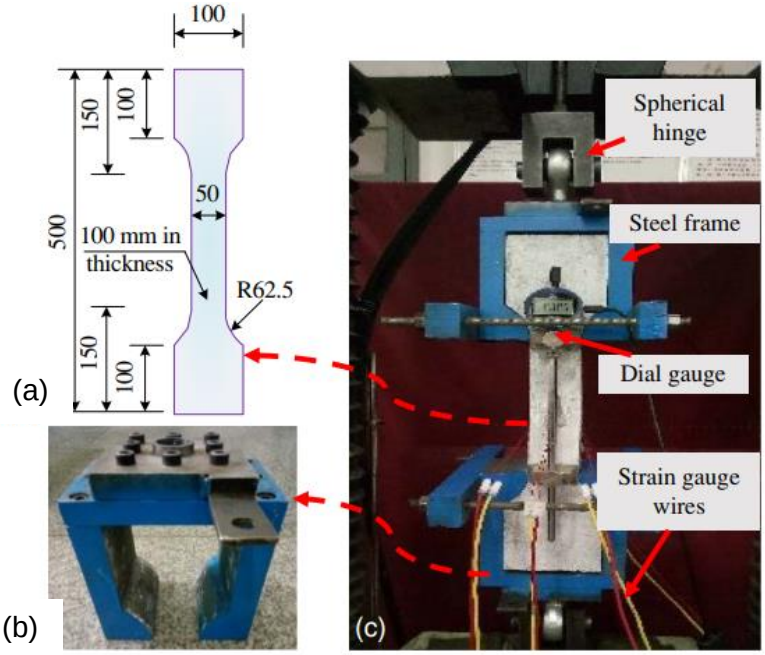

Figure 2-18 Method VI test setup (Qiu et al., 2022) (a) specimen dimensions (mm), (b) special steel frame, and (c) Method-VI specimen assembly in testing machine

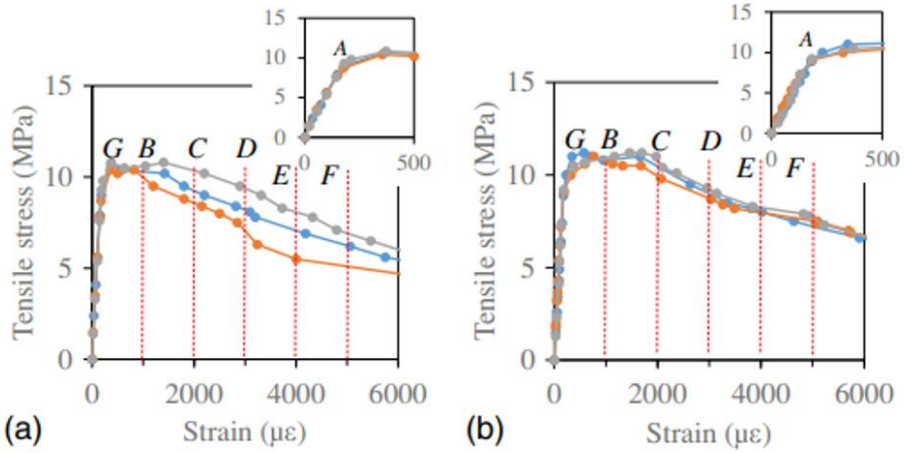

Figure 2-19 Tensile stress-strain relationships for steek hooked fibers in UHPC with varying fiber lengths (Qiu et al., 2022)

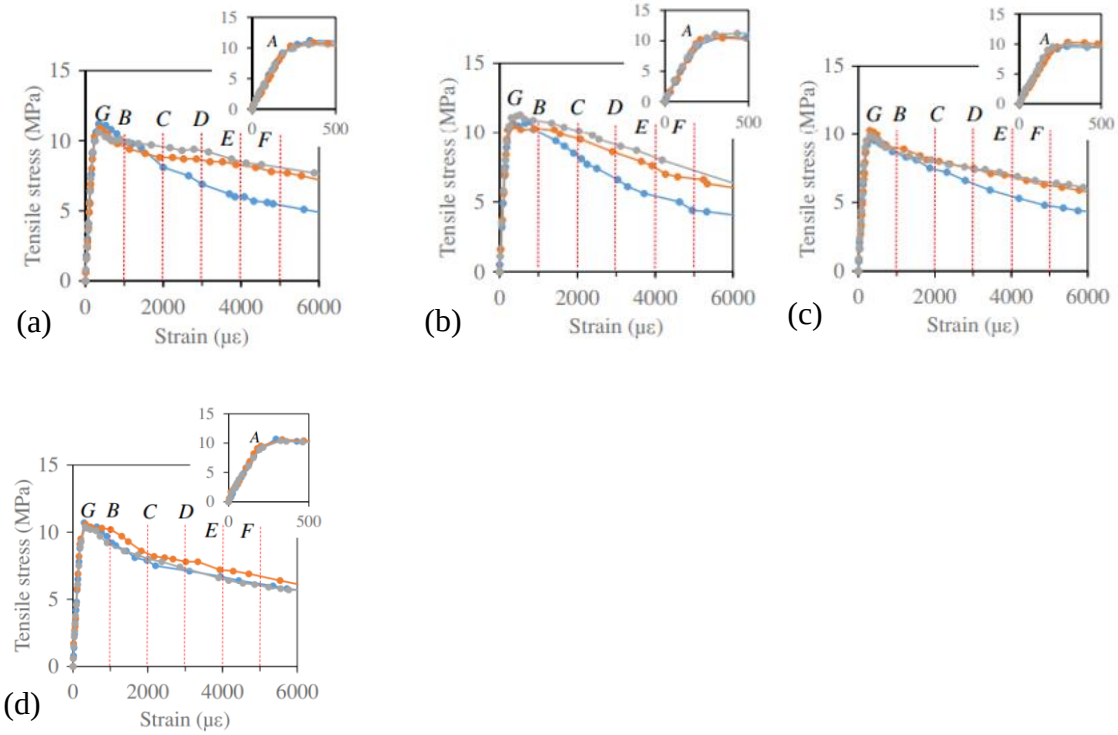

Figure 2-20 Tensile stress-strain relationships for straight steel fibers in UHPC with varying fiber lengths (Qiu et al., 2022)

Table 2-3 Steel fibers used in Qiu et al. (2022) study.

Tensile specimens		Fiber type	Volume content (%)	Lengh × diameter (mm)	Aspect ratio	Density (kg/m^3)	Tensile strength (MPa)	Elastic modulus (GPa)
Method-V	Method-VI							
EH-A	H-A	Hooked end	2	13 × 0.22	59	7,850	>2,000	200
EH-B	H-B	Hooked end	2	13 × 0.2	65			
ES-A	S-A	Straight	2	13 × 0.22	59			
ES-B	S-B	Straight	2	13 × 0.18	72			
ES-C	S-C	Straight	2	13 × 0.15	87			
ES-D	S-D	Straight	2	20 × 0.2	100			
EM-A	M-A	Straight	0.4	8 × 0.12	67			
		Straight	1.6	13 × 0.15	87			
EN	N	No	0	—	—	—	—	—

Note: E = Method-V; H = hooked-end steel fibers; S = straight steel fibers; M = hybrid fibers; N = no fiber; and A, B, C, and D = steel fibers with different aspect ratios.

Qiu et al. (2022) observed that the usage of hooked steel fibers appeared to create a more pronounced strain-hardening platform compared to straight fibers, primarily due to the mechanical anchorage provided by the hooked fibers. In terms of first crack strength, all the specimens fell within a range of 0.4 MPa (58 psi). Nevertheless, the inclusion of steel fibers led to an increase in peak strength by 19 to 25% for hooked fibers and 11 to 22% for straight fibers when compared with the plain concrete specimens.

In general, concerning the impact of different types of steel fibers on UHPC tensile strength, the specimens with hooked end fibers showed higher residual tensile stress (about 0.2 MPa (29 psi) at the same crack width) than the straight fiber specimens at the same aspect ratio of fibers. Regardless of whether the fibers had a hooked or straight end, an increase in the aspect ratio of fibers from 59 to 72 resulted in an approximate rise of 3.0% to 3.9% in residual tensile stress at the same crack width. Conversely, a rise in aspect ratio from 72 to 100 led to a drop in residual tensile stress by 9.6% for straight fibers only. The ductility ratio and characteristic stress increased when the aspect ratio of the hooked end fibers increased, but this was not observed in the case of straight fibers.

The mold and setup used for the test specimens were in accordance with the specifications laid out by Chao et al. (2011). This choice was made due to the advantages offered by the pin-pin loading condition, which helps achieve pure axial load in tension.

Furthermore, this setup confined cracking to the central portion due to the arrangement of the steel mesh.

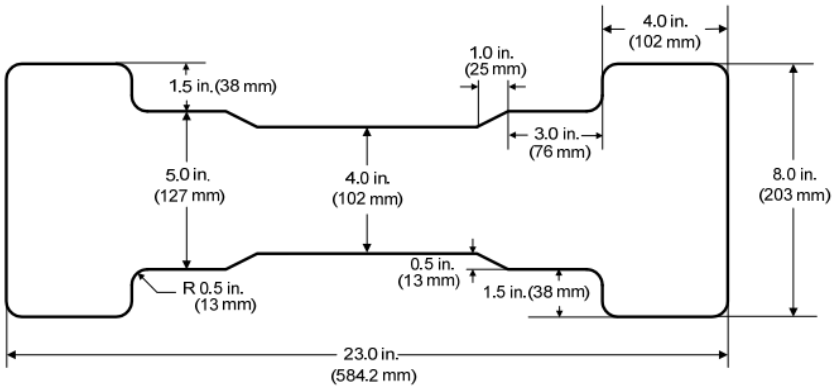

Figure 2-21 Direct tension test (DTT) mold used in this study

2.6.2 DTT comparison between hooked and straight fibers

UHPC is known for its high compressive strength, which leads to a brittle nature. As a means of offsetting this characteristic, fibers are incorporated into UHPC to improve tensile strength and augment strain-hardening behavior in tension, thereby transforming brittle failure into ductile failure (Nematollahi et al., 2012). While a considerable number of tensile tests have been conducted for UHPC, there remains a deficit in research specifically when comparing the impact of different fiber shapes in UHPC mixtures using DTT.

Wille et al. (2011) reported that deformed (hooked and twisted) steel fibers demonstrated superior tensile strength and strain capacity when compared to short straight steel fibers. Interestingly, despite the use of hooked, straight, and twisted fibers, Wille et al. (2011) noted minimal variations in tensile strength. Subsequent research by Qiu et al. (2022), involving a direct tensile test on dogbone specimens, led to the conclusion that hooked fibers achieve a more discernible strain-hardening platform than straight fibers, based on

their mechanical anchorage. Their findings also indicate that hooked fiber specimens display a higher residual tensile stress than straight fiber specimens by about 0.2 MPa (29 psi) at the same crack width, given the same ratio of fibers.

Given the limited body of research contrasting the effects of hooked and straight fibers as observed in DTT, the primary focus of this thesis lies in this underexplored area.

2.7 Beam-type test

The direct tension test (DTT) is a direct form of tensile testing, yet in the absence of a dedicated ASTM standard for DTT, alternative testing methods are commonly employed to examine the tensile strength of UHPC. The flexure beam test serves as one such indirect approach to tensile testing. This test method was conducted following the ASTM C1609/C1609M-19a Standard Test Method for Flexure Performance of Fiber-Reinforced Concrete (Using Beam with Third-Point Loading) (ASTM 2019), which provides a recognized standard for conducting these indirect tensile tests.

Based on a review of previous research, it has been observed that the steel fiber content in UHPC has a negligible effect on the first crack strength and first crack deflection as presented in the flexural load-deflection curve. However, it is noteworthy that the steel fiber content significantly affects the peak load of the material.

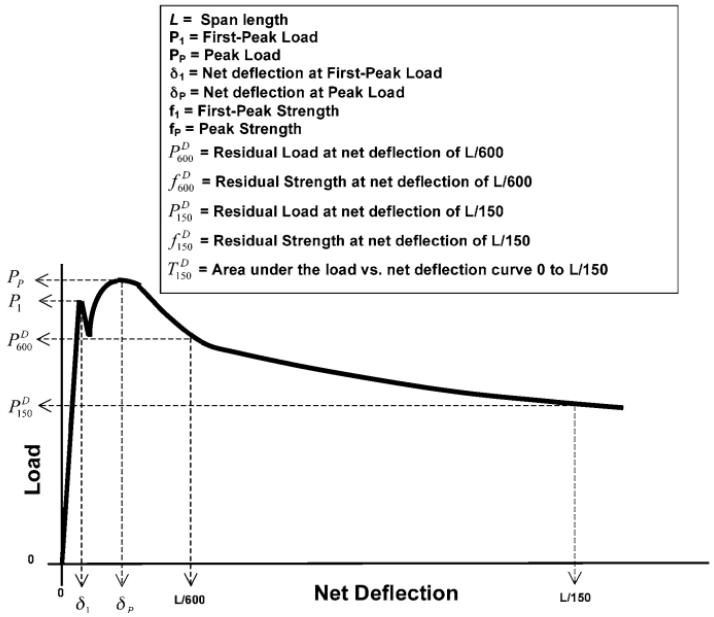

Figure 2-22 Load deflection curve for beam test ASTM C1609/C1609M-19a (ASTM, 2019)

Wu et al. (2016) reported a substantial increase in peak load for hooked fibers compared to straight fibers when conducting the flexure-tensile test. In their study, they utilized straight, corrugated, and hooked-end fibers, all of which had a tensile strength of about 2800 MPa (406 ksi), a diameter of 0.2 mm (0.008 in.), and a length of 13 mm (0.51 in.). During the flexural testing process, the incorporation of 2% fibers led to an increase in the peak load by 46.3%, 81.1%, and 61.4% for the straight, hooked end, and corrugated fibers, respectively, compared to concrete without any fiber additives.

Moreover, peak deflection also displayed a noticeable increase of 76.7%, 153.3%, and 123% for straight, hooked end, and corrugated fibers, respectively. These findings emphasize the advantages of using hooked fibers over straight fibers in UHPC, as validated by flexural testing.

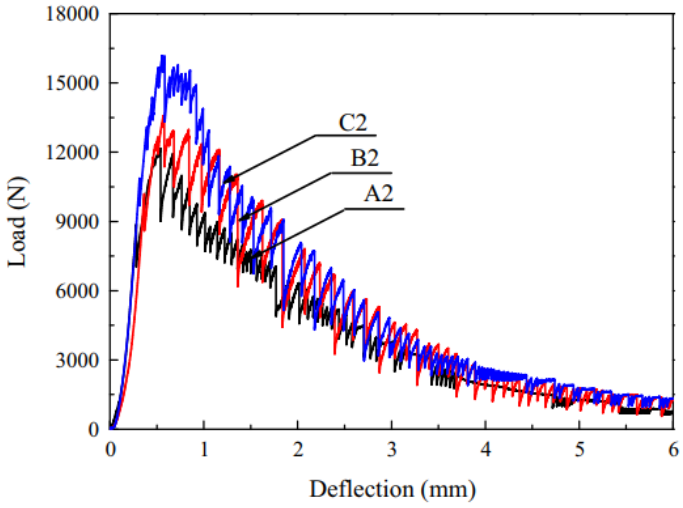

Figure 2-23 Effects of UHPC steel fiber shapes on load-deflection curve (A-straight, B-corrugated, and C-hooked) (Wu et al., 2016)

The flexural tensile test conducted by Yoo et al. (2017) yielded intriguing results that appear to contradict findings from earlier research. They reported reduced flexural strength for hooked fibers compared to straight fibers, which disagrees with the consensus of previous studies. A number of possible explanations for this unexpected result could include poor fiber distribution as the fibers came in a bundle, a decrease in pullout capacity resulting from fiber congestion (likely linked to bundling), and the adverse impact of microcracks on the performance of adjacent fibers. The specific types of fibers utilized in their flexural test, along with the observed flexural response of the UHPC, are detailed in the following sections.

Table 2-5 Steel fiber study results of Yoo et al. (2017)

Type of fiber	d_f (mm)	l_f (mm)	Aspect ratio (l_f/d_f)	Density (g/cm^3)	f_{ft} (MPa)	E_f (GPa)
S13	0.200	13.0	65.0	7.9	2788	200
S19.5	0.200	19.5	97.5	7.9	2500	200
S30	0.300	30.0	100.0	7.9	2580	200
H30	0.375	30.0	80.0	7.9	2630	200

[Note] Sxx = straight steel fibers with a length of xx, Hxx = hooked steel fiber with a length of xx, d_f = fiber diameter, l_f = fiber length, f_{ft} = tensile strength of fiber, and E_f = elastic modulus of fiber.

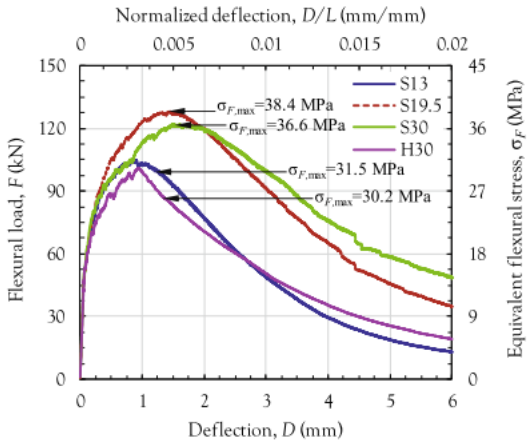

Figure 2-24 Effect of fiber type on UHPC flexural loads and deflection curves (Yoo et al., 2017)

In flexural beam tests, cracks often initiate at locations experiencing high tensile stress, particularly near the bottom surface of the beam. This high tensile stress arises primarily from the bending moment generated by the applied load. As the load continues to increase, the tensile stress surpasses the UHPC tensile strength, resulting in crack formations.

The initiation of cracks creates a loss in the fiber-bridging effect. This occurs as the fibers are pulled out from the UHPC matrix. Consequently, additional flexural cracks surface as a result of the redistribution and homogenization of stresses within the concrete. These new cracks form adjacent to the existing cracks (Qi et al., 2018).

2.8 Double Punch Test (DPT)

The DPT is a simple yet reliable methodology for determining the UHPC tensile strength and fracture toughness. Trumbauer & Chen (1971) initially developed the DPT to assess the tensile strength of plain concrete. The DPT is grounded in a well-established principle concerning the limit state (i.e., an inelastic state) bearing the capacity of the concrete. This limit state principle has been rigorously studied from both theoretical and experimental perspectives since the 1950s.

In the DPT, two parallel holes are created in a cylindrical concrete specimen using cylindrical steel punches, followed by the application of compressive stress perpendicular to the holes' axis. Under this load, the specimen fails in tension along a plane situated between the two holes. This specimen failure yields valuable data about the material's tensile properties.

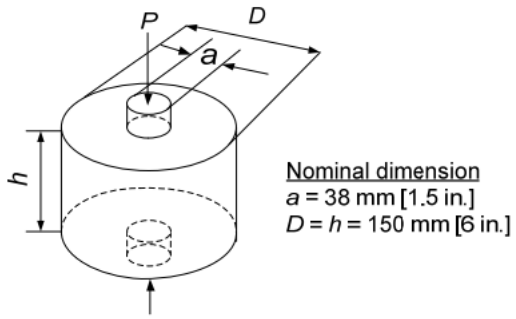

Figure 2-25 Setup for DPT test

The DPT has proven to be a highly effective tool, boasting numerous advantages. Beyond its capacity to determine tensile strength, the DPT method has been successfully used to predict other key fiber-reinforced concrete (FRC) parameters, such as strain-hardening, toughness, and stiffness. Notably, both compressive and tensile strength tests can be performed using the same testing equipment and associated instrumentation.

Because no predetermined fracture plane exists in split tensile tests, the DPT can cause multiple possible fracture planes . This feature aligns with the random dispersion and orientation of fibers within the specimen, thereby offering a more accurate representation of the fiber reinforcement effect, which is a crucial characteristic of FRC.

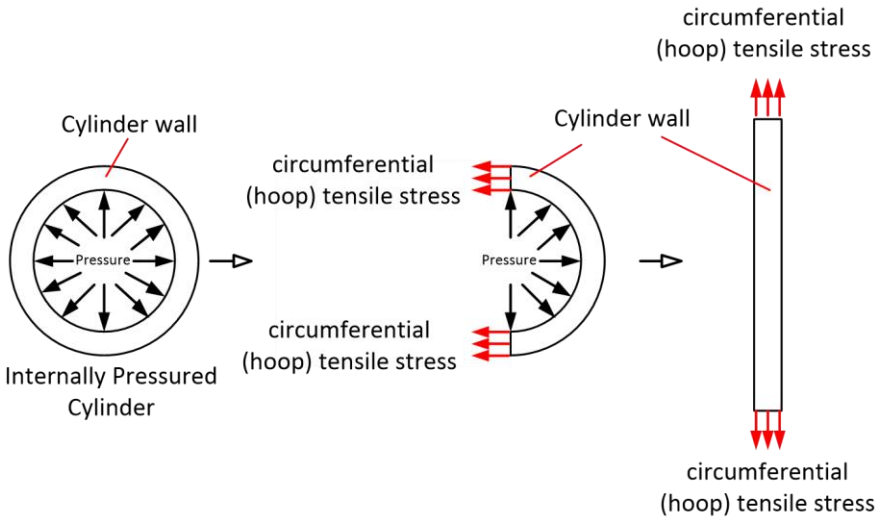

Figure 2-26 Mechanisms of working DPT test

One potential drawback of the DPT lies in the cost of the circumferential extensometer, which may limit its use in industrial and laboratory tests. However, Tuladhar & Chao (2019) conducted extensive research and discovered a linear correlation between circumferential strain and linear deformation. This finding allows the use of less

expensive linear variable differential transformers (LVDTs) in DPT tests, making this method more accessible.

Tuladhar & Chao (2019) found that the DPT can provide averaged mechanical behavior outcomes due to the simultaneous occurrence of multiple crack planes, thereby inducing less variability in the load-versus-deformation curves for specimens of the same batch. This result can serve as an evaluation tool for mixture quality. In contrast, the uniaxial DTT and the ASTM C1609 make the third point bending test possible. It is typically governed by a single primary crack, which exhibits considerable data variability due to the effects of fiber distribution.

Tuladhar & Chao (2019) also conducted a DPT using 3% micro steel fibers with specified properties (i.e., a length of 13 mm (0.5 in.), a diameter of 0.2 mm (0.079 in.), and a tensile strength of 2158 MPa (313 ksi). They compared these results with those from the DTT and ASTM C1609, while observing the coefficients of variation (COVs) at peak strength. The post-cracking strength demonstrated through the direct tensile test (DTT) curves and the ASTM C1609 test were significantly higher than that of the DPT. In addition, when Tuladhar & Chao (2019) compared samples with 0.75%, polyethylene (PE) to those with 3% steel fibers, they discovered that DPT could differentiate between tensile strain-hardening and strain-softening behavior as well as residual strength.

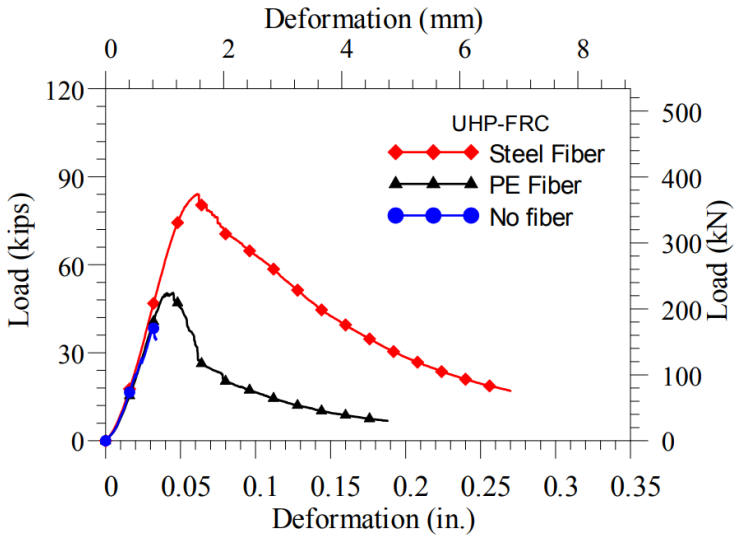

Figure 2-27 Load vs deformation curve with various UHPC mixtures (Tuladhar & Chao, 2019)

Given the relatively limited amount of research conducted utilizing the DPT method, this thesis aims to contribute further data to this field. The focus will be on comparing the performance of hooked fibers and straight microfibers at varying volume fractions using the following tests: the direct tensile test (DTT), the double punch test (DPT) and the ASTM C1609 test. Through this analysis, this thesis intends to shed more light on the behaviors and comparative advantages of these fiber types under different testing methodologies.

2.9 Ductility

Ductility is a structural property that allows significant deformation without sudden failure. In the context of UHPC, ductility is primarily determined by the bond between the cementitious matrix and the embedded fibers. Abbas & Khan (2016) pointed out that the failure mode responsible for the ductile behavior of UHPC can be attributed to the sequence of fiber bridging, fiber debonding, and fiber pullout.

Notably, fiber pullout is the desirable failure mechanism, as a rupture within the fibers would result in a brittle failure, which is less predictable and hence more dangerous. This concept underscores the importance of the interfacial bond between the matrix and the fibers in ensuring the ductile behavior of UHPC structures.

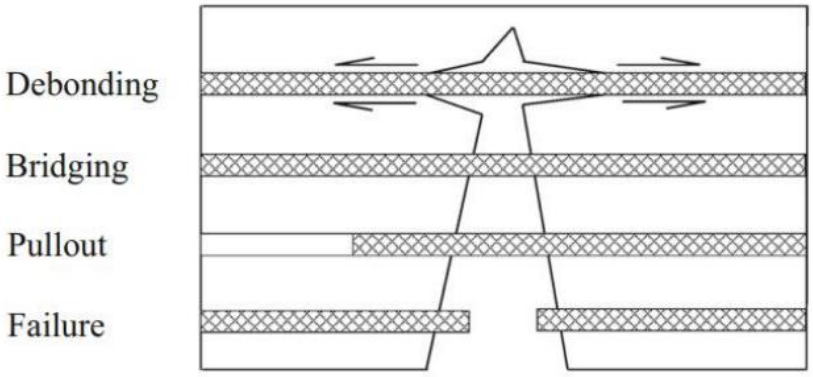

Figure 2-28 Mechanism of fiber-cementitious matrix interaction (Abbas & Khan, 2016)

The tensile behavior and ductility of the brittle ultra-high-performance concrete (UHPC) are controlled by the fiber bridging at the crack surfaces. This phenomenon is influenced by factors such as the type of fiber (characterized by the mechanical properties of the fibers) and the strength of the cementitious matrix (determined by its packing density) (Wille & Naaman, 2012).

High strength hooked fibers are commonly used in the UHPC mix. The end hook of these fibers can enhance the fiber bridging property based on the improvement of the mechanical property. Many researchers have investigated the impact of hooked fibers on the bonding strength and the pullout energy of UHPC.

Hooked fibers demonstrate mechanical bonding that, after initial adhesion and ductile internal friction, results in high pullout and fracture energy; this process is effective during the early to mid-stages of straining, enhancing the bridging effect and post-

cracking strength, and can induce significant strain-hardening if it exhibits slip-hardening (Naaman et al., 1991).

In material behavior, slip-hardening and slip-softening refer to two distinct responses to pullout forces in a fiber-matrix system. Slip-softening behavior manifests as an initial increase in pullout force up to a particular load, after which the force decreases. This behavior is exemplified by fibers bridging a first crack but failing to sustain loads beyond a certain threshold within the elastic region, leading to failure at that single crack. In contrast, slip-hardening behavior embodies a more resilient response to cracking. Upon the occurrence of the first crack, the fibers bridging it sustain higher loads, initially demonstrating a linear load-slip curve that transitions into non-linearity. This action induces an increase in force in regions of the matrix away from the initial crack, promoting the development of multiple cracks instead of a failure at a single point. This distinction between slip-hardening and slip-softening behavior underlines the contrast in bond behavior, with the former being optimal as it enhances composite ductility within the matrix.

Figure 2-29 shows the pullout load vs slip for the hooked fibers and the straight fibers, portion BC shows the slip hardening portion for the hooked fibers which is represented by the non-linear portion in the graph.

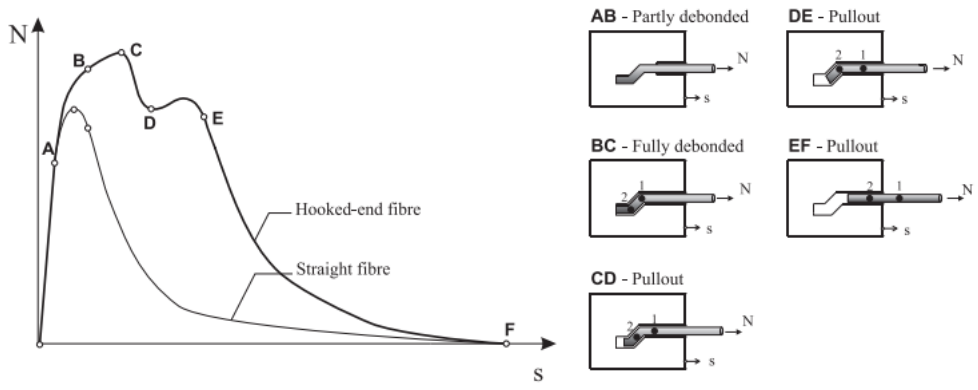

Figure 2-29 Pullout relationship between the load and the end-slip for hooked fiber (Cunha et al., 2010)

When comparing the pullout of high-strength hooked-end fibers with that of straight fibers, Wille & Naaman (2012) found that the former's pullout resistance was four to five times greater than that of straight microfibers tested under identical conditions.

According to Wille & Naaman (2012), hooked steel fibers embedded in UHPC exhibited superior pullout resistance, both in terms of bond strength and energy absorption capacity, when compared to straight microfibers. The bending resistance of an end hook during pullout exerts pressure on the cement matrix, thereby augmenting the frictional force and, by extension, the pullout resistance. This mechanical contribution, however, diminishes as slip increases and only proves beneficial until the end hook is straightened.

In this paper, we aim to examine the effect of hooked fibers on pullout strength for the custom-developed cementitious matrix based on the results of single fiber pullout tests.

2.10 Analytical Investigation of ASTM C1609 beam test

The ASTM standard employed in the flexure test of concrete beams provides an indirect evaluation of the tensile characteristics of fiber-reinforced concrete. However, potential discrepancies in underlying assumptions necessitate further investigations to ensure the method's validity in assessing tensile response.

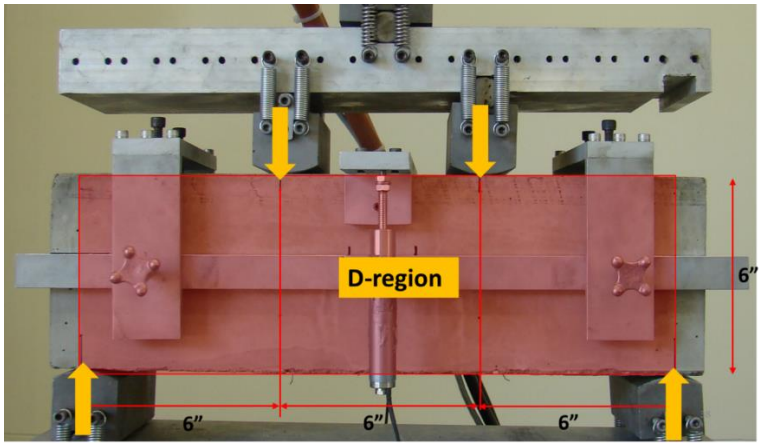

Figure 2-30 D-region for ASTM beam as per (ACI 318-19, 2019)

The strut and tie method chapter from ACI 318-19 (ACI, 2019) alludes to a discontinuity in stress distribution at a concentrated load. This discontinuity is presented to extend to a distance equivalent to the beam's depth (d) from the load application points (Figure 2-30). Such a condition implies a nonlinear strain distribution within the beam cross-section, challenging the foundational assumption of the ASTM C1609/C1609M-19a standard (ASTM, 2019) plane section's remaining plane. As a result, the stress (σ) calculation based on the equation $\sigma = \frac{Mc}{I}$, might not accurately reflect the true stress conditions.

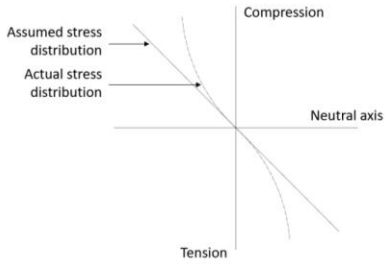

Figure 2-31 Stress distribution across specimen depth in flexural test (Liao et al., 2020)

The ASTM standard for the flexure test of concrete beams typically focuses on the region between the loading points, known as the D-region as shown in Fig. 2-30. This is where cracking is most likely to occur due to the constant moment exerted on the beam. However, this D-region, contrary to traditional understanding, exhibits a nonlinear strain distribution because of the concentrated loading. This observed behavior calls into question the assumptions inherent in conventional stress analysis. Therefore, it may be more precise to calculate the internal forces using the strut and tie model, given the evident nonlinear strain distribution within the D-region.

Furthermore, the widely accepted assumption of a constant moment and zero shear force between the loading points might also need to be reevaluated. In practical scenarios, the formation of a crack within the loading area may significantly affect the moment and shear force distribution in the D-region.

Thus, the traditional methodologies and their underlying assumptions need a thorough reassessment to obtain an accurate characterization of stress-strain behavior, especially in the D-region. To investigate these complex behaviors, this paper utilizes analytical modeling software such as Vector3 and Abaqus. These tools will help us investigate whether the region between loading points does indeed display a nonlinear strain

distribution. Moreover, we aim to determine whether the specific location of a crack within the loading region has any effect on tensile stress.

To study these complex behaviors, this research incorporates analytical modeling software (FEA), including Vector3 and Abaqus. This exploration seeks to verify the ASTM assumption that the beam might exhibit a nonlinear strain distribution. In addition, the possible impact of the precise location of a crack within the loading region on the tensile stress was studied. This investigation probes whether the manifestation of a crack at specific points within the loading zone could significantly affect the distribution of tensile stress, moment diagram, and shear force diagram. To depict these behaviors, moment and shear force diagrams were generated from the analytical models that incorporate cracks at different locations.

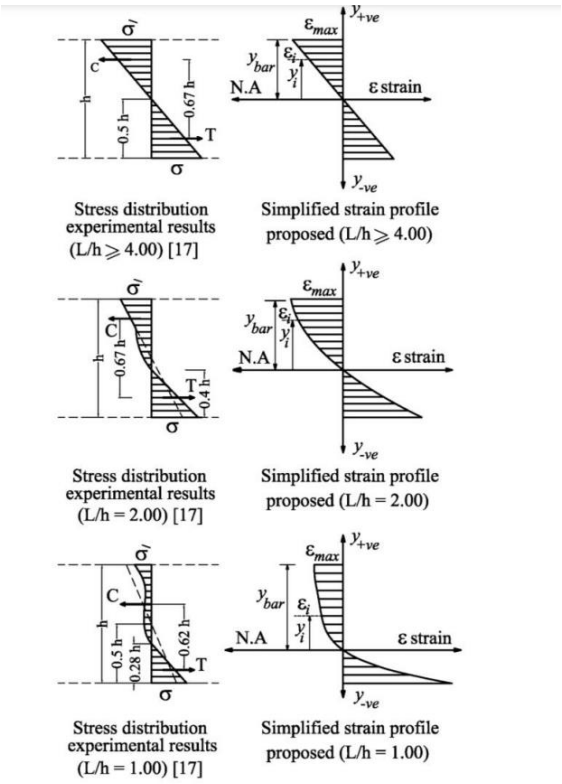

Figure 2-32 Experimental stress distribution results vs simplified strain profiles for deep beams under two-point or uniform loading (Abdel-Nasser et al., 2017)

According to ACI 318-19 (2019), a beam is classified as a deep beam if the length to depth ratio (L/d ratio) is less than 4. By this definition, ASTM C1609 beams fall under the category of deep beams. These beams exhibit nonlinear strain distribution, as depicted in Figure 2-32. Furthermore, in such deep beams, shear deformation becomes significant compared to pure flexure. As a result, the ASTM C1609 test might not purely qualify as a flexure test, given that the resultant cracks manifest as a combination of shear and flexural failures.

The tensile response, essentially the tensile stress-strain relationship, stands as a key characteristic of UHPC. This fundamental attribute can be obtained through a Direct Tensile Test. Nevertheless, this method presents several complications such as the lack of established ASTM standards, potential issues with eccentricity, and an intricate experimental arrangement, which makes it less preferred. As a practical alternative, the Flexural Test, an ASTM-standardized method, is broadly employed in industry. This testing approach yields results in the form of a force-deflection curve. While this does not directly provide the stress-strain relationship, it serves as a valuable input for back calculation. This process, in turn, allows for the derivation of the desired stress-strain relationship, thereby unlocking a comprehensive understanding of UHPC's tensile properties. Figure 2-33 shows the model selected to generate the stress-strain relationship. After the flexural test is completed, the load-deflection response is obtained which can be utilized to compute Young's modulus and the cracking strain (ε_{cr}) under the assumption of elastic relationships, leading to a calculation of σ_{cr}.

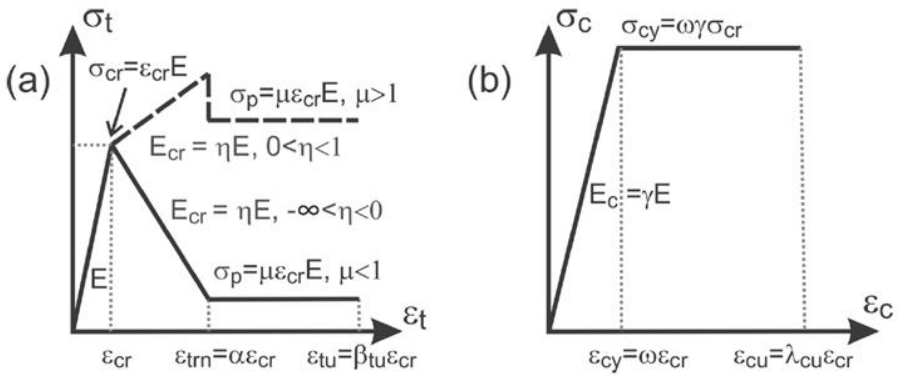

Figure 2-33 FRC model for (a) tensile strain-softening and (b) strain-hardening response (Soranakom & Mobasher, 2008)

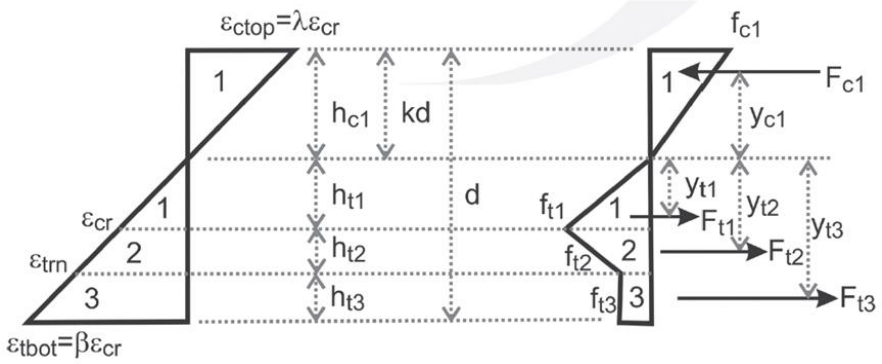

Figure 2-34 Strain and stress diagram at the post-crack stage (Soranakom & Mobasher, 2008)

Figure 2-34 presents strain and stress diagrams constructed across the cross-section of a beam where ε_{ctop} and f_{c1} correspond to the compression results, and ε_{cr} corresponds to the peak stress, f_{t1}. Parameters, α, β, and λ are based on material properties, which give the corresponding ε_{trn}, ε_{tbot} and ε_{ctop}, respectively. Assuming that the linear strain is valid, ε_{trn} can be pinpointed, which corresponds to f_{t2} based on one-one stress-strain relationship. The residual stresses, f_{t2} and f_{t3}, are calculated based on the moment capacity calculated from the stress diagram, which is compared with the experimental data and modification is made accordingly.

However, all these back calculations rest upon the presumption that the strain profile along the cross-section maintains linearity and that there exists a one-to-one relationship between stress and strain. Given that the ASTM C1609 beam is categorized as a deep beam, and the region of interest resides in the D-region, the assumption of strain linearity may be invalid. As such, an accurate depiction of the stress-strain curve could be potentially unattainable under these circumstances. This thesis seeks to delve into this matter further, probing the validity of these assumptions and their implications for stress-strain characterization.

3 EXPERIMENTAL PROGRAM

3.1 Development of Proprietary UHPC mix.

UHPC is formulated with the objective of optimizing particle packing density and leveraging self-compacting mechanisms. For this study, the materials sourced from US markets include Ordinary Portland Type I cement, fly ash, silica fumes, two variants of sand, two types of high-strength steel fibers (straight and hooked), high-range water reducers (HRWRs), and water.

Ordinary Portland Type I cement, a standard and readily available cement in the US, served as the primary binder in the mix. Fly ash, a byproduct of burning pulverized coal in power plants, was incorporated to improve the mix's flowability, minimize voids, reduce permeability, and enhance compressive strength, mitigating heat generation during curing when used in significant quantities.

Silica fume is a valuable ingredient for UHPC, primarily due to its capacity to augment the compressive strength of concrete. It enhances the mix's cohesion and increases its impermeability, making it a strategic component of UHPC. We selected the Norchem silica fume for our UHPC research primarily because of its higher carbon content which gives the mix a degree of stiffness that can positively affect the overall behavior of UHPC.

We used two distinct types of sand: coarse Sand 1 with particle sizes ranging from 400-800 microns and fine Sand 2 with particle sizes ranging from 80-200 microns. The inclusion of glass powder in UHPC is an environmentally friendly approach as it repurposes material otherwise destined for landfills. Glass powder also has the potential

to diminish the mix's carbon footprint by replacing cement and quartz powder without compromising compressive strength. The smooth surface and low water absorption of glass powder further enhance the workability of the UHPC mix.

Incorporating fibers in concrete can improve its mechanical properties, particularly in tensile strength and ductility. The integration of fibers in UHPC enhances its post-cracking performance, increases energy dissipation capacity, and fosters wider crack spacing with reduced crack widths.

This study uses two types of fibers: high-strength straight microfibers and high-strength hooked fibers.

Table 3-1 Fibers used in the study.

Fiber	Diameter* (d), mm	Length* (l), mm	Aspect Ratio (l/d)	Tensile Strength, MPa (ksi)
Straight smooth fiber (Bekaert OL 13/.20)	0.175	12.5	71.4	2,160 (313)
Hooked fiber (Bekaert 3D 80/30)	0.38	30	80	3,070 (455)

Figure 3-1 Types of fibers used in the study. (a) Hooked fibers and (b) straight microfibers

High-range water reducers (HRWRs) are pivotal in influencing the fresh characteristics of UHPC. Correctly dosed, HRWRs can enhance the mix's flowability and facilitate uniform fiber dispersion. However, overuse can result in excessive flowability, causing fiber segregation and an uneven mix, while underuse can lead to a stiff mix. For subsequent tests, including single fiber pullout, tensile, beam, and double punch tests, a proprietary mix developed at the University of Texas at Arlington was utilized, which is detailed in other sections of this thesis.

3.1.1 UT Arlington Mix Design

The original proprietary mix used in this study was developed by Aghdasi et al. (2016) at The University of Texas at Arlington. However, due to the dynamic nature of the US market, some previously utilized components were no longer available, necessitating minor adjustments to the mix design for the current research. Table 3-2 lists details of the components used in this study.

Table 3-2 Components used in the UTA mix design.

Components	Particle size	Suppliers
Cement Type I	0.00079 in. (20 μm)	Any US supplier
Fly ash	0.00079 in. (20 μm)	Class F
Silica Fume	0.00047 in. (1.2 μm)	Norchem
Silica sand 1	0.02 in. (500 μm)	US Silica
Silica sand 2	0.0047 in. (120 μm)	US Silica
Glass Powder	0.00067 in. (1.7 μm)	US Silica
HRWR	Poly-carboxylate based	BASF Co. (Melflux)

Table 3-3 Mix Design for UTA-UHPC

Cement	Fly ash	Sand 1	Sand 2	Silica Fume	Glass Powder	HRWR
1	0.2	0.43	0.37	0.25	0.25	0.021

The concrete mix components were proportioned as shown in Table 3-3, focusing on achieving a high packing density, aiming to enhance the mechanical properties of the resulting UHPC mix. Concurrently, considerations were made to maintain adequate mix flowability, which is crucial for ensuring uniform mix and preventing fiber segregation. This type of flowability ensures a more balanced and effective UHPC mix.

3.1.2 Mixing procedure

Figure 3-2 Lab mixer used for casting five quarts of UHPC.

Figure 3-3 This lab mixer was used to prepare 40 quarts of UHPC.

Figures 3-2 and 3-3 illustrate the lab mixers employed in the UHPC casting process. More precisely, the mixer represented in Figure 3-2 has a volume of five quarts and was used for mixing a smaller number of cubes. The larger mixer presented in Figure 3-3 was suitable for casting a larger quantity of cubes or a single dog bone specimen within each batch due to its greater capacity of 40 quarts.

The UHPC mixing procedure begins with a premixing phase where all dry materials, excluding the superplasticizer, are mixed for five minutes at Speed 1 (60 rpm). This step ensures a homogeneous distribution of the materials. Following this, high-range water reducers (HRWRs) are incorporated into the mix, and the mixing is extended for an additional two minutes. The subsequent stage involves a slow and steady addition of water for over a minute of continuous mixing.

Approximately six to seven minutes into the process, the mix becomes liquefied, and the fibers are then integrated. Mixing persists until the fibers are uniformly spread within the mix. The final phase of the mixing process involves an increase according to the mixer's Speed 2 (124 rpm) for roughly two minutes. This increase in mixing speed facilitates the attainment of the desired consistency in the UHP-FRC mix.

3.1.3 Effect of curing method on the compressive strength of the UHPC mix.

UHPC is renowned for its superior mechanical properties, including remarkable compressive strength, tensile strength, ductility, and flowability. However, attaining these standout characteristics necessitates rigorous quality control protocols, which are easier to implement in precast plants than on-site, cast-in-place UHPC segments.

Given this context, the primary goal of this study is to conduct a comparative analysis of various curing methodologies applied to UTA's proprietary UHPC mix to identify the most effective strategy for accelerating early strength development. This aspect is essential since faster strength gain can significantly expedite construction timelines, increasing efficiency and creating a more cost-effective building process.

Park et al. (2015) conducted a comprehensive study examining the early-strength gain of UHPC under diverse curing conditions. The variables considered in this investigation included curing temperature, delay time prior to the commencement of curing, duration of curing, and moisture condition. This thesis, conducted at UTA, employs parameters including curing temperature, delay time, and moisture condition as foundational variables for curing conditions to enhance the compressive strength of UHPC.

The research places specific emphasis on the exploration of temperature-controlled curing methods. It probes into the impact of two different curing temperatures, 90°C and

65°C, on the mechanical properties of UHPC. In addition, the study also scrutinizes the influence of delay time (duration till which specimens were kept in the curing room before providing heat treatment) prior to the initiation of heat curing treatment on the overall performance of UHPC.

By delving into these critical factors, this research hopes to furnish valuable insights that can guide the development of optimized curing protocols for UHPC, ultimately contributing to more efficient and effective construction practices. Figure 3-4 shows the oven used for the heat treatment of UHPC specimens. Water was added around the specimens during the heat treatment process, thereby maintaining the humidity to prevent the loss of moisture in the cube mix.

Figure 3-4 Oven used for heat treatment.

3.1.4 Study on Flowability of UHPC based on changes to specific materials.

Flowability is a crucial property of UHPC. UHPC represents a fusion of three distinct concrete technologies: Self-compacting concrete (SCC), fiber-reinforced concrete (FRC), and high-performance concrete (HPC), and flowability plays a vital role in ensuring that the concrete self-compacts while simultaneously preventing fiber segregation.

Flowability is a fundamental characteristic of UHPC, given its integration of three unique concrete technologies: self-compacting concrete (SCC), fiber-reinforced concrete (FRC), and high-performance concrete (HPC). In this context, flowability is essential to ensure the self-compaction of the concrete while simultaneously preventing fiber segregation and contributing to the overall UHPC performance and integrity.

The workability or flowability of freshly mixed UHPC was evaluated using a flow test conforming to the ASTM C1437-20 (2020). The final UHPC mixture was transferred to a truncated cone, as shown in Fig. 3-5. The cone was filled, and then the attached handle was used to impart 25 impacts to the base plate through rotation. Following this, the spread cone was gently lifted without disturbing the mix, enabling the concrete to freely spread across the plate.

Figure 3-5 Flowability test

This research aimed to enhance UHPC flowability to improve its application in manufacturing UHPC-based slurry infiltrated fiber concrete (SIFCON). To achieve this goal, several constituent materials were systematically investigated and adjusted. For instance, the study examined the effects of employing silica fumes with distinct purity levels on the mechanical properties of UHPC. Additionally, a comparative analysis was

conducted between two types of fine sand, with the second variant exhibiting a more spherical shape. Furthermore, the effects of substituting fly ash with slag cement on the flowability of UHPC were evaluated by comparing mixtures containing these supplementary cementitious materials.

3.1.5 Effect of Silica Fume Purity on UHPC mechanical strength

While prior studies on UHPC have predominantly investigated the impact of varying silica fume replacement levels on mechanical properties like compressive strength and flowability, this thesis adopts a more distinct approach. It maintains a constant level of silica fume replacement and focuses on manipulating the type of silica fume utilized based on its purity level. The aim is to explore how these changes affect the resulting mechanical properties of the UHPC mix.

The purity of silica fume is primarily determined by its silicon dioxide (SiO_2) content. The high SiO_2 content in silica fume imparts its pozzolanic properties, which facilitates a reaction with calcium hydroxide—a byproduct of cement hydration—to generate additional cementitious compounds. The formation of these compounds helps to fill the concrete pores, enhancing its strength and durability.

In this preliminary investigation, three types of silica fume—920U, W940U, 970U—were employed, and each type was different based on its purity level or silicon dioxide percentage (92%, 94%, and 97%, respectively). The new silica fumes are more spherical than the Norchem silica fume used in the study, enhancing the UHPC mix's flowability property. Given the reduction in fly ash production in North America due to the transition from coal-fired to gas-fired power plants, this study replaced fly ash with an equivalent amount of slag cement to see the changes in the mechanical properties of UHPC.

3.2 Tensile Response

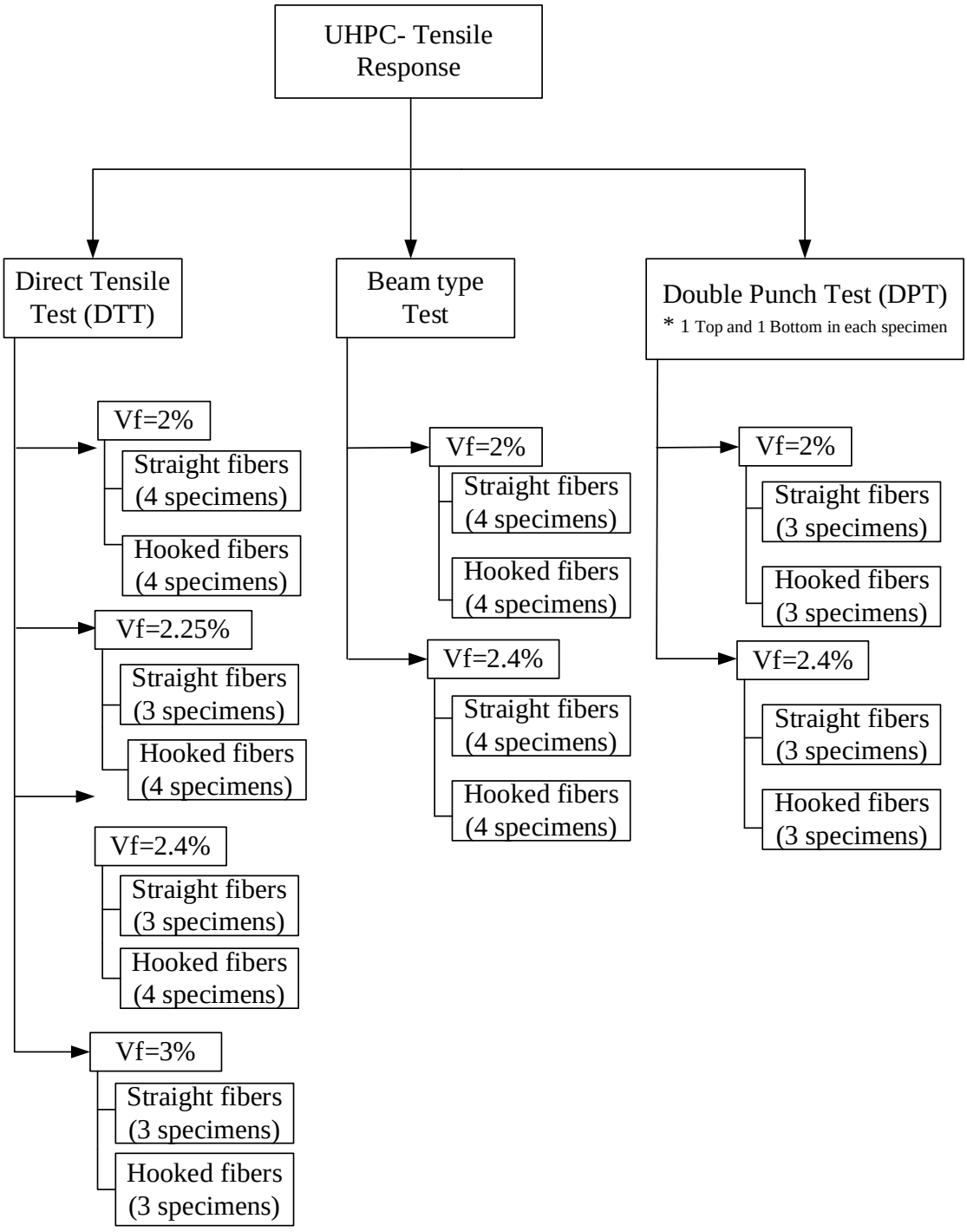

Figure 3-6 Tests completed in the thesis.

This research primarily compares the tensile responses of high-strength 3D fibers and microfibers utilized in varying volume fractions. For the purpose of contrasting different testing methods, the selected volume fractions were 2% and 2.4%. The upper limit for the volume fraction was capped at 2.4% as fiber entanglement began to manifest beyond this point, potentially compromising the UHPC mix's integrity.

However, when examining the tensile responses of hooked fibers and straight microfibers using the direct tensile test (DTT), a broader range of volume fractions were deployed (i.e., 2%, 2.25%, 2.4%, and 3%). For the 3% fiber volume fraction, a slurry-infiltrated fiber concrete (SIFCON) approach was undertaken to circumvent fiber entanglement issues specifically for the hooked fibers.

3.3 Direct Tensile Test (DTT)

The focus of our interest lies primarily in UHPC tensile properties, given that the integration of fibers in UHPC facilitates the redistribution of internal tensile stresses across the specimen after initial cracking. This process leads to tension strain hardening after forming the first crack, culminating in a more ductile failure under tension. Owing to the absence of an ASTM standard for DTTs, we used the specimen shape and testing method developed at The University of Texas at Arlington (Chao et al., 2011).

Within the scope of this study, direct tensile tests were performed employing an MTS Model 810 testing machine situated in the UTA Civil Engineering Lab Building (CELB). We crafted and evaluated large-scale dog bone-shaped specimens with a cross-sectional area measuring 16 square inches. Fig. 3-7 shows the dimensions, and Fig. 3-7 shows the test setup of these large-scale dog bone specimens.

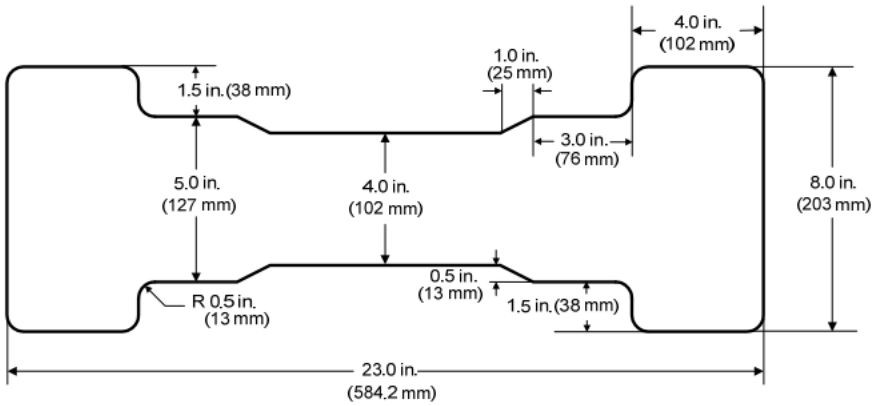

Figure 3-7 DTT specimen shape and size

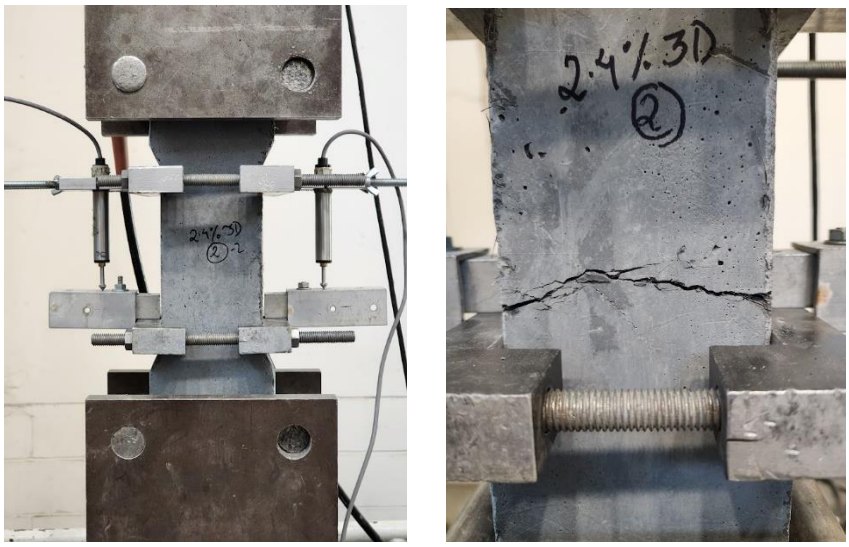

Figure 3-8 DTT test setup

When preparing larger concrete batches, we used the Zyklos ZK 150 HE rotating pan mixer (Pemat Mischtechnik GmbH, Freisbach, Germany). This mixer offers a ready-made mix batch capacity of 75 liters (2.65 cubic feet) and can accommodate a maximum dry charge of 108 liters (3.81 cubic feet), which translates to approximately 120 kg (265 lbs).

The mixing process entailed carefully weighing the dry components of the concrete mixture using buckets, as shown in Figure 3-9. These measured ingredients were

transferred to a pan mixer, as shown in Figure 3-10. Water was introduced into the mix incrementally to obtain the correct paste consistency. Once this base mixture was prepared, fibers were added. The mixture was then subjected to several minutes of mixing until a homogenous blend was obtained, ensuring the optimal distribution of fibers throughout the mix.

Figure 3-9 Material preparation and mixing

Figure 3-10 Pan mixer used for mixing UHPC specimens

For the DTT, specimen failure must occur within its central section, designated as the gauge length, with a cross-sectional area of 16 square inches. This requirement ensures

that the observed failure is attributed solely to tension, enabling precise analysis of the results. To direct the failure towards this desired region, the broader ends of the dog bone-shaped specimen are fortified with five layers of horizontal steel mesh. Additionally, two layers of vertical mesh are applied at the points where the specimen's cross-section changes, as demonstrated in the accompanying figure. These reinforcements help concentrate the tensile stress within the specimen's gauge length, ensuring the test outcomes' validity.

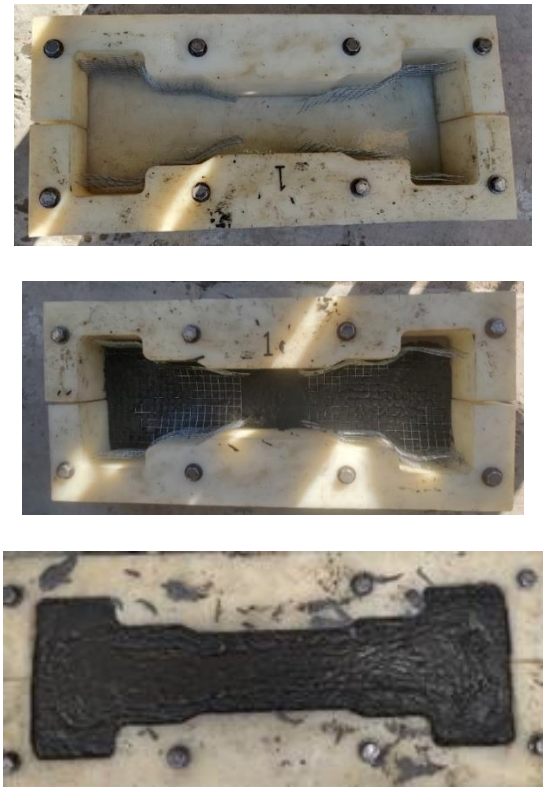

Figure 3-11 Process of applying steel mesh for DTT specimens.

3.4 Single Fiber Pullout Test

A key determinant in the UHPC tensile behavior is the bond-slip relationship between the fiber and the cementitious matrix, which is typically characterized by physicochemical and mechanical bond properties. This study focuses on the mechanical bond aspect, which can be enhanced through hooked fibers.

During the pullout process, the ends of a hooked steel fiber must experience substantial deformation and yield before being extracted from the concrete, thereby contributing to improved ductility. This usually results in straightening the fiber ends, which were initially deformed before the pullout occurred. The ductility of fiber-reinforced concrete (FRC) is influenced by the fiber's capacity to pull out and bridge cracks. In light of this, a pullout test was conducted in this research to investigate the pullout resistance of hooked fibers.

Test specimens were prepared using Plexiglas molds with a cross-section of 0.98 × 0.90 inches and a length of 2.76 inches. Fibers were embedded at the desired length (ld/4), where L_d is the length of the fibers needed to ensure a fully embedded hook. The fibers were secured by embedding them in Styrofoam blocks measuring 1 x 2 inches. Figure 3-12 below visually depicts the specimen preparation process.

The concrete mix was then poured into the molds and gently vibrated to ensure even distribution and elimination of air pockets. The specimens were smoothed out, covered with plastic sheets for 24 hours to allow for initial curing, then de-molded, labeled, and stored for subsequent testing.

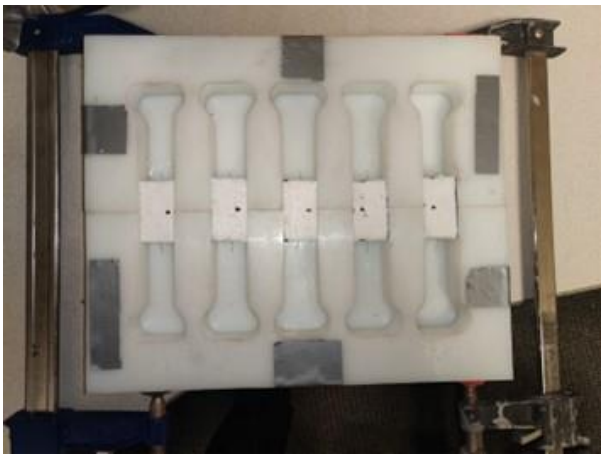

Figure 3-12 Mold for fiber pullout test

A specially designed clamp, attached to the testing machine's load cell, was used to grip the top of the specimen. The body of the specimen was held by a grip typically used for ASTM tensile mortar tests. To simulate a fiber being pulled in a standard cracked tensile specimen and reduce the effects of the fiber's free elongation, the free length of the specimen should be minimized. Following this, force and displacement were measured to create a pullout load versus the slip graph.

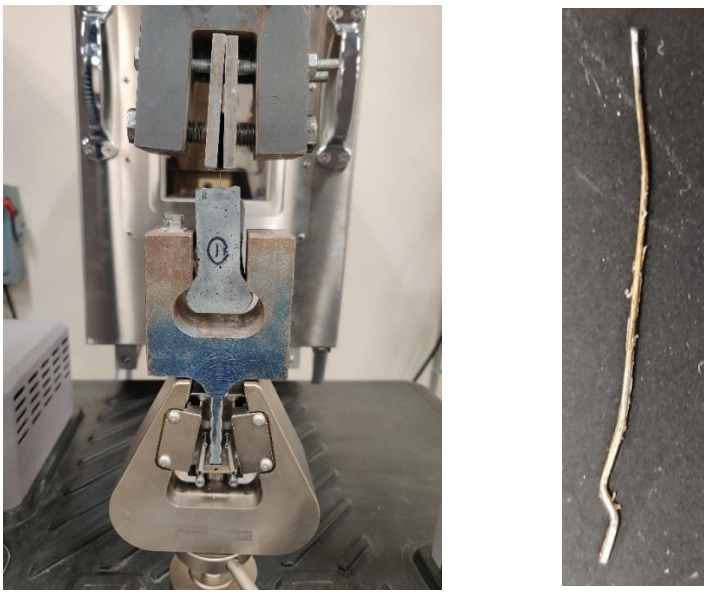

Figure 3-13 Fiber pullout test setup and fiber after completion of pullout test

3.5 Beam-type ASTM C1609 test

To assess UHPC flexural performance, the ASTM C1609 standard was utilized. A 6" × 6" × 21" beam was tested over an 18-inch span. As depicted in the accompanying figure, the test setup features a third-point loading arrangement comprising two hinged supports and two loading points positioned on top.

A rectangular jig, positioned on the beam's neutral axis directly over the supports and enveloping the beam, ensured accurate mid-span deflection readings. Linear variable differential transformers (LVDTs) are strategically located on both sides of the beam to capture the deflection at mid-span. This test setup is designed to minimize errors arising from twisting or incorrect seating of the concrete specimen within the supports, thereby ensuring reliable and valid results.

In the experiment, the tensile performance of straight microfibers and 3D hooked fibers were compared at 2% and 2.4% volume fractions, respectively.

Figure 3-14 Mold and UHPC beam specimens for ASTM C1609 test

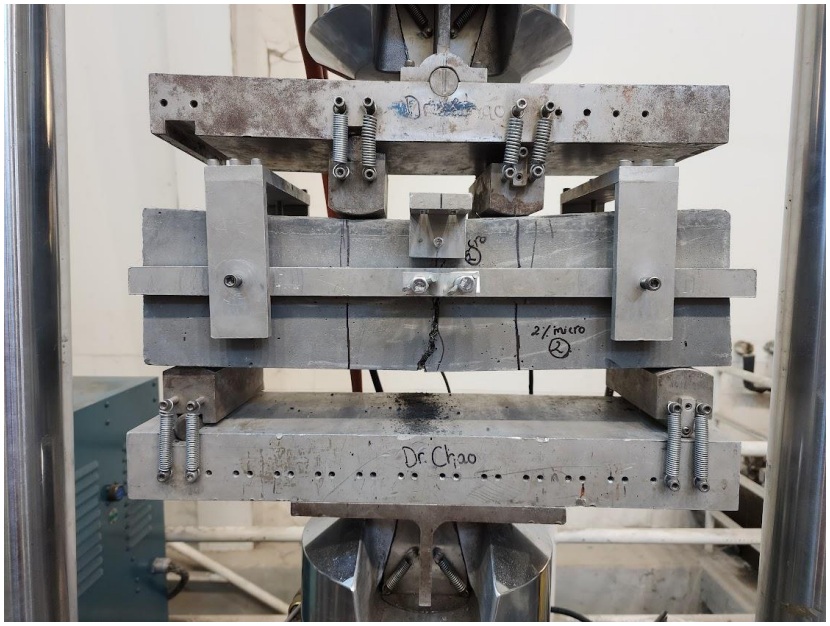

Figure 3-15 Test setup for beam-type test

3.6 Double Punch Test

The objective of the study is to assess if the Double Punch Test can serve as an alternative method for conducting tensile tests of UHPC specimens. 6-inch by 12-inch cylindrical UHPC specimens were cast in a pan mixer as shown in Figure 3-10.

Figure 3-16 Mold for double punch test (DPT)

The 6-inch by 12-inch cylinder sample was divided into two 6" × 6-inch cylinders, referred to as the top and bottom. The upper and lower surfaces were smoothed using

sandstone or grinding techniques to ensure that the steel punches established an even (flat) contact with the top and bottom faces of the specimen.

Figure 3-17 Procedure for cutting DPT cylinder specimens.

Figure 3-18 Test setup for DPT test

The double punch testing setup includes a compression testing machine, a load shell, two steel punches, two LVDTs, and a DAQ (data acquisition system). During testing, the bottom steel punch is placed on top of a plate resting on the load shell. A 6" × 6" specimen is positioned on the bottom steel punch, followed by the placement of the top steel punch. To prevent eccentric loading, the top and bottom punches must be perfectly centered on the specimen. The compression machine applies each load at a constant rate of 0.04 inches per minute. A minor adjustment to the testing procedure, known as a shakedown, was led by Chao et al. (2011) to obtain a more precise stiffness measurement for specimens at the early stages of the test. In this method, the load was initially applied at a rate of up to 2 kips, then reduced to 0.5 kips, and finally reloaded to failure. The load shell measures the applied load, while the two LVDTs monitor vertical axial deformation, with the data recorded by the DAQ system.

Following this, the double punch testing (DPT) was conducted on conventional FRC with a fiber volume of 0.45%. The objective was to compare the outcomes from two distinct specimen preparation methods: The first involved a 6" × 6" mold that was halved, and the second involved specimens that were subsequently cut in half from specimens of 6" × 12". The study aimed to address complications encountered after cleanly halving the cylinder and ensuring that the top and bottom surfaces were uniformly smooth.

A gravity mixer was utilized to prepare the standard fiber reinforced concrete, as illustrated in Fig. 3-19.

Figure 3-19 Gravity mixer for casting normal fiber-reinforced concrete.

4 TEST RESULTS

4.1 Compressive strength of the UHPC mix.

As stated in Tables 3-2 and 3-3, the mix developed at the University of Texas at Arlington, incorporated a diverse range of materials including cement, fly ash, two types of sand, glass powder, silica fume, and superplasticizer, mixed in specific proportions. The thesis primarily concentrates on the comparative study of two distinct fiber types: straight microfibers and Bekaert 3D fibers (hooked fibers). To evaluate their effectiveness, compressive strength tests at 28 days were performed on 3×6-inch cylindrical samples.

Table 4-1 Compression test results

Fibers Type / Fiber Volume	Compressive strength (Straight Microfibers)	Compressive strength (Hooked fibers)
2%	16.386 ksi	16.69 ksi
2.25%	16.461 ksi	16.724 ksi
2.4%	17.75 ksi	18.653 ksi

The outcomes of the compressive strength tests indicate slightly better performance of the hooked fibers in comparison to the straight fibers, when evaluated at the same fiber volume.

Figure 4-1 Compression test on 3×6 in. cylinders

4.2 Heat Treatment curing protocol

The U.S. materials market often faces fluctuations, affecting the availability of certain components utilized in concrete mix designs. Notably, we recently experienced a shortfall of a specific type of fine sand. As a result, we engaged in extensive experimentation to establish an optimal mix design that could accommodate this unexpected change.

The solution we discovered involved two key alterations. First, we phased out the use of the fine sand used in the previous mix design, consequently adjusting the water-to-cement (w/cm) ratio to 0.18 to maintain comparable flowability. Second, we incorporated an alternative type of sand, which possessed a more spherical shape. This introduction proved beneficial, as it enabled us to achieve equivalent flowability to the previous mix but with a slightly reduced w/cm ratio of 0.19.

(a) (b) (c)

Figure 4-2 Flowability for (a)regular mix, (b) new mix with sand 2 (w/c-0.19) and (c)mix without sand2 (w/c-0.18).

Table 4-2 Compressive strength comparison

Mix	Compressive strength
Old mix (w/cm-0.2)	17.8 ksi
Mix with new sand(w/cm-0.19)	18.6 ksi
Mix without sand 2 (w/cm-0.18)	16.42 ksi

The mix incorporating the new fine sand demonstrated superior flowability and compressive strength compared to the mix without sand 2. However, the achieved strength did not meet the benchmark of 22 ksi as set by ACI Committee 239 for UHPC. To enhance the mechanical properties of the UHPC, heat treatment was applied to the new mix (w/c-0.19). Three distinct treatment scenarios were established: first, an oven temperature of 90 degrees with a 24-hour delay (where specimens were placed in the oven after 24 hours); second, a temperature of 60 degrees with a 24-hour delay; and third, a 65-degree oven temperature without any delay.

Table 4-6 shows the compressive strength for the mix with new fine sand and w/cm ratio of 0.19.

Table 4-3 Compressive strength for different curing protocol

Curing Protocol	1 day	28 days
90°C (24 hr. delay)	17.75 ksi	22.6 ksi
60°C (24 hr. delay)	13.79 ksi	17 ksi
65°C (Directly in the oven)	13.86 ksi	16.25 ksi

Given that the oven temperature of 90 degrees with a 24-hour delay exhibited superior outcomes relative to other curing conditions, this specific curing protocol was selected for further investigation.

Table 4-4 Extensive study of curing protocol (90 °C oven temperature and 24 hr. delay)

Curing Protocol	**Compressive strength (ksi)**
2 days in curing room -2nd day test	9.875
1 day in oven (24 hr. delay)- 2nd day test	17.75
2 days in oven (24 hr. delay)- 3rd day test	20.75
1 day in oven (24 hr. delay)- 7th day test	20.6
1 day in oven (24 hr. delay)- 28th day test	22.6
1 day in oven (24 hr. delay)- 28th day test	21.1
Only in curing room- 28th day test	18.6

Conclusion from the heat treatment test:

1. Specimens cured for 2 days in the oven demonstrated the highest early strength gain. However, the strength gained after 28 days for these specimens was minimum. Thus, to attain early strength, specimens should be cured in the oven for 2 days after 24-hour delay. This results in strength values akin to those seen after a 28-day period.

2. Curing for 1 day in the oven with 24-hour delay gave an overall better result on 28 days strength.

3. For better compressive strength of the UHPC specimens, heat treatment is essential as 28 days strength for specimens cured only in the curing room was much less compared to the specimen kept in oven for 1 day after 24 hr. delay.

4.3 Effect of Silica Fume Purity on properties of UHPC

Silica Fume, commonly used pozzolanic material, has been shown to enhance both the mechanical attributes and the durability of the UHPC mixtures. While numerous studies have explored varying replacement levels of silica fume, the focal point of this investigation was to maintain a fixed ratio of silica fume to cement at 0.25:1 and assess the influence of silica fume purity on UHPC properties.

Silica fume purity is quantified through its silicon dioxide (SiO_2) content. In the course of this study, three grades of silica fume - 920U, W940U, and 970U - were utilized, distinguished by their relative purity levels or silicon dioxide percentages (92%, 94%, and 97% respectively). These silica fumes were spherical in shape helping in flowability.

The study maintained the same mix formulation as the UTA-UHPC mix, with the only variation being the substitution of fly ash with an equivalent quantity of slag cement, as mentioned earlier. This was accompanied by a 3% microfiber content.

i. Flowability:

In this experiment, our aim was to minimize the water-to-cementitious material (w/cm) ratio, targeting a value less than 0.2, while maintaining sufficient flowability to ensure a workable mix. An important aspect was to prevent fiber segregation, which could compromise the homogeneity and mechanical properties of the mixture.

Table 4-5 Flowability test with different silica fumes

Silica Fume	w/cm ratio	Flowability
920U	0.185	7.25”
W940U	0.17	8.5”
970U	0.185	6.75”

Figure 4-3 Flowability test for a. 920U, b. W940U, c. 970U

From the observation made based on Table 4-2, the UHPC mix incorporating Silica Fume with a purity level of 94% exhibited greater flowability at a lower w/cm ratio, in comparison to the mixes using Silica Fume of 92% and 97% purity.

ii. Strength:

For the purpose of evaluating compressive strength, 2-inch cubic samples were casted and 28 days compression test was performed.

Figure 4-4 Casting of 2 in. cubes.

Table 4-6 Compression test with different silica fumes

Silica Fume	Compressive Strength
920U	20.47 ksi
W940U	19.66 ksi
970U	18.91 ksi

Referring to Table 4-3, preliminary assessments indicate that the 920U variant of Silica Fume (92% silica fume purity) outperforms the 940U (94% silica fume purity), which in turn is slightly better than the 970U (97% silica fume purity). It's important to note, however, that these findings are preliminary and further testing is required to substantiate these observations.

iii. Improving flowability with replacement of slag cement with fly ash

Fly ash is a cementitious material with more spherical particle shape, which when allowed in the mix allows the angular particles, like cement and sands to roll over each other during the mixing process enhancing the flowability of the mix.

In the experimental stage, silica fume 970U showed slight less flowability for w/cm ratio 0.185 and slag cement to cement ratio as 0.2 and hence, slag cement was replaced with fly ash to check the benefits brought about by addition of fly ash.

Table 4-7 Comparison of specimens with and without fly ash

Silica Fume	w/cm ratio	Flowability	Compressive strength
970U (w/o fly ash)	0.185	6.75”	18.91 ksi
970U (w fly ash)	0.185	7.375”	19.42 ksi

Figure 4-5 Flowability test a. 970U (w/o fly ash) b. 970U (w fly ash)

From Table 4-4, conclusion can be derived that application of fly ash has significant benefits in terms of flowability and the compressive strength, but further investigation needs to be done.

4.4 Single Fiber Pullout test

The body of the specimen was restrained by a grip, whereas the free edge with the fiber was such that it will replicate the pullout of the fibers with minimum effects of free elongation of the fiber. The fiber pullout was performed on the specimens as shown below. The values of the pullout load and the corresponding slip were recorded using Data Acquisition System (DAQ system).

Figure 4-6 Single fiber pullout setup

Figure 4-7 Sample test specimen for fiber pullout

The graph of pullout load versus slip is shown below. All specimens tested showed no fiber fracture and the fiber was pulled out from the matrix which is the good outcome we were expecting. All fibers exhibited the desired slip hardening behavior.

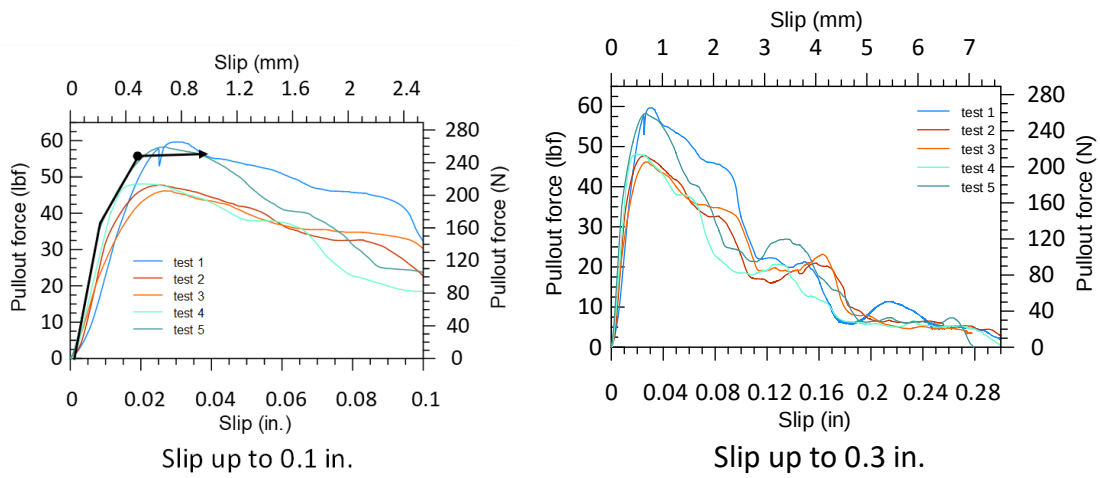

Figure 4-8 Pullout force vs slip curve

Maximum Fiber Tensile Stress, $\sigma = \frac{4*P_{max}}{\pi d^2}$

Average bond strength, $\tau = \frac{P_{max}}{\pi*d*L_E}$

Where, P_{max} gives maximum Pullout Load, d represents diameter of the fiber and L_E gives the embedment length.

Table 4-8 Single Fiber Pullout Test

	Test1	Test2	Test3	Test4	Test5
Max. Fiber Pullout Load (lbf)	59	47	46	49	58

Discussions:

1. The ascending part in the graph shows the bonding between the fibers and the UHPC matrix.
2. The force doesn't drop suddenly indicating no fiber rupture and demonstrating ductile behavior. The end hook of all the fibers after the test were straightened which shows full utilization of the mechanical bond.

3. The maximum pullout load is observed to be 59 lbf (265.3 N), maximum fiber tensile stress to be 339.3 ksi (2339 MPa) and the average bond strength of 4.3 ksi (29 MPa).
4. The non-linear curve depicted in Figure 4-8 demonstrates the slip-hardening behavior of the fiber, indicative of optimal bond characteristics that helps in enhancing the composite ductility of the UHPC.

4.5 Direct Tensile Test

The main objective of the thesis is to compare the tensile performance of the hooked fibers and commonly used straight microfibers using Direct Tensile Test (DTT) as a test measurement. Dog bone specimens were used for performing the Direct Tensile Test and the setup is shown below. Dog bone specimens were casted such that the failure will occur within the gage length of 6 inches and the cross-sectional area of 16 in^2. Failure pattern of one of the sample specimens is shown in the figure below.

Table 4-9 Number of Specimens (DTT)

Fiber Volume / Fiber Type	1.5%	2%	2.25%	2.4%	3%
Hooked	3	4	4	4	3(2021) 3(2023)
Straight	3	4	3	3	3

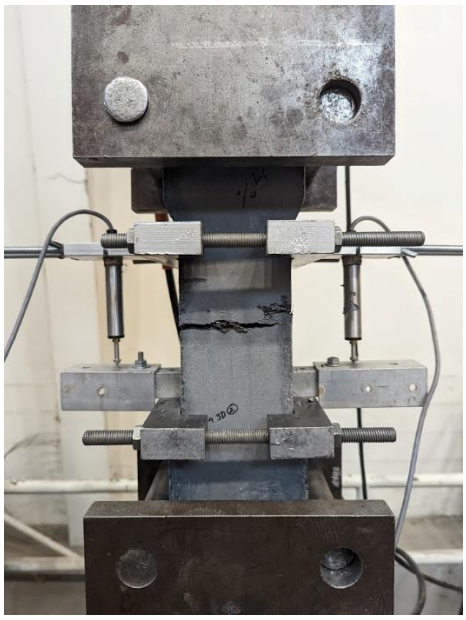

Figure 4-9 DTT specimens

The test was performed on dog bone specimens for fiber volume of 1.5%, 2%, 2.25%, 2.4% and 3%, with each fiber volume has at least 3 specimens for 3D fibers and microfibers, respectively. 3% hooked fiber specimens were prepared using slurry infiltrated fiber concrete (SIFCON) method because of the problem with pan mixing due to fiber entanglement of hooked fibers. Data Acquisition System (DAQ system) was used to collect the force and displacement data. For the force, data from the built-in load cell for the MTS machine was used, whereas for the displacement data an average of two LVDTs were used. The graphs were plotted as shown below.

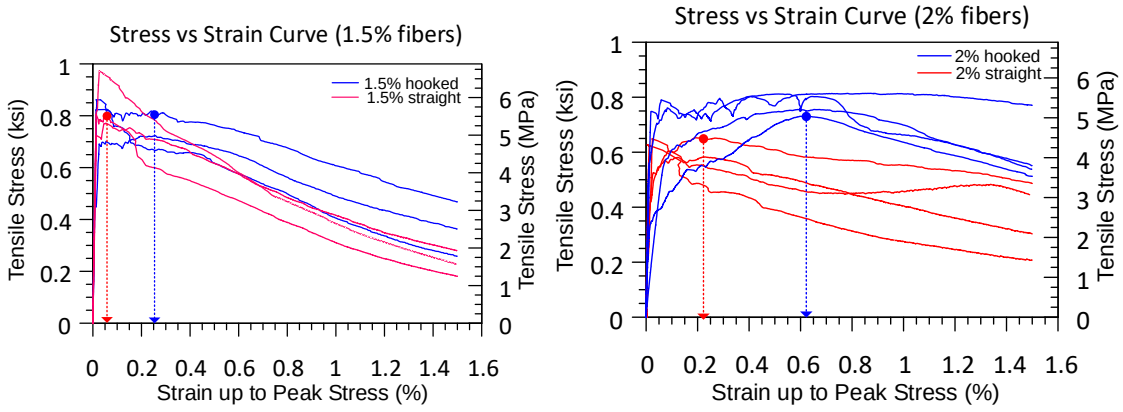

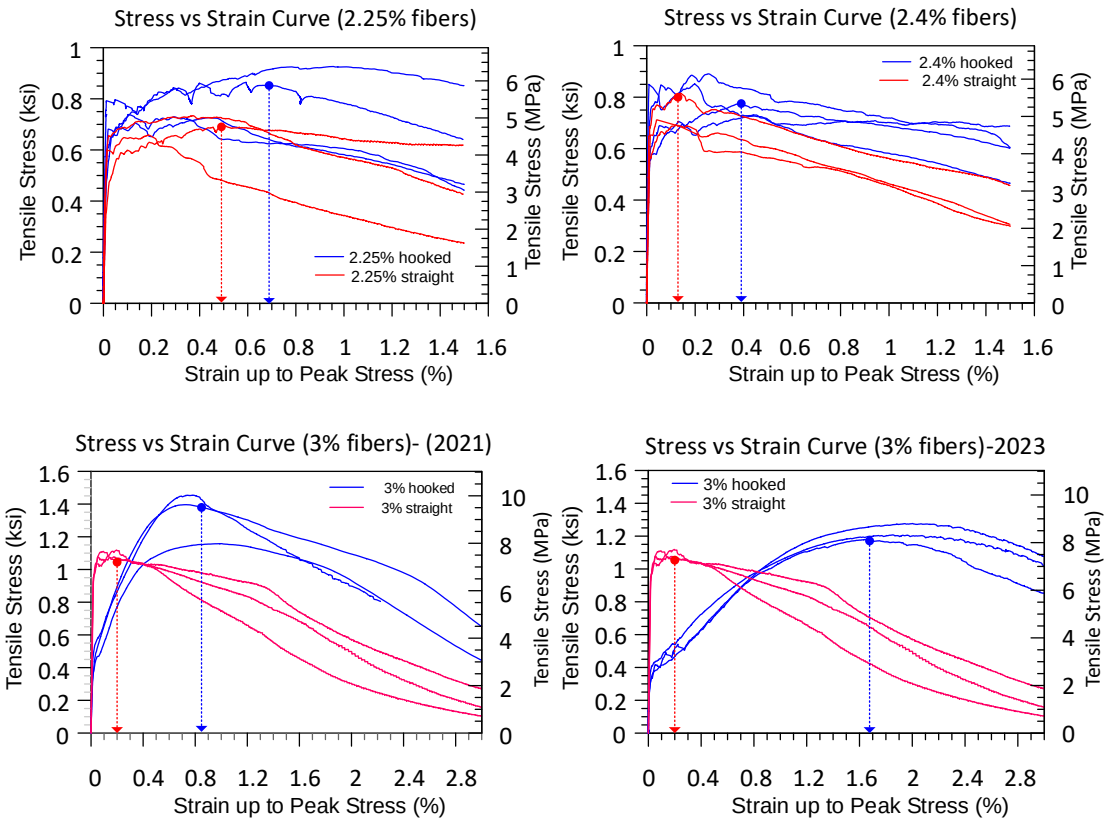

Figure 4-10 Tensile Stress vs Strain curve for (1.5%,2%,2.25%,2.4 and 3%) fiber volumes

Table 4-10 DTT results

Fiber Volume and Type		Peak Stress (ksi)		Average Tensile Stress (ksi) at		
		Peak Stress	COV	1.5% strain	2% strain	3% strain
1.5%	Hooked	0.80	7.2%	0.36	0.25	0.10
	Straight	0.85	10.4%	0.23	0.14	0.03
2%	Hooked	0.77	4.5%	0.59	0.49	0.32
	Straight	0.63	4.5%	0.36	0.27	0.27
2.25%	Hooked	0.79	14.1%	0.6	0.46	0.32
	Straight	0.69	4.5%	0.43	0.38	0.24
2.4%	Hooked	0.81	7.9%	0.59	0.48	0.23
	Straight	0.74	7.3%	0.35	0.22	0.16

3%	**Hooked-2021**	1.34	9.6%	1.14	0.97	0.63
	Hooked-2023	1.22	3.3%	1.19	1.21	0.98
	Straight	1.10	1.7%	0.68	0.46	0.18

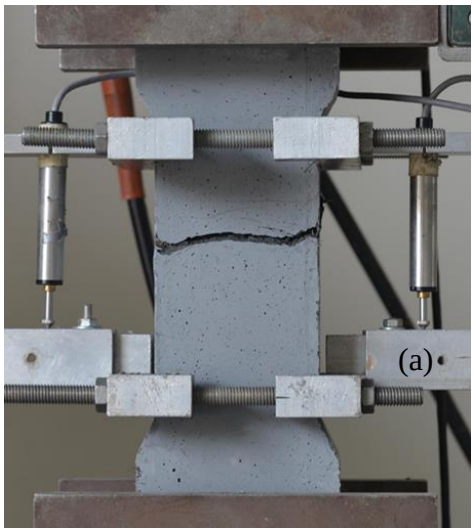
(a)

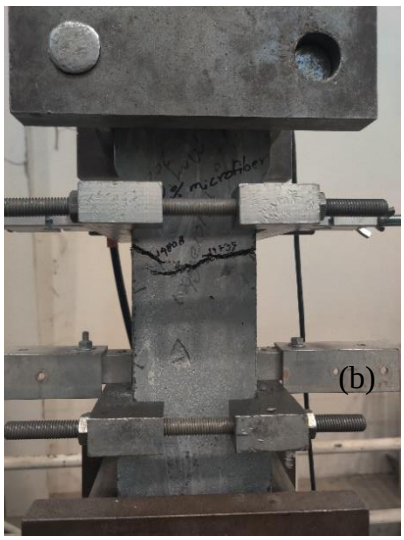
(b)


(c)

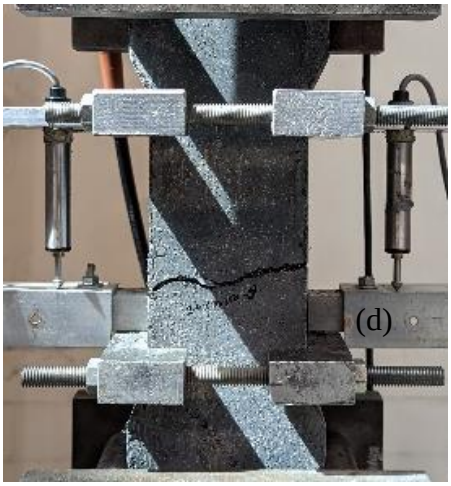
(d)

Figure 4-11 Failure for dog bone samples for straight fibers, a.1.5%, b.2%, c.2.25%, d. 2.4%, e. 3%

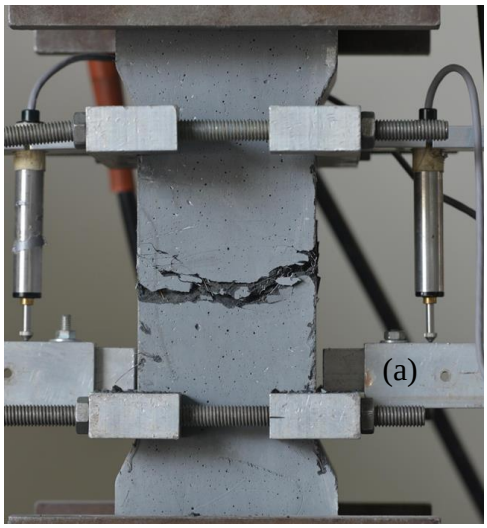

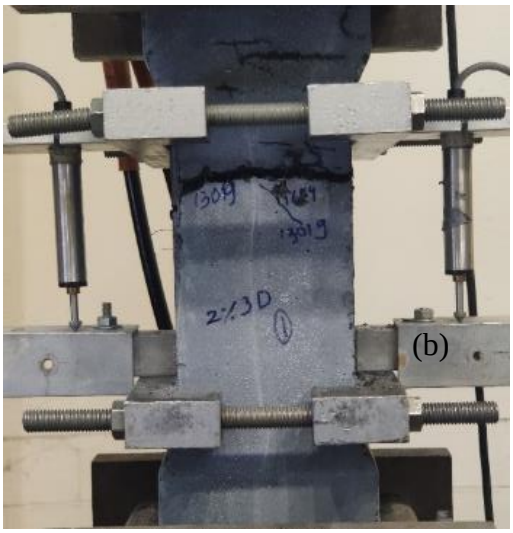

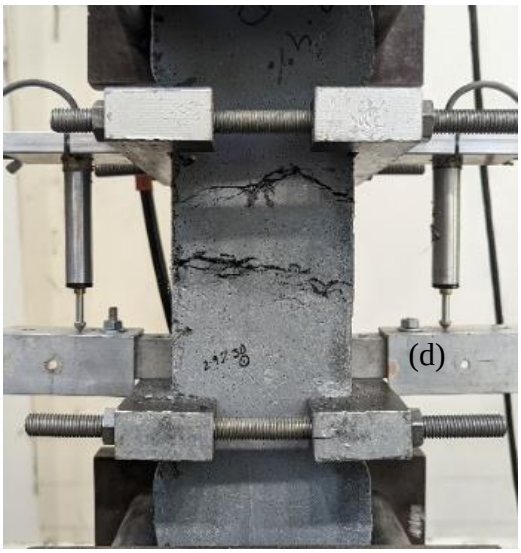

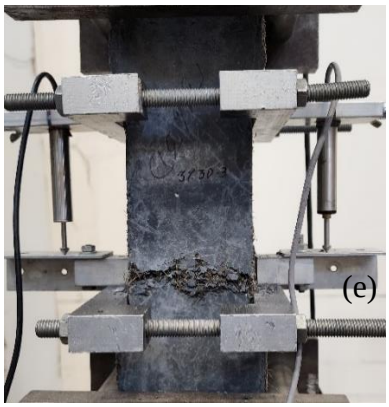

Figure 4-12 Failure for dog bone samples for hooked fibers, a.1.5%, b.2%, c.2.25%, d. 2.4%, e. 3%

Conclusions from the direct tensile test:

- From Figure 4-10, UHPC with high-strength hooked fibers showed higher tensile strength when compared with the straight microfibers for the same volume fraction. This shows the better tensile response for the hooked fibers compared to the straight microfibers.
- UHPC with hooked fibers showed strain capacity at peak stress from 0.3% to 0.6%, compared to 0.1% to 0.4% of straight microfibers, suggesting superior tensile strain capacity. Higher tensile strain capacity means better ductility for the UHPC mix and improvement in the nominal bending capacity of the UHPC members. Maximum tensile strain capacity was observed at 2.25% fiber volume fraction with 0.7% for hooked fibers and 0.5% for straight fibers; however, the values dropped for 2.4% fiber volume fraction, which might be due to a problem with mixing due to fiber entanglement.
- The average Coefficient of Variation (COVs) for the peak stress for all the specimens was 6.8%. Although the tested specimens in this research showed considerably better COVs, previous research suggested higher COVs for the DTT test. So, further study needs to be done to get a clear picture of the result obtained from the DTT test.

  Hooked fibers cast using SIFCON had lower first cracking strength, which might be because of less concrete matrix, but the problem with the less first cracking

strength got compensated by the higher fiber volume to gain higher peak tensile stress.

4.6 Double Punch Test

Double Punch Test was performed for introduction as a good tensile response measurement test. The test result was verified with the results obtained from the direct tensile test and flexural beam test. 6x 12 in. cylinders were cast with 2% and 2.4% fiber volumes for both 3D and microfibers, 3 in each batch. The specimens were cut into half and named top and bottom. The surfaces were smoothened by grinding. The specimens were then used for double punch tests with punches of dimension 1 in. height and 1.5 in. diameter.

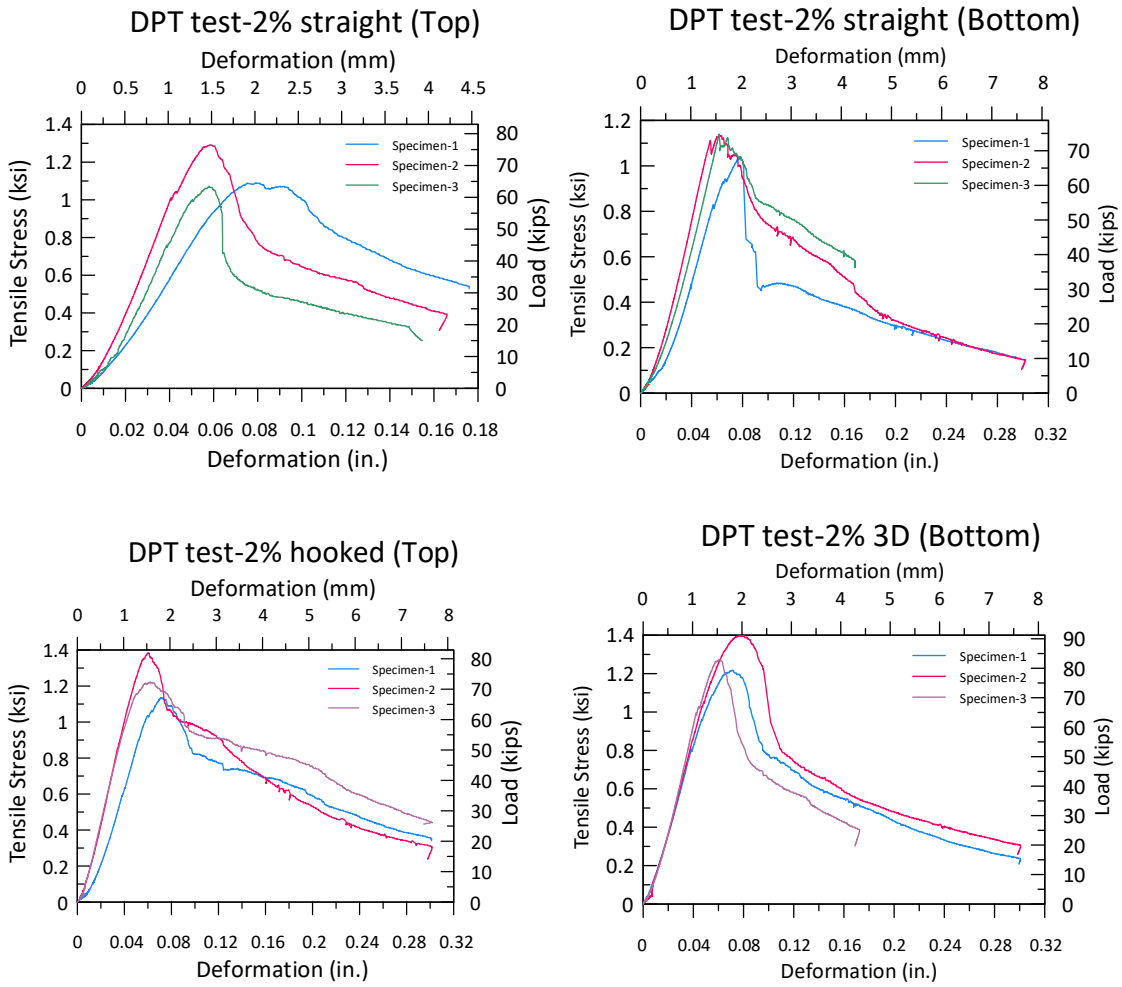

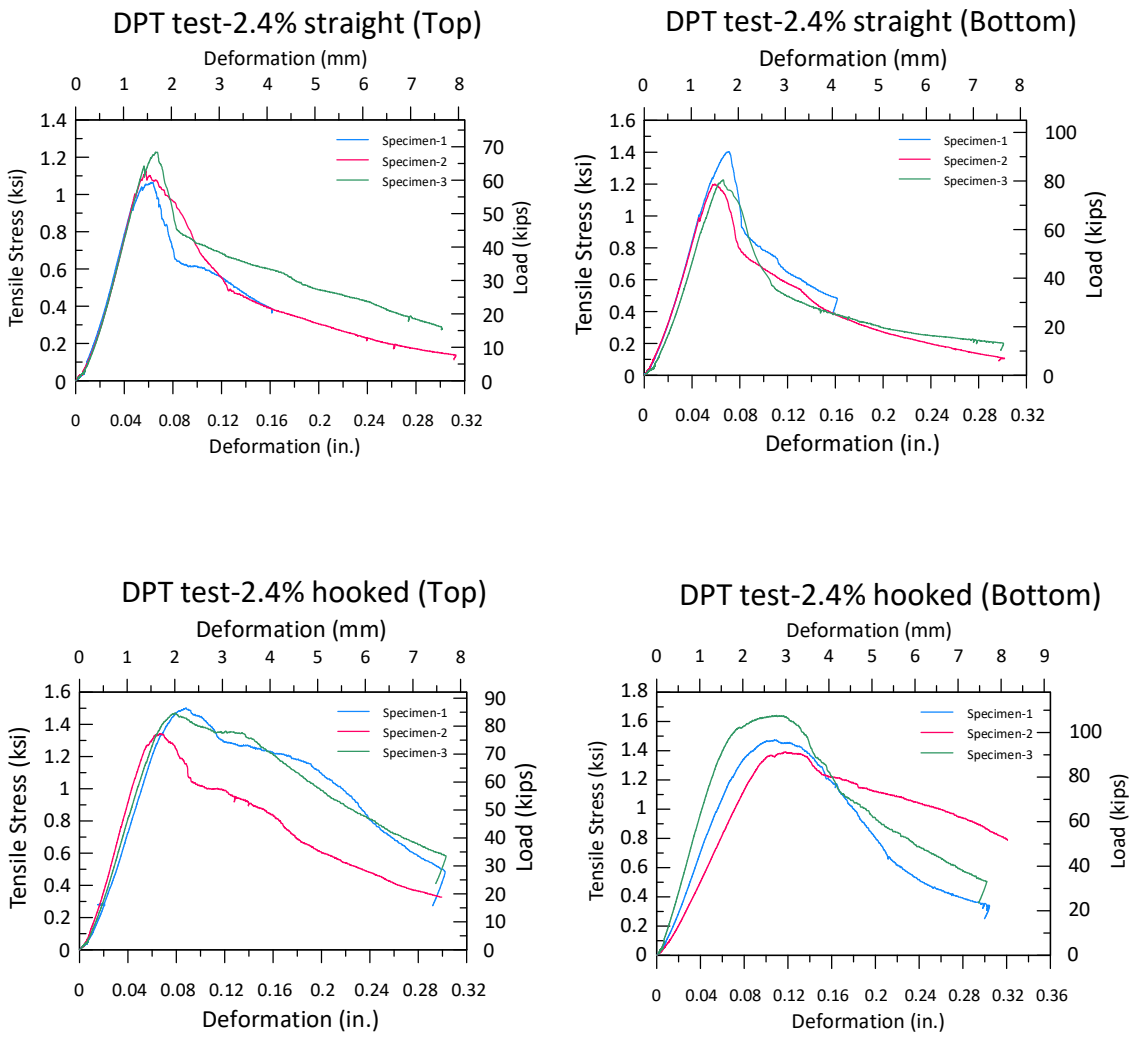

Figure 4-13 Tensile stress vs strain curve for DPT test

Figure 4-14 Sample DPT specimen showing cracks.

Figure 4-15 DPT specimens after testing.

Table 4-11 shows detailed results obtained from DPT tests.

Table 4-11 DPT test results

Fiber Volume and Type		**Peak Stress**		**Deformation-0.1 inch**		**Deformation-0.15 inch**	
		Peak Stress (ksi)	**COV**	**Average Stress (ksi)**	**COV**	**Average Stress (ksi)**	**COV**
2% hooked	**Top**	1.25	8.2%	0.91	7.3%	0.76	7.9%
	Bottom	1.29	5.8%	0.79	15.3%	0.55	12.8%
2% straight	**Top**	1.15	8.6%	0.70	32.2%	0.46	28.9%
	Bottom	1.11	3.7%	0.68	21.8%	0.54	17.5%
2.4% hooked	**Top**	1.44	4.8%	1.28	14.8%	1.13	15.6%
	Bottom	1.5	6.9%	1.48	7.7%	1.29	2.6%
2.4% straight	**Top**	1.14	5.9%	0.69	7.7%	0.48	18.9%
	Bottom	1.28	7.1%	0.70	7.9%	0.45	10.7%

Conclusions from double punch test:

- UHPC with high-strength hooked fibers showed higher peak stress when compared with the straight microfibers for the same fiber volume percentage. Same pattern was observed for the residual strength at 0.1 in. and 0.15 in., where hooked fibers showed higher strength than that with straight fibers.
- Average COVs for peak stress was 6.37%, so double punch test is a good test method for quality control.
- COVs for top and bottom specimens were below 10% for all the fiber volume fractions, meaning fiber density for top and bottom specimens were similar, leading to an average of top and bottom specimens for average computation.

The difficult part of the DPT test was cutting the cylinders in half. Also, extra caution needs to be made to make sure both the top and bottom specimens have COVs below 20%, as fibers might segregate to the bottom of the cylinder. So, the mold was cut in half, and the comparison between the specimens cut in half and the mold cut in half was made. This comparison used normal FRC concrete with a 0.45% volume fraction.

Figure 4-14 Molds cut in half.

Figure 4-15 DPT specimens after failure

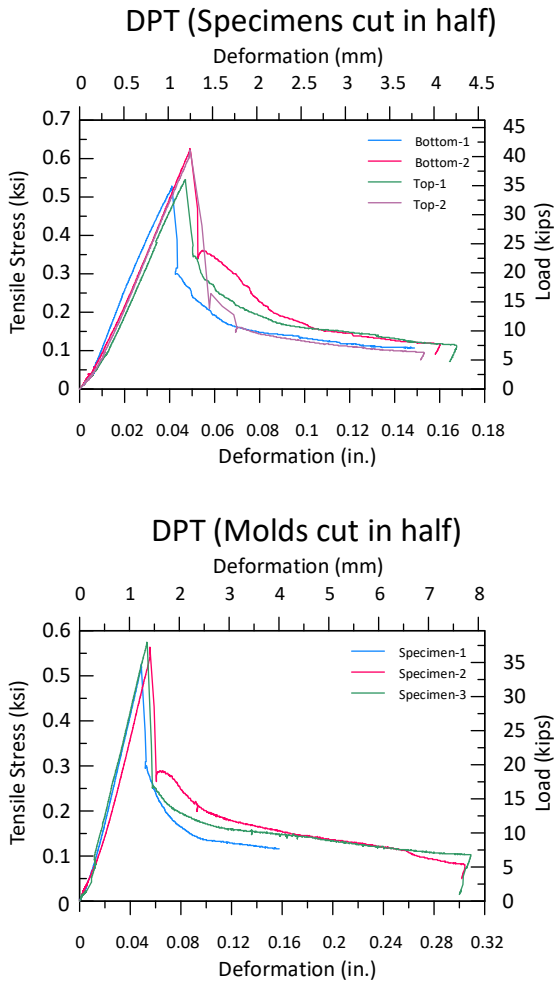

Figure 4-16 Tensile stress vs strain curve (DPT specimens)-specimens cut in half and mold cut in half.

Table 4-12 DPT test result (Specimens cut in half and mold cut in half)

Parameters	Specimens cut in half	Molds in half
Average Maximum Stress	0.58 ksi	0.55 ksi
Coefficient of Variation of Maximum Stress	7.6%	3.85%
Average Deformation at 0.15 inch	0.11 ksi	0.14 ksi

Table 4-12 shows that COVs for the molds cut in half showed consistent results when compared with the specimens cut in half.

4.7 Beam Test (ASTM C1609 test)

For the comparison of tensile response, ASTM C1609 test was performed for specimens with 2% and 2.4% fiber volumes, with each specimen having 4 samples for 3D and microfibers, respectively. For each fiber volume, 4 beam specimens with dimensions 6 in. x 6 in. x 21 in. were cast. The specimens were placed in the curing room for 28 days, and the flexural test was performed following the ASTM standards, ASTM C1609. The test setup for the beam test is shown below. The measurements were taken and stored in Data Acquisition System (DAQ system). The load was obtained from the load cell, and the displacement was obtained as an average from the two LVDTs. The graph was plotted later, for 2% and 2.4% fiber volumes for 3D fiber specimens and microfiber specimens.

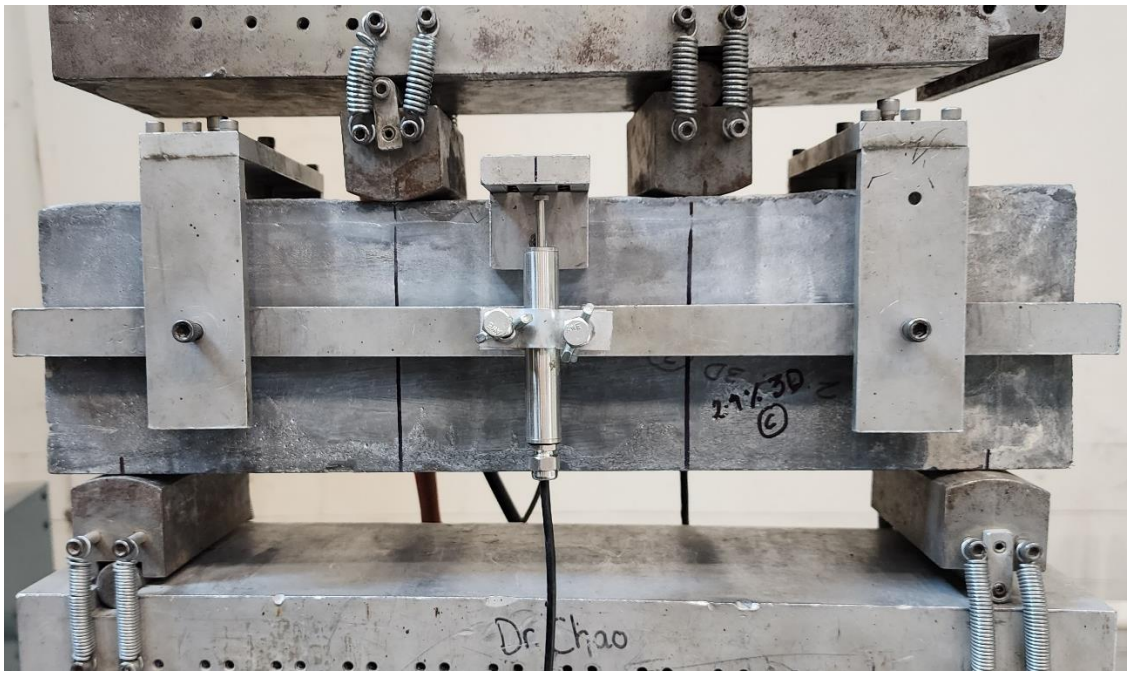

Figure 4-17 Beam test setup

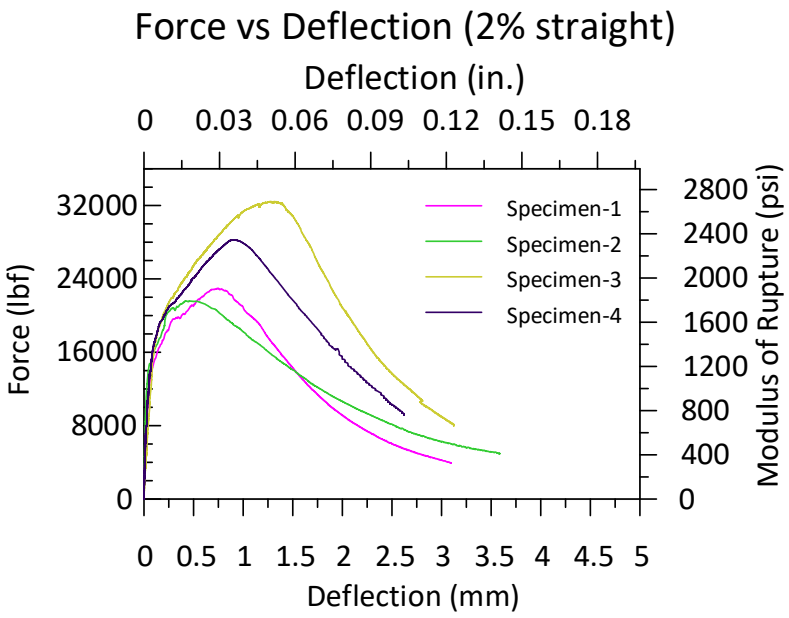

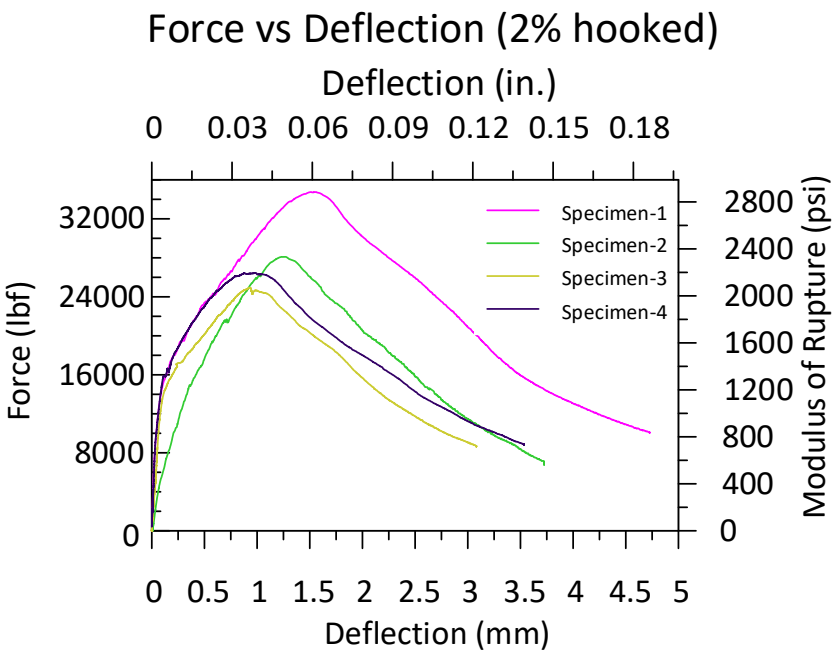

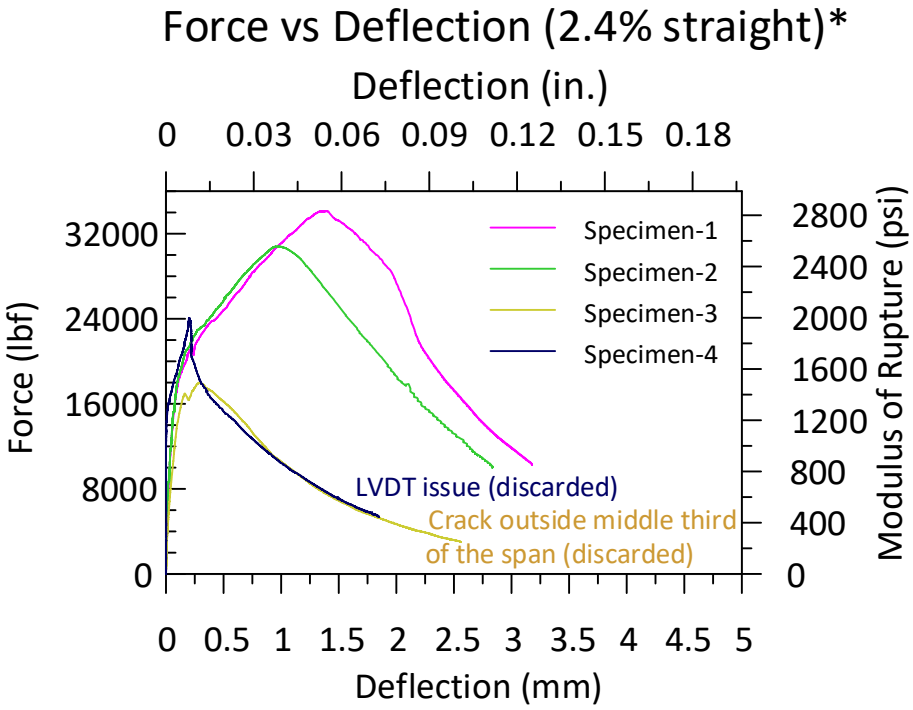

*Out of 4 data, one was discarded because the crack occurred outside the middle third of the span and another had a problem with the LVDT during the testing, so its data was only used for average peak force and COVs of peak force and not in the graph.

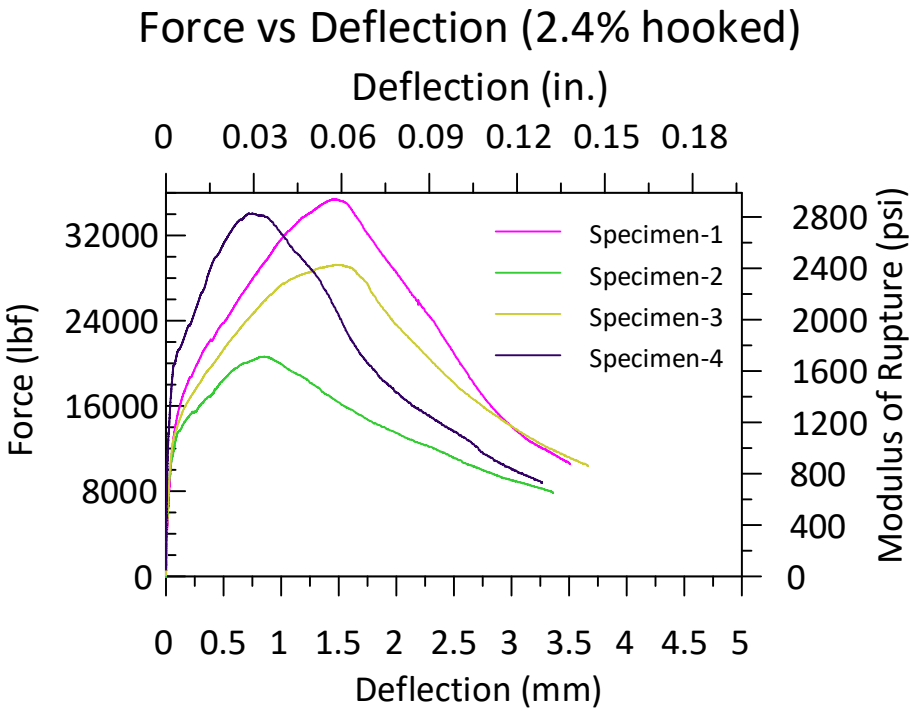

Figure 4-18 Force vs Deflection curve (Flexure test)

Table 4-13 represents a detailed result obtained from the beam testing.

Table 4-13 Beam test results

Fiber Volume and Type	**Average Peak Force**		**Average Force at 2.5 mm Deflection**	
	Peak Force (lbf)	**COV**	**Average Force (lbf)**	**COV**
2% Hooked	26322	16.4%	9558	29.7%
2% Straight	28563	13.1%	16970	31.8%
2.4% Straight	29673	14.1%	15288	13.3%
2.4% Hooked	29839	19.4%	15958	23.9%

Conclusions from the beam testing:

- UHPC with high-strength hooked fibers demonstrated higher peak force than high-strength straight microfibers for a 2% fiber volume fraction. The same observation was seen for residual strength at 2.5 mm deflection with higher peak force than straight microfibers. However, results were similar for a 2.4% fiber volume fraction for hooked and straight fibers, possibly due to fiber entanglement in the mixing process for higher volume fractions.
- Average COVs at the peak load for all specimens at peak load was 15.75%, and the graph for force vs deflection was also scattered and inconsistent. Based on these observations, it can be concluded that the ASTM C1609 test is not suitable for quality control purposes.
- Deflection hardening was observed for all the tested specimens, which is optimal behavior for the beam specimens during failure.

5 ANALYTICAL RESULTS OF BEAM TEST

5.1 Overview

The ASTM C1609/C1609M-19a standard (ASTM, 2019) is a key testing method designed to assess the flexural attributes of fiber-reinforced concrete. It employs a load-deflection curve as a tool to extrapolate specific parameters. This is achieved through experimentation on a beam that is simply supported and subjected to third-point loading. The test quantifies several vital properties of the fiber-reinforced concrete, such as first-peak strength (flexural behavior up to the onset of cracking), residual strength (capacity after cracking), and toughness (energy absorption capacity).

The outcomes derived from this test method serve multiple functions, which lead to a reliable way to compare the efficacy of different concrete mix compositions, contribute to research and development, maintains checks on concrete quality, and ensures the verification of adherence to construction specifications. However, since the ASTM C1609/C1609M test is controlled by displacement (displacement controlled) at two loading points, the assumption that the moment remains constant and a zero-shear condition always exists between the loading points may not hold true. This is attributed to the potential of cracks appearing unpredictably anywhere along the length of the material under the ASTM test. For this reason, the initial portion of the finite element analysis was conducted with the primary goal of inspecting the moment diagram and the shear force diagram by instigating cracks at specific locations within the loading region.

Another assumption is that the plane section remains a plane; hence, a linear strain distribution is required to formulate the equations in ASTM C1609. This requirement might also be questioned for its validity in the context of ASTM beams. This could be attributed to the fact that the beam evaluated for the ASTM C1609 test is a deep beam,

which does not hold the linear strain relationship. Moreover, stress distribution at a distance equivalent to the depth of the member (h) from the concentrated loading point shows discontinuity and is addressed as a D-region in ACI 318-19 (ACI, 2019), which further helps address the issue about equation formulation for ASTM beams. Consequently, in the subsequent segment of the finite element analysis, the strain diagram was visualized along the cross-section to further explore this hypothesis.

5.2 FEA analysis using VecTor3 software

VecTor3(Formwork-plus-v1.0) is an advanced, three-dimensional (3-D) nonlinear finite element analysis (NFEA) program, meticulously engineered for simulating reinforced concrete structures under a broad spectrum of loads. It operates on a pivotal framework that incorporates a 3-D smeared, rotating-crack model, a strategy devised from two authoritative models well known for their analytical capabilities concerning cracked reinforced concrete. These acclaimed models are the modified compression field theory and the disturbed stress field model. Owing to its proven efficacy in the domain of concrete analysis, VecTor3 was judiciously selected as the computational tool utilizing finite element methodology for the analysis of the ASTM C1609 beam in this research.

5.2.1 Concrete Model

The purpose for selecting VecTor3 as the nonlinear finite element analysis (FEA) software for the analysis of beam testing lies in its pre-defined concrete model. This built-in model has been empirically validated to accurately represent the procedures involved in concrete testing. It thoughtfully incorporates fundamental mechanical parameters such as compression and tension, along with the inherent nonlinearity of concrete and its crack-propagation behavior. Within the scope of this analysis, standard

pre-defined parameters were specifically chosen to create an effective model for conventional concrete. Establishing these parameters provides a better understanding of the material's behavior under testing conditions thereby enriching the study with more reliable and comprehensive findings.

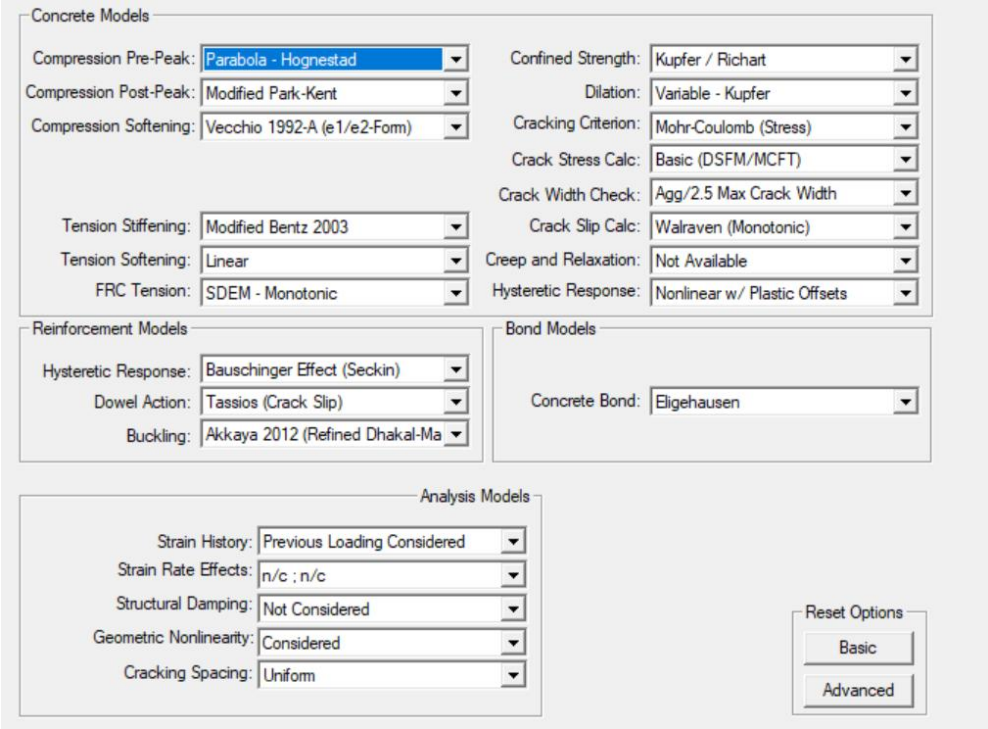

Figure 5-1 Concrete Models using VecTor3 analysis.

5.2.2 FEA model with aligned fiber orientation

An FEA model focusing on aligned fiber orientation represents a preliminary investigation aimed at verifying the zero-shear force and the constant moment condition associated with the ASTM C1609 test. In this case, the selected fibers are 0.38 mm (0.015 in.) in diameter and 25.4 mm (1 in.) in length. Their strength characteristics are modeled using Bekaert 3D 80/30 high-strength steel fiber, which boasts an ultimate strength of 3,070 MPa.

The fibers are systematically arranged so that 11 are aligned along the Y-axis, and 13 along the Z-axis as shown in Figure 5-2. This deliberate arrangement was predicated with the objective of aligning two peak loads: 1) peak load P_1 and 2) peak load P_p with the experimental results obtained from the actual beam test as shown in Figure 5-3. The number of fibers and their orientation were determined with the goal of ensuring a close match between the computational simulation and the empirical beam test data.

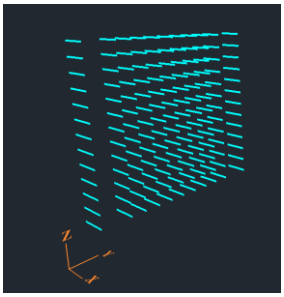

Figure 5-2 Aligned fiber orientation.

(a)

(b)

(c)

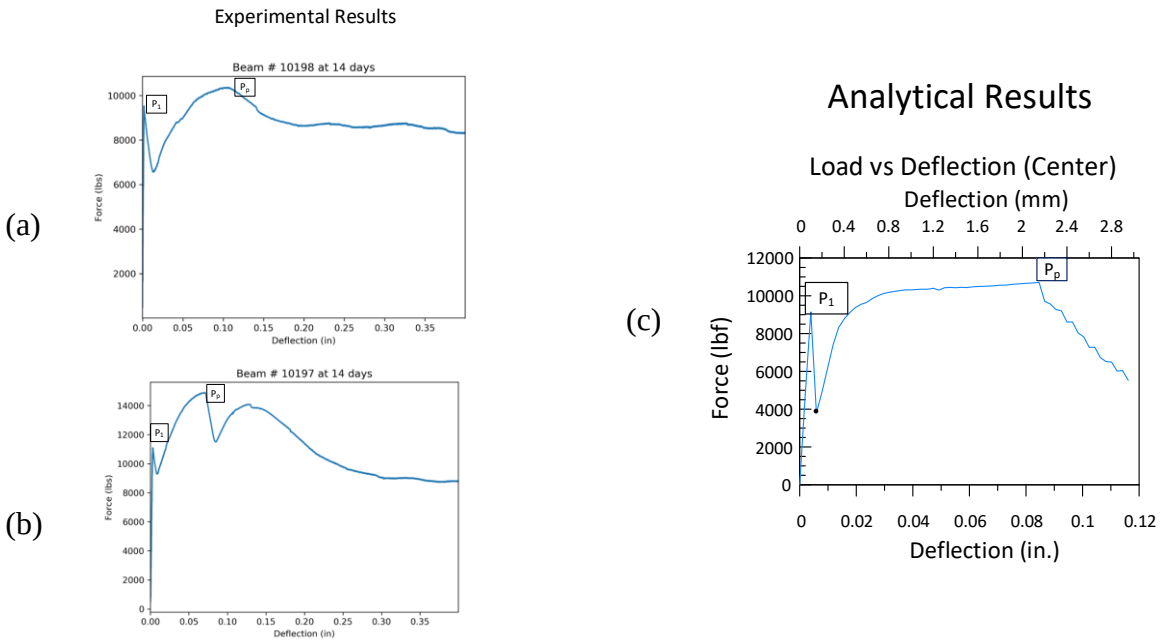

Figure 5-3 Three load vs. deflection graphs: (a) and (b) provide experimental results and (c) analyzes the load vs. deflection results.

Table 5-1 Fiber properties for aligned fiber model

Diameter	Area	Yield Strength (fy)	Ultimate strength (fu)	Elastic Modulus (E)
0.015 in.	0.00018 $in.^2$	420 ksi	445 ksi	29,000 ksi

This FEA represents a preliminary investigation and is succeeded by a subsequent FEA employing random fiber orientation and a configuration more congruent with real-world applications. For this research, the focus was on plotting the shear force and moment diagrams at the lowest point following the first peak load derived from the load-deflection curve. This analysis was applied to each model featuring a central notch, as well as notches placed one inch and two inches from the center,

Each notch has a depth of 0.5 inches (12.7 mm) and a width of 0.039 inches (1 mm) to ensure that cracking will occur along the notch. The notch has a depth equal to the element size of 0.5 inches (12.7 mm) as described previously, although its width is 0.039 inches (1 mm) which is small compared to the element size. Notably, the element has little effect on the analysis results when compared to the beam without the notch. Furthermore, the fibers were strategically placed in the center of the notch. This placement was designed to resist potential cracking, which is made possible by the notch. The fibers were exclusively positioned across the notch to imitate actual conditions; thus, the fibers were mainly situated along the crack to resist cracking.

Fig. 5-4 shows the models with different crack locations used for FEA (i.e., the crack in the center, one inch from the center and two inches from the center of the beam.

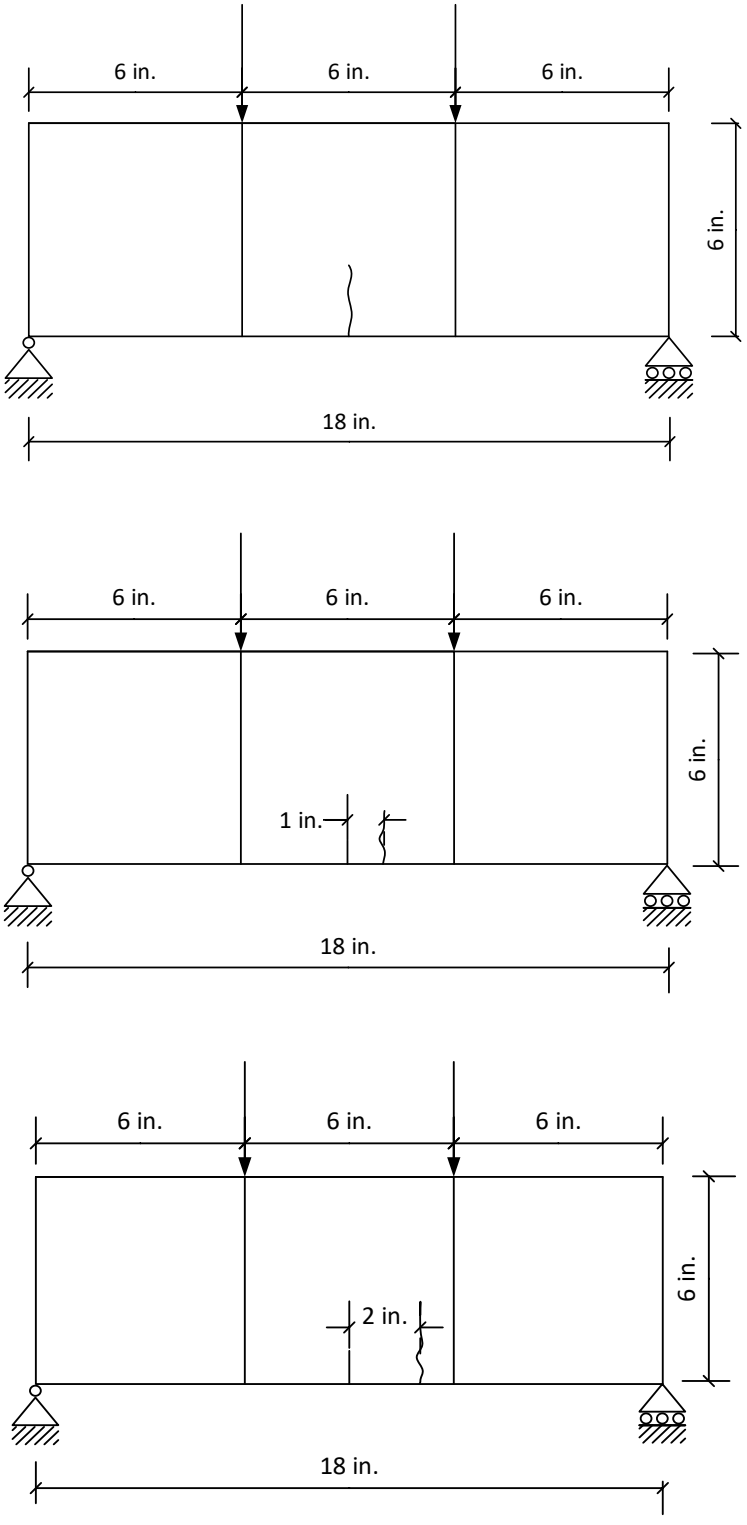

Figure 5-4 Three models with different crack locations

Figure 5-5 is a simple illustration of the ASTM C1609 test with support points, A and D, and loading points, B and C.

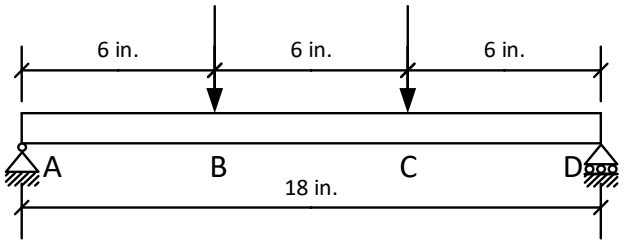

Figure 5-5 Beam with loading points and support conditions

For each model, a crack was intentionally induced at the center, which was nine inches from the hinge support), and one inch from the center, which was 10 inches from the hinge support. A crack was also induced two inches from the center, which is 11 inches from the hinge support. The corresponding reaction forces were then taken from the FEA model, as shown in Table 5-2 to illustrate the shear force diagram and the moment diagram, providing critical insights into the structural behavior based on our models' specific crack distance from center conditions.

Table 5-2 Reactions (RA, RB, RC and RD) at loading points for each model

Reactions at loading points A, B, C, & D	**Distances from the Hinge Support**		
	9 in.	**10 in.**	**11 in.**
R_A	1904 lbf	3254 lbf	4235 lbf
R_B	-1910 lbf	-4362 lbf	-6023 lbf
R_C	-1893 lbf	-1063 lbf	-640 lbf
R_D	1899 lbf	2161	2441 lbf

Analysis Results

FEA models with different notch placements were analyzed; then, a force-deflection graph was plotted along with shear force and moment diagrams.

i. FEA model with notch at the center of beam

In this model, a notch is created which forces cracks to occur at the center of the beam.

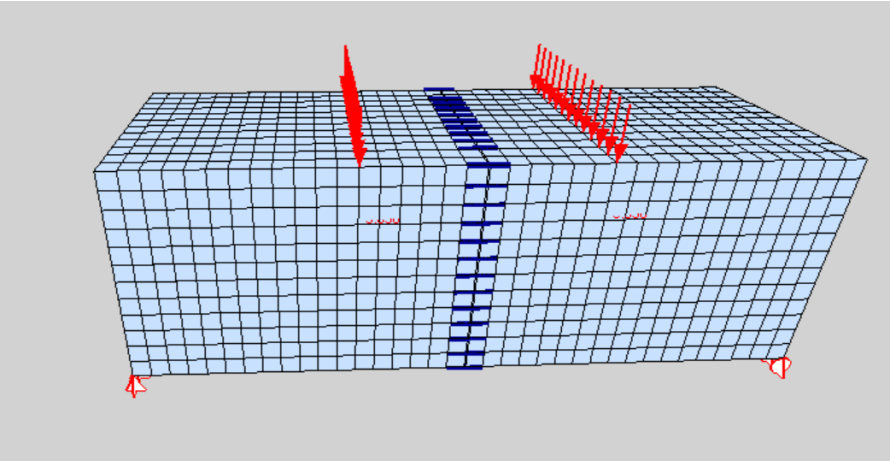

Figure 5-6 FEA model with notch at the center of the beam

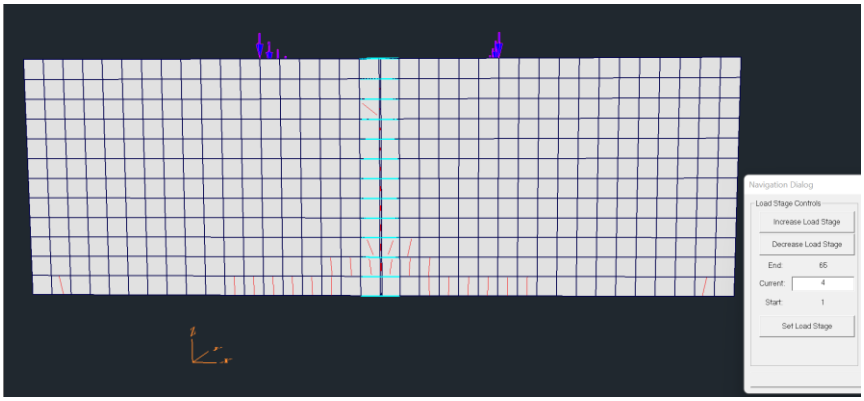

Figure 5-7 Cracks at Load Stage 4 (i.e., lowest point after the first peak in load-deflection graph)

Both Figs. 5-6 and 5-7 models have a centrally placed notch. Fig.5-6 demonstrates the analytical model, while Fig. 5-7 displays the cracks in the FEA model at Load Stage 4,

which is in line with the lowest point following the initial peak in the load-deflection graph, as indicated in Figure 5-8.

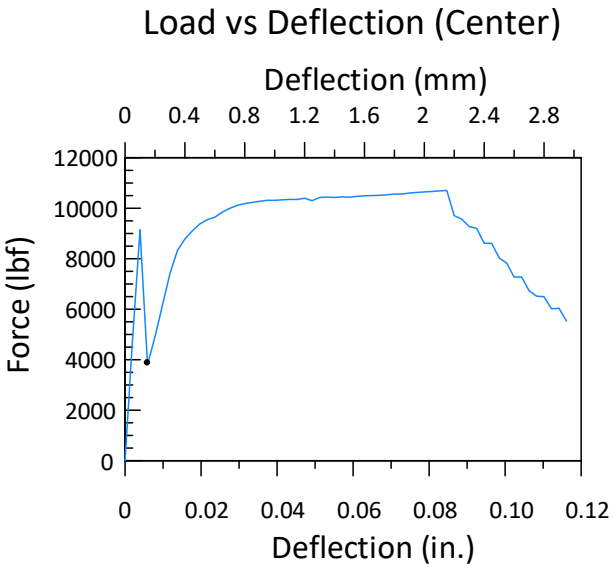

Figure 5-8 Force vs deflection graph

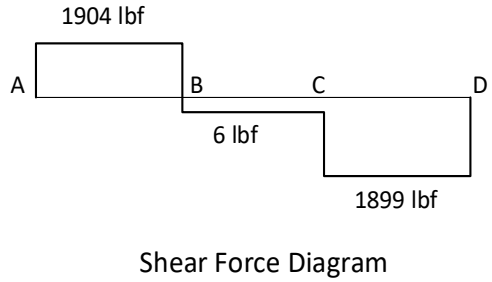

(a)

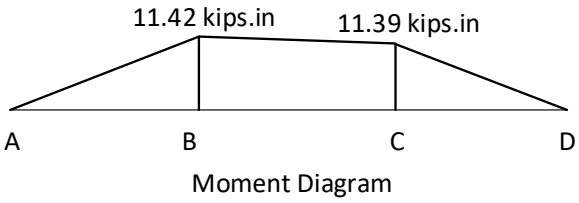

(b)

Figure 5-9 (a) Shear force diagram and (b) moment diagram

Fig. 5-9 shows the shear force diagram and moment diagrams plotted at the lowest point after the drop from the first peak point (P_1) for the load-displacement graph. Fig. 5-9 (a)

shows the zero shear force condition and Fig. 5-9 (b) shows that the constant moment criteria has been met for this FEM model with the crack occurring at the center of the beam.

ii. Model with the notch one inch from the center of beam

In this model, a notch is created that forces cracks to occur one inch from the center of the beam.

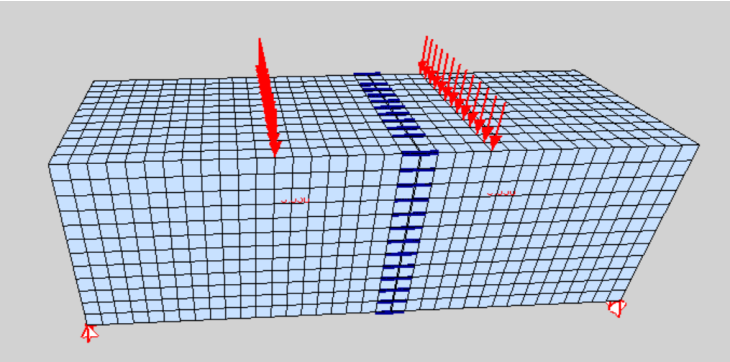

Figure 5-10 FEA model with notch one inch from the center of the beam

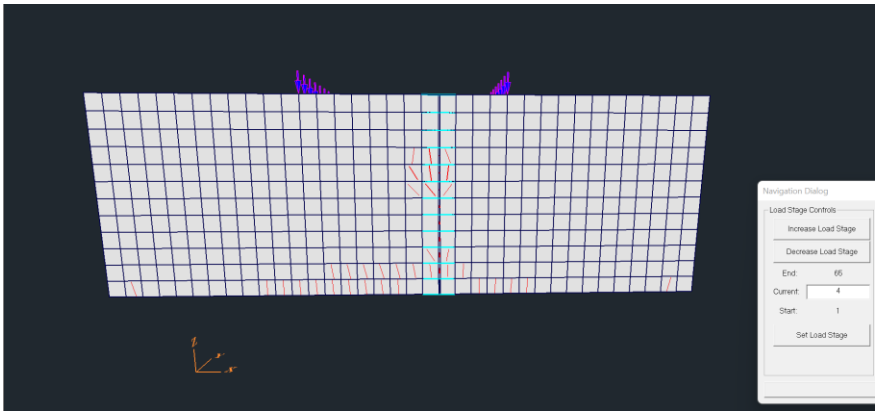

Figure 5-11 Cracks at Load Stage 4 (i.e., lowest point after the first peak in the load-deflection graph)

Figures 5-10 and 5-11 depict the model with a notch positioned one inch from the center of the beam. One figure presents the analytical model, while the other illustrates the

cracks in the FEA model at Load Stage 4, which corresponds to the lowest point following the first peak in the load-deflection graph, as demonstrated in Figure 5-12.

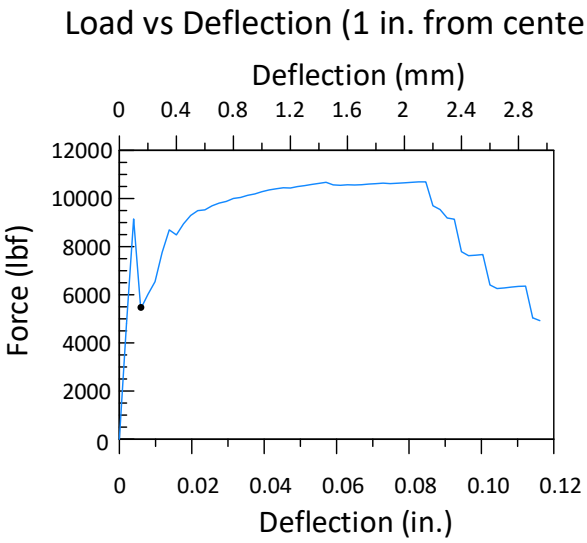

Figure 5-12 Load vs deflection curve for FEM model with crack one inch from the center of the beam

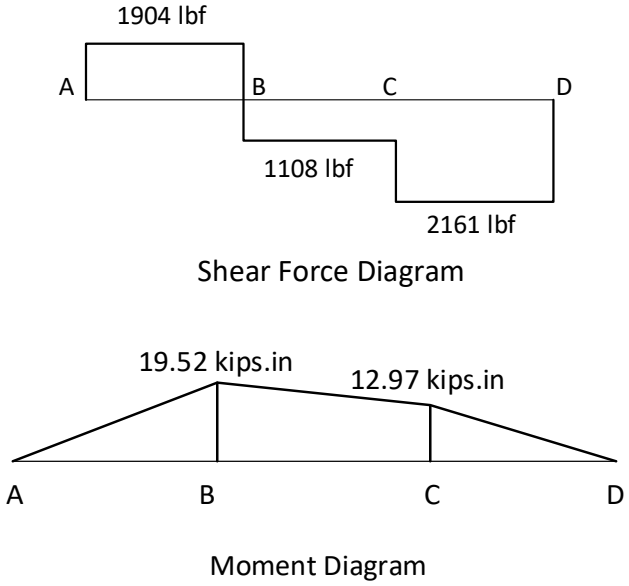

Figure 5-13 Shear force diagram and moment diagram

Figure 5-13 displays the shear force diagram and moment diagram. Both plotted for the lowest point after the drop from the initial peak point (P_1) in the load-displacement graph.

The diagram suggests that the zero-shear force condition and constant moment criteria are not satisfied in this FEM model, where a crack is induced one inch from the beam's center. A noticeable shear force appears to exist along the loading point, assisted by varying moments at loading points, B and C.

iii. Model with notch two inches from the center of beam

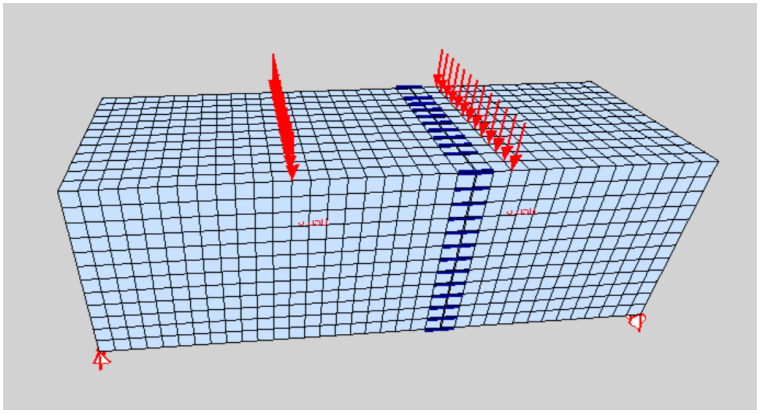

Figure 5-14 FEA model for notch two inches from the center of the beam

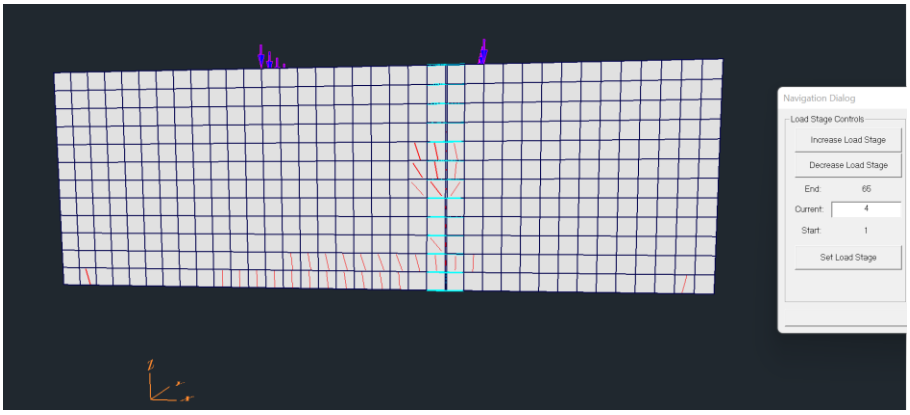

Figure 5-15 Cracks at the Load Stage 4 (i.e., lowest point after the first peak in load-deflection graph)

Figures 5-14 and 5-15 depict the model with a notch positioned two inches from the center of the beam. One figure presents the analytical model, while the other illustrates

the cracks in the FE model at Load Stage 4, which corresponds to the lowest point following the first peak in the load-deflection graph, as demonstrated in Figure 5-16.

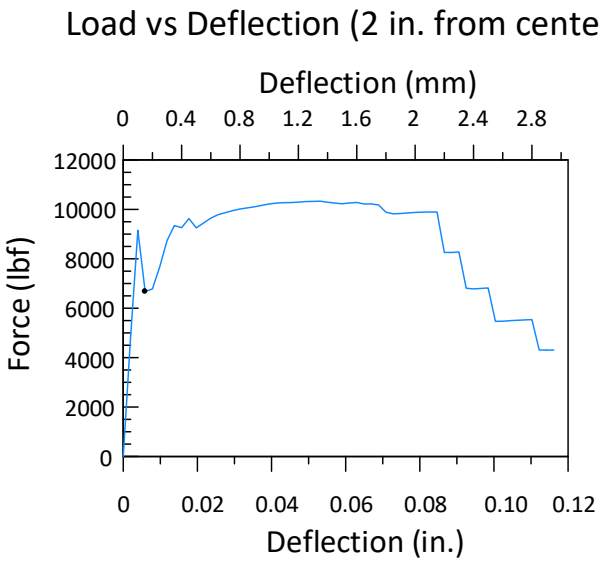

Figure 5-16 Load vs deflection curve for FEM model with crack two inches from center of beam

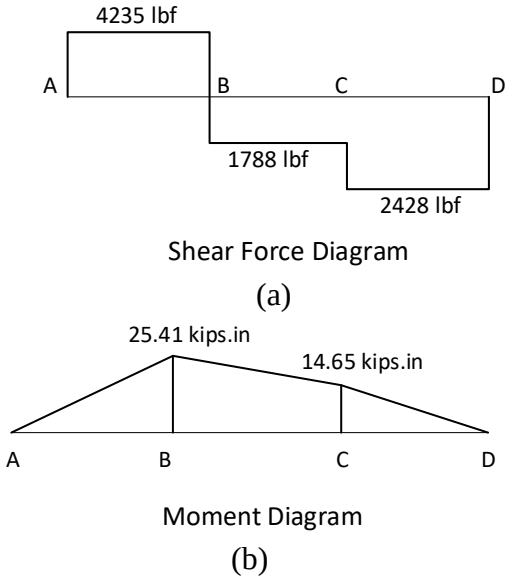

Figure 5-17 (a) Shear force diagram and (b) moment diagram

Figure 5-17 presents the shear force and moment diagrams, both of which are plotted for the lowest point following the drop from the initial peak point (P_1) on the load-displacement graph. For the model with a crack positioned two inches from the center, a

substantial shear force along the loading point forms and varying moments at Loading Points B and C are noticeable. It is also noteworthy that as the location of the crack deviates further from the center of the beam, there is an increase in the shear force between the loading points. This observation calls into question the calculations underlying the ASTM C1609 test, which does not factor in the location of the crack in its foundational calculations for the test.

5.2.3 FEM model with random fiber orientation

In this study, an analytical model was established based on a 6” × 6” × 18” concrete beam, adhering to ASTM C1609 standards for testing. The beam was subjected to four-point loading, with each load intentionally applied at one-third the length of the beam. The chosen finite element for the concrete was a hexahedral unit with an element size of 0.5 inch (12.7 mm).

For the boundary conditions, a simply supported restraint was employed at both ends of the beam, and a load was strategically placed at one-third of the beam’s length. The selected concrete material boasted a compressive strength of 6 ksi and a tensile strength of 0.581 ksi, while all other parameters defaulted to their standard values. The primary objective of the finite element analysis (FEA) was to accurately replicate the behavior of a fiber-reinforced concrete beam in a computational model. Drawing insights from the preliminary FEA analysis of the model with an aligned fiber arrangement, as discussed in Section 5.2.2, it was observed that the conditions of the zero-shear force and constant moment might not be attained as postulated. Consequently, an FEA analysis featuring a model with a randomly oriented fiber placement, which mimics real-world conditions

was conducted. This analysis serves as a detailed investigation, building on the insights gleaned from the preliminary analyses reported in Section 5.2.2.

Fibers were modeled as truss elements with a diameter of 0.75 mm and a length of 50 mm. Their placement within the concrete matrix was randomized to mimic real-world scenarios. Furthermore, the positioning of the fibers was strategically placed in the center of the notch. This placement was designed to resist potential cracking instigated through the notch. The fibers were exclusively positioned across the notch to imitate actual conditions, where the fibers were mainly situated along the crack. Once placed, the fibers formed a natural resistance to the crack.

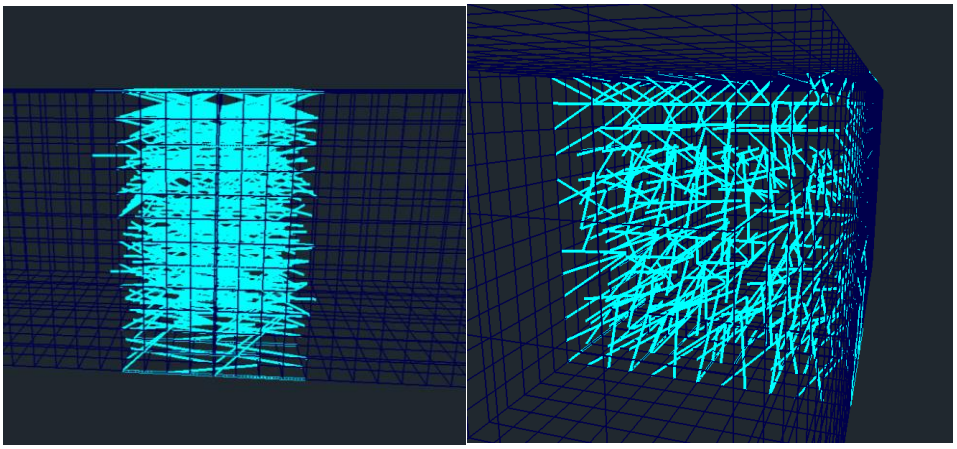

Figure 5-18 Fiber orientation in the VecTor3 model

To initiate cracking within the loaded points, three models were constructed featuring notches located at 9 inches, 10 inches, and 11 inches from the hinge support, respectively. In other words, these notches were positioned at the beam's center and the others were offset from the beam's center by one inch and 2 inches, which corresponded to the parameters set for this research.

Fibers were scattered randomly with a 0.35% fiber volume fraction, maintaining the same fiber orientation across all models as depicted in Fig. 5-18. The orientation and the properties of the fibers were designed to approximate our in-lab experimental results.

Table 5-3 Fiber properties used in UTA research group's analysis.

Diameter	Area	Yield Strength, fy	Ultimate strength, fu	Elastic Modulus, E
0.029 in.	0.0007 in.^{2}	217 ksi	319 ksi	29000 ksi

Experimental Results

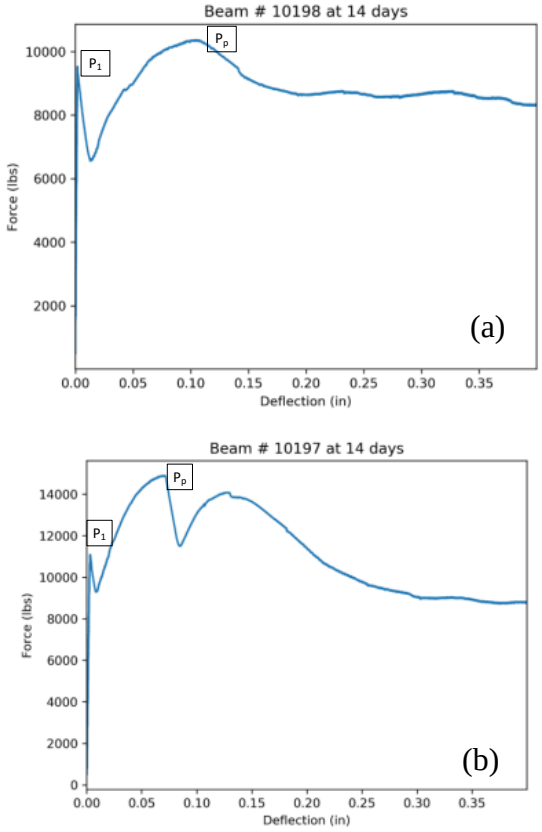

Analytical Results

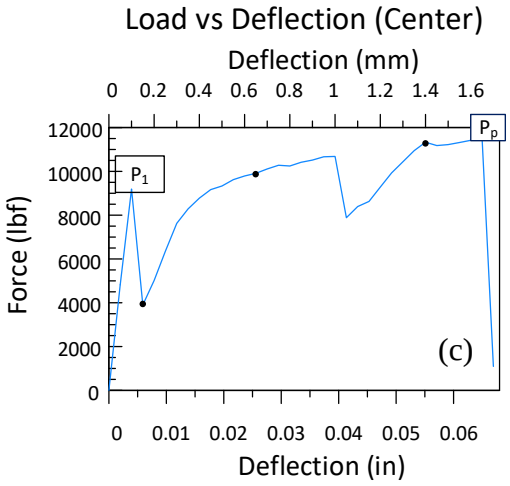

Figure 5-19 Load vs deflection graphs with (a) and (b) experimental results and (c) analytical results

Since the experimental results vary a lot based on specimen cracking while testing, as well as fiber orientation and other factors, the objective was to match the first peak load (P_1) and the peak load (P_p) with the fiber orientation and the fiber properties as shown in Figure 5-19. Once the fiber orientation was fixed, the same orientation was replicated in all the other models.

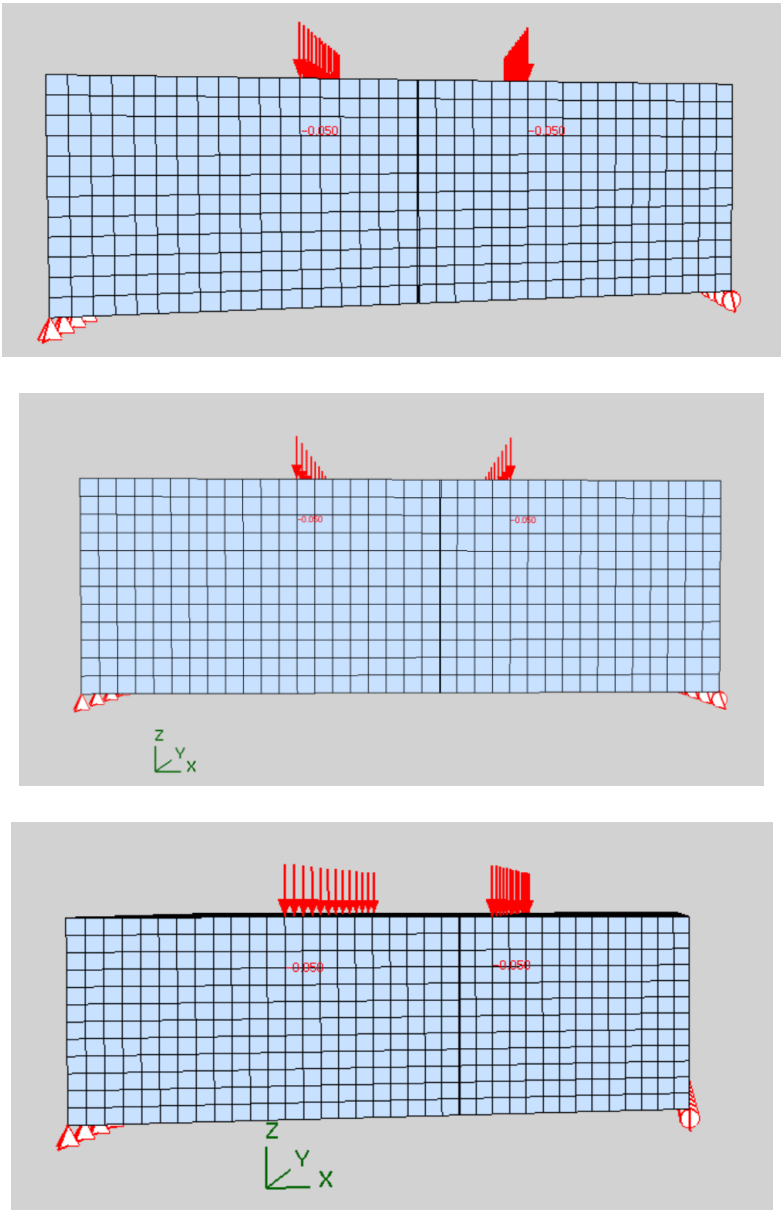

Figure 5-20 FEA model with different notch location

Analytical Results

5.2.3.1 Model with a notch at the center

In this model, cracks are forced to occur at the center of the beam with the help of a notch at the center.

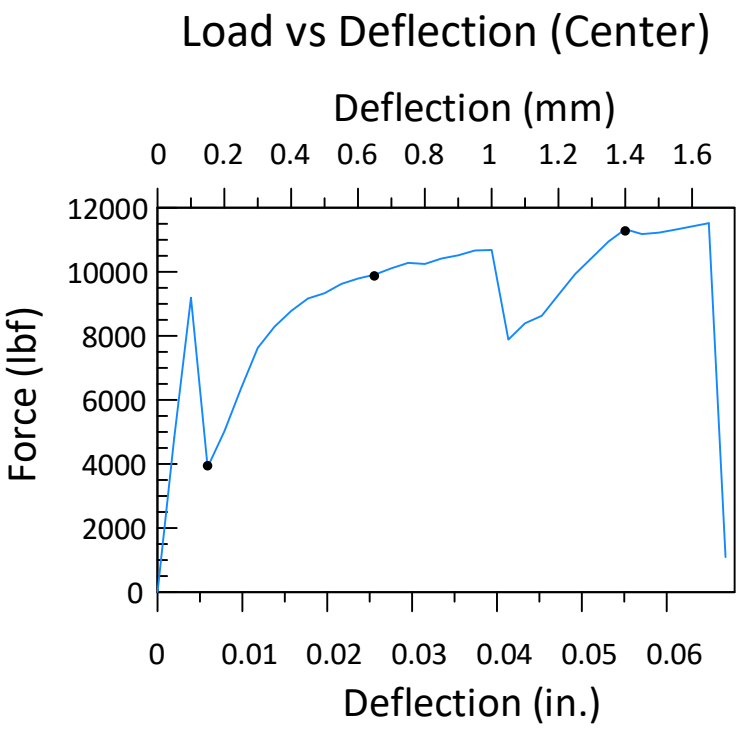

Figure 5-21 Load vs deflection graph

From Figure 5-21, the shear force diagram and moment diagram have been extracted from the force vs deflection curve at three randomly chosen points. Specifically, these points are located at the lowest point following the first peak (corresponding to a loading stage of 0.15 mm (0.006 in.)), and at loading stages of 0.65 mm (0.026 in.) and 1.4 mm (0.055 in.), as indicated in the preceding graph. The loading stages signify the

displacement of the loading points as the test is displacement controlled, and the 0.15 mm loading stages correspond to the 0.15 mm displacement of the loading points, B and C.

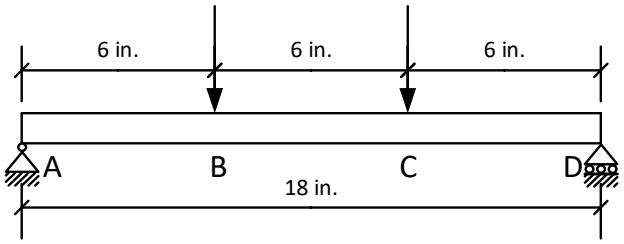

Figure 5-22 ASTM beam test condition

Table 5-4 shows the reactions in the beam at the A, B, C and D points shown in Fig. 5-22 in response to the displacement load as defined by each loading stage.

Table 5-4 Reactions at each loading stage

Loading stages / **Reactions**	**0.15 mm (0.006 in.)**	**0.65 mm (0.026 in.)**	**1.4 mm (0.055 in.)**
R_A	1965 lbf	4942 lbf	5659 lbf
R_B	-1993 lbf	-4914 lbf	-5630 lbf
R_C	-1908 lbf	-4995 lbf	-5685 lbf
R_D	1936 lbf	4970 lbf	5673 lbf

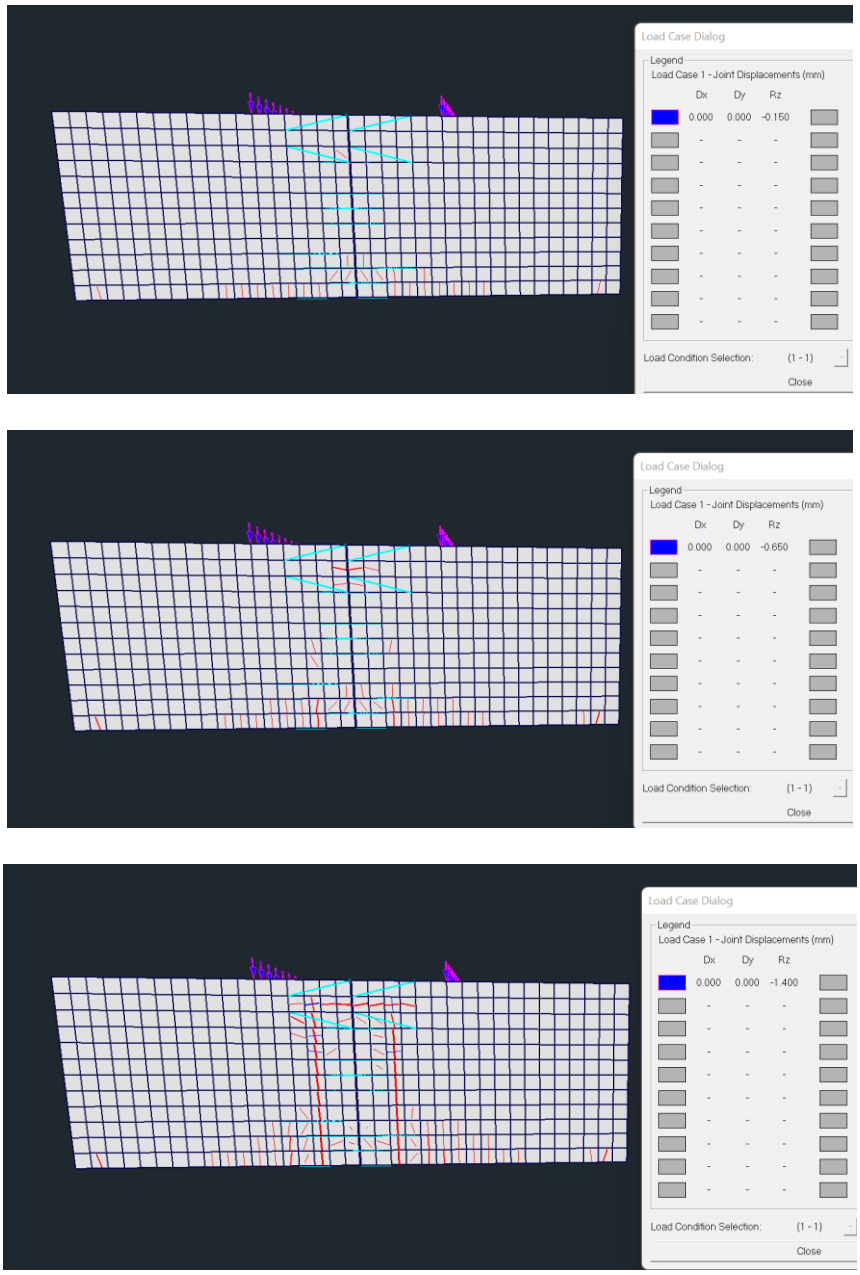

Figure 5-23 Cracking patterns at different loading stages

a. Loading stage 0.15 mm (0.006 in.)

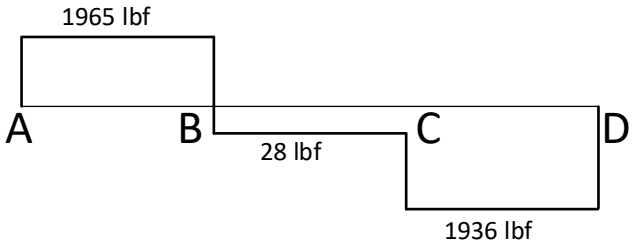

Shear Force Diagram

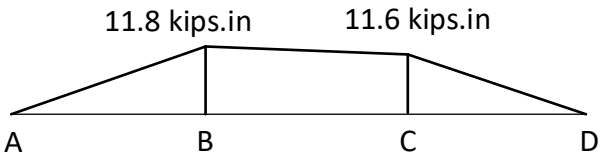

Moment Diagram

Figure 5-24 Shear force diagram and moment diagram

As illustrated in Figure 5-24, under displacement-controlled loading circumstances, when the displacement value for loading points B and C reaches 0.15 mm (0.006 in.), the shear force observed between these points becomes zero. This observation is supported by nearly constant values of the moment at the respective B and C loading points.

b. Loading stage 0.65 mm (0.026 in.)

Figure 5-25 delineates a displacement value of 0.65 mm (0.026 in.) under displacement-controlled loading conditions. The results show an almost negligible shear force between the loading points, like the earlier observed loading stages of 0.15 mm. The consistency of this phenomenon is further substantiated by the constant value of the moment

identified at the B and C loading points, which reconfirms the near absence of shear force under these specified conditions.

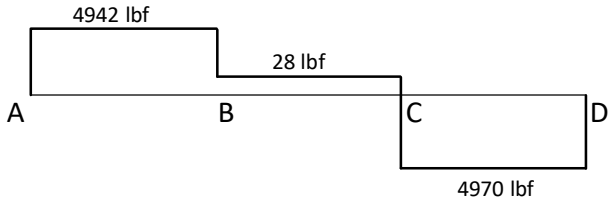

Shear Force Diagram

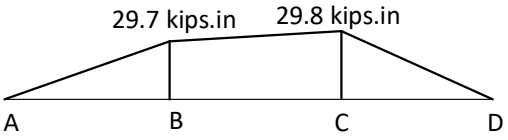

Moment Diagram

Figure 5-25 Shear force diagram and moment diagram

c. Loading stage 1.4 mm (0.055 in.)

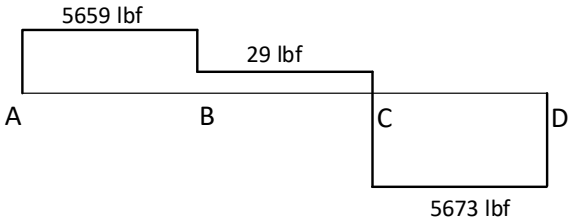

Shear Force Diagram

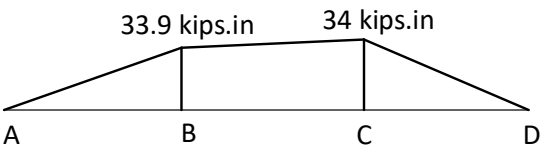

Moment Diagram

Figure 5-26 Shear force diagram and moment diagram

Figure 5-26 shows a similar condition at the loading stage of 1.4 mm (0.055 in.), where the shear force approximates zero and the moment between the loading points remains constant, further reiterating the consistency of these observed phenomena across different displacement values.

5.2.3.2 Model with notch one inch from center

In this model, cracks are forced to occur one inch from the center of the beam with the help of a notch. After that, the load vs deflection curve is plotted, and shear force and moment diagrams are plotted at different loading stages as shown in Fig. 5-27.

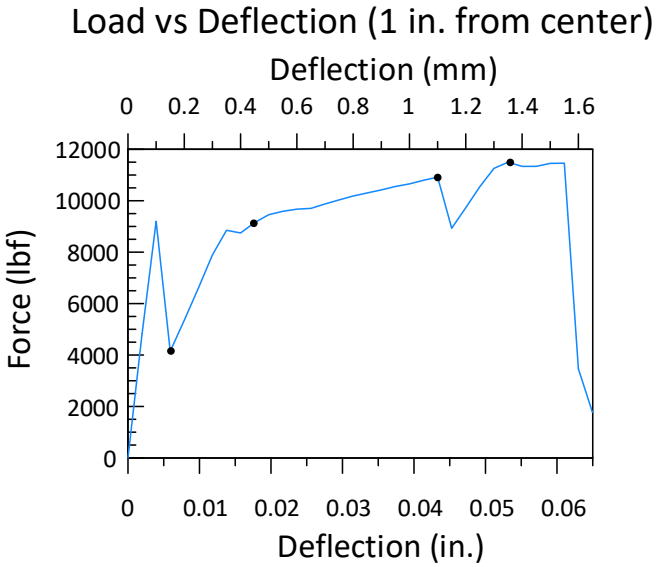

Figure 5-27 Load vs deflection graph

In this model, cracks are intentionally induced one inch from the beam's center utilizing a notch. This allows us to create a graph showing the correlation between load and deflection, as well as concurrent diagrams representing shear force and moment, constructed at distinct loading stages as shown in Fig. 5-27.

The shear force diagram and moment diagram were derived at three arbitrarily selected locations: The first location is at the lowest point after the 1st peak, showing the loading stage at 0.15 mm or 0.006 in. The second location is after the second peak, showing the loading stages of 0.45 mm or 0.018 in. The third location is after the third peak with a loading stage of 1.1 mm or 0.043 in., and the fourth location is after the fourth peak with a loading stage of 1.35 mm or 0.053 in. In this context, these loading stages correspond to the displacement of the loading points under the displacement-controlled loading condition.

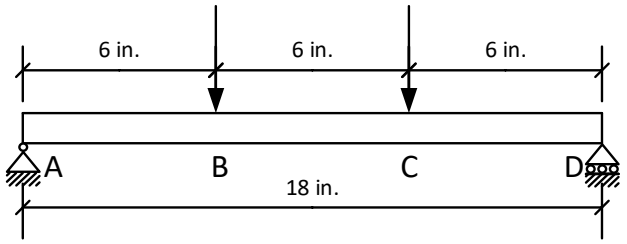

Figure 5-28 shows cracking at each displacement of the loading points.

Table 5-5 Reaction at each loading stage

Loading stages / Reactions	**0.15 mm or (0.006 in.)**	**0.45 mm or (0.018 in.)**	**1.1 mm or (0.043 in.)**	**1.35 mm or (0.053 in.)**
R_A	2692 lbf	5261 lbf	5484 lbf	5812 lbf
R_B	-3929 lbf	-6617 lbf	-5532 lbf	-5908 lbf
R_C	-219 lbf	-2546 lbf	-5376 lbf	-5568 lbf
R_D	1455 lbf	3891 lbf	5435 lbf	5686 lbf

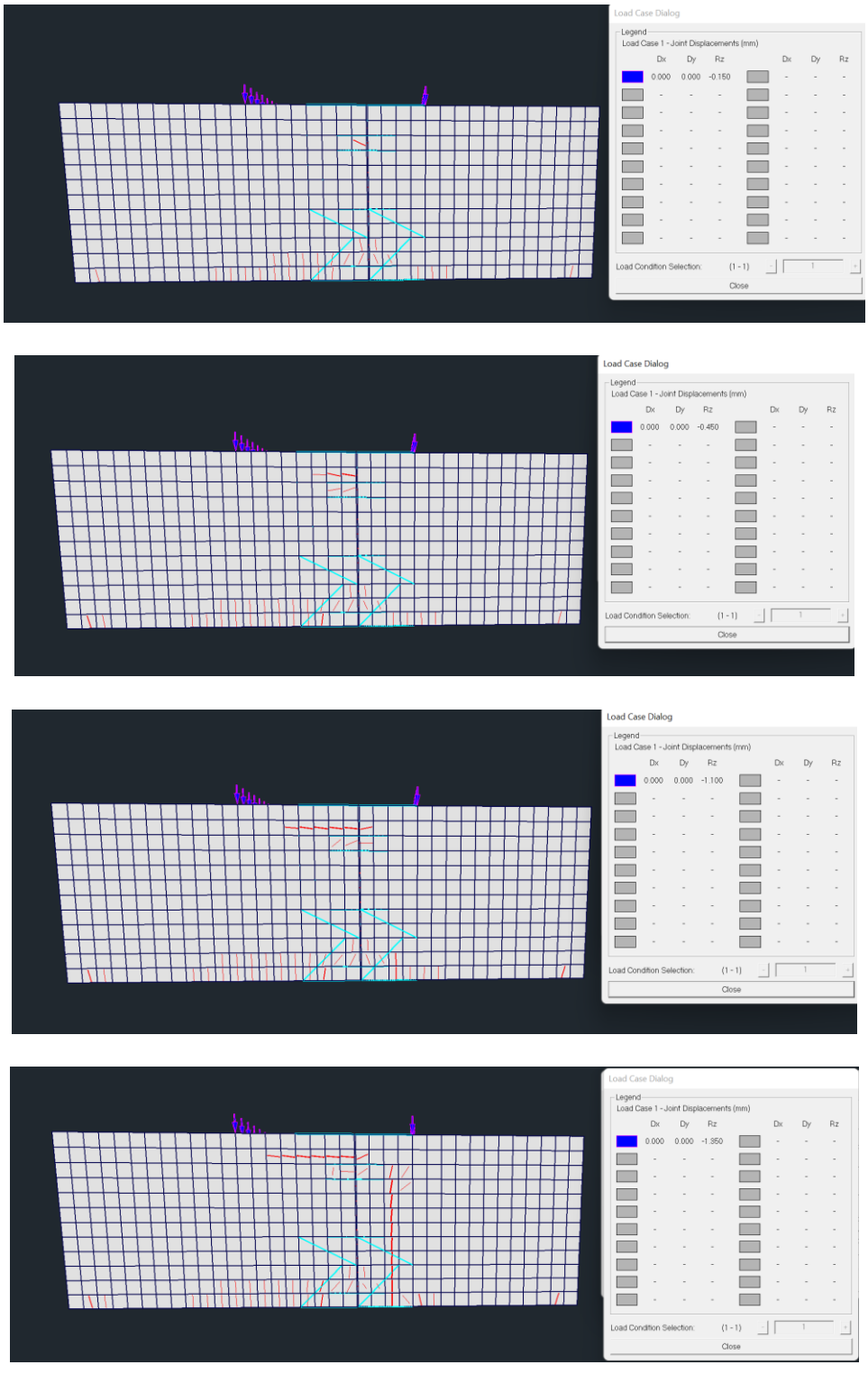

Figure 5-28 Cracking is shown here at every loading stage

a. Loading stages at 0.15 mm (0.006 in.)

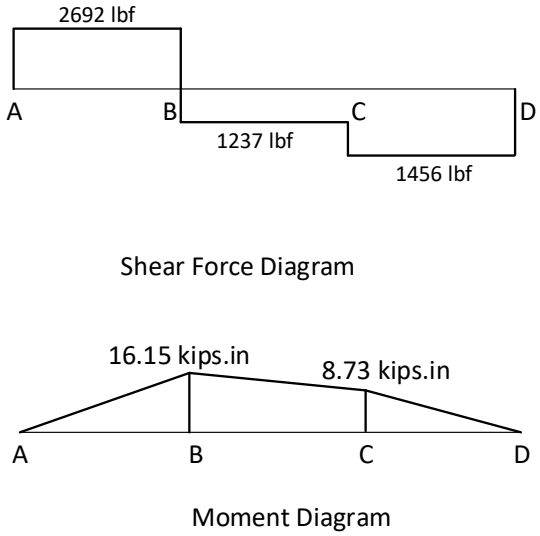

Figure 5-29 Shear force diagram and moment diagram

Figure 5-29 shows a substantial shear force which was observed between loading points B and C. when the shear force was under displacement-controlled loading conditions, causing a displacement at the loading points of 0.15 mm (0.006 in.). Moreover, the moment at these loading points is not consistent. There are stark differences between two models—one with a notch located at the center—and the other with the notch located one inch from the center. These disparities indicate the significant effects of notch placement on the resultant shear force and moment distribution.

b. Loading stages at 0.45 mm (0.018 in.)

Figure 5-30 shows the displacement at loading points of 0.45 mm (0.018 in.), which mirrors the situation encountered at the 0.15 mm loading stage (0.006 in.), where the conditions of near-zero shear force and a constant moment were not met.

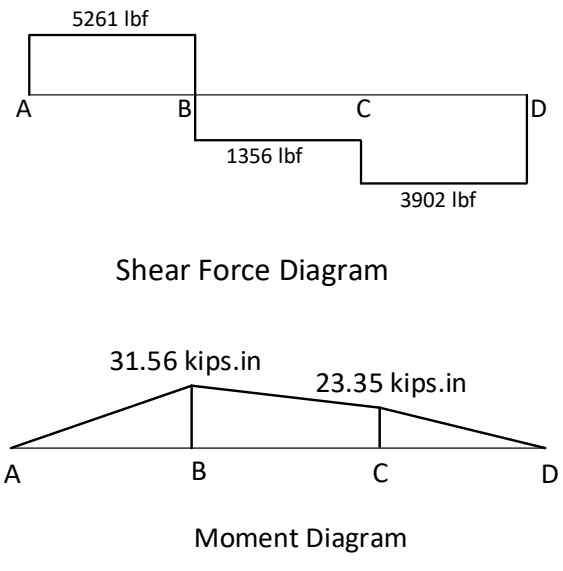

Figure 5-30 Shear force diagram and moment diagram

c. **Loading stages at 1.1 mm (0.043 in.)**

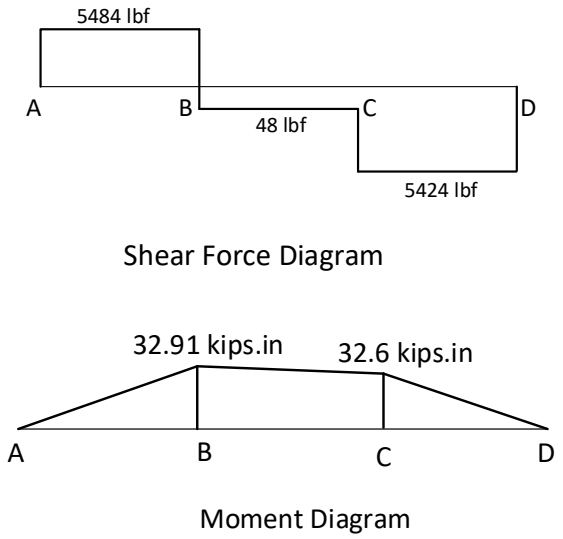

Figure 5-31 Shear force diagram and moment diagram

As shown in Figure 5-31, at the loading point displacement of B and C or loading stage of 1.1 mm (0.043 in.), the shear force between loading points B and C appears to approach zero. This indicates that despite the model with a crack initiated at one inch

from the center not initially meeting the zero-shear force criterion, a zero-shear force between the loading points was achieved as the load increased. Concurrently, the criterion of a constant moment is also satisfied at this loading stage.

d. Loading stages at 1.35 mm (0.053 in.)

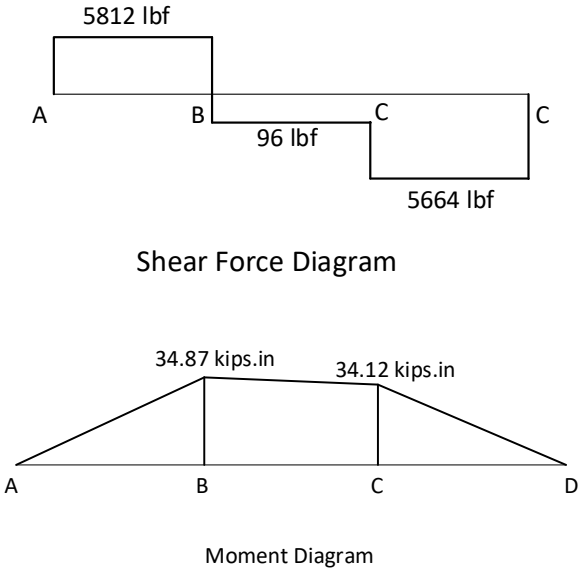

Figure 5-32 Shear force diagram and moment diagram

Figure 5-32 suggests that similar to the earlier loading stage of 0.043 inch, the present loading stage of 0.053 inch also complies with the conditions of zero shear force and a constant moment.

5.2.3.3 Model with notch 2 inches from center

In the current model, cracks are deliberately induced at 2 inches from the center of the beam using a notch. Subsequently, the relationship between load and deflection is graphed and shear force and moment are generated at various loading stages, as depicted in Figure 5-33.

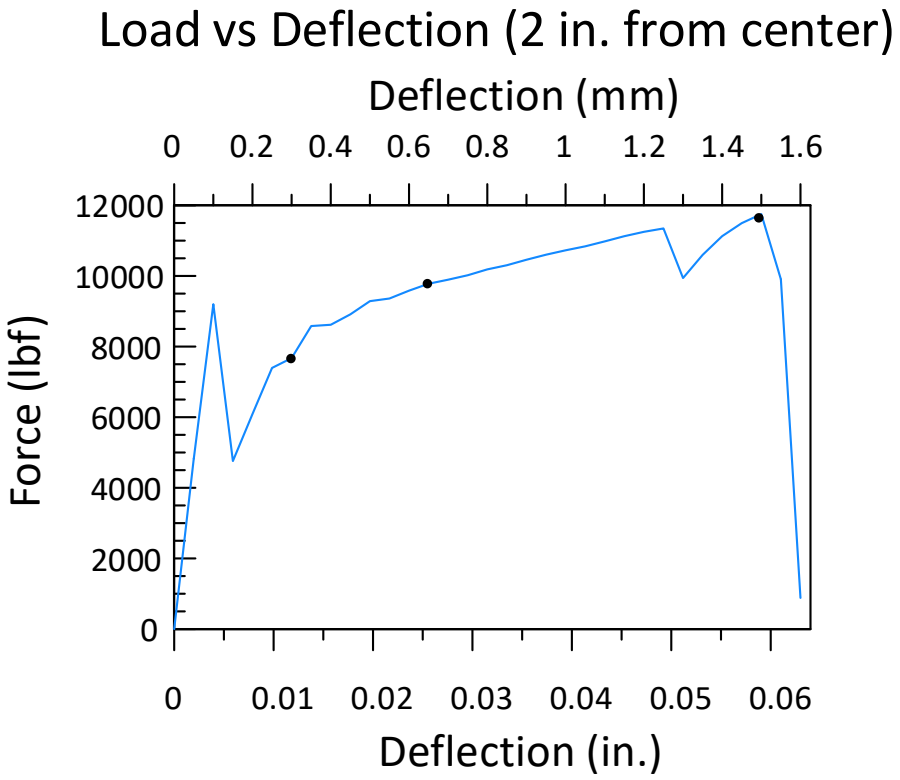

Figure 5-33 Load vs deflection graph

The shear force and moment diagrams have been derived at three arbitrarily selected locations: 1) at loading stages 0.3 mm (0.012 in.), 2) 0.65 mm (0.026 in.), and 3) 1.5 mm (0.059 in.). In this context, these loading stages correspond to the displacement of the loading points under the displacement-controlled loading condition.

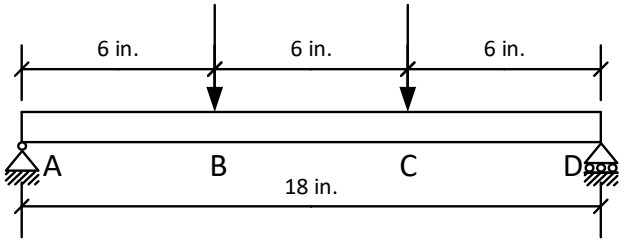

Loading stages / Reactions	0.3 mm (0.012 in.)	0.65 mm (0.026 in.)	1.5 mm (0.059 in.)
R_A	4578 lbf	5198 lbf	6055 lbf
R_B	-6051 lbf	-5802 lbf	-6408 lbf
R_C	-1615 lbf	-3972 lbf	-5354 lbf
R_D	3096 lbf	4582 lbf	5698 lbf

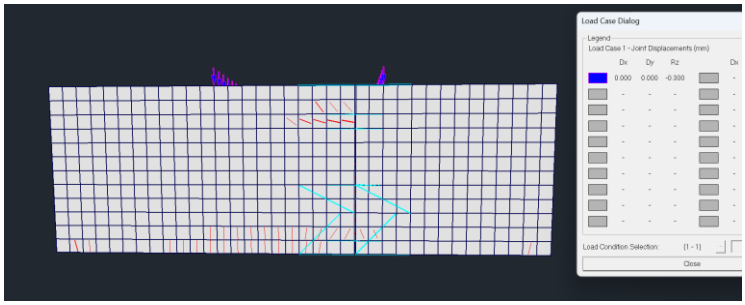

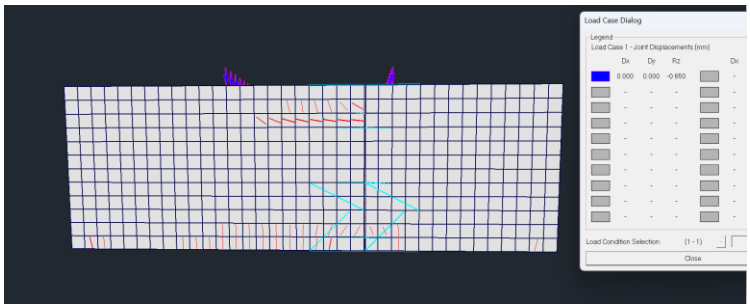

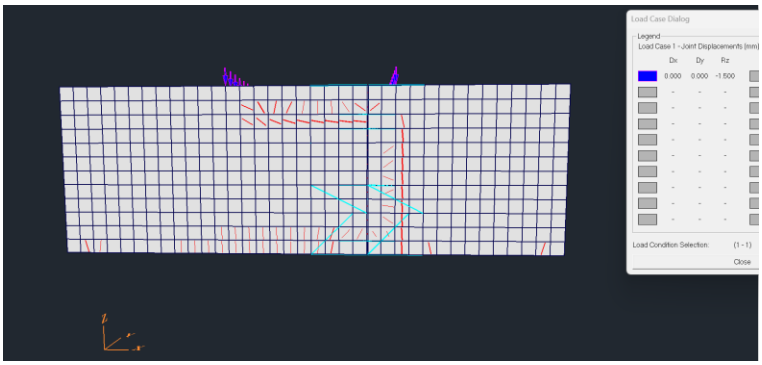

Figure 5-34 Cracking pattern at different loading stages

a. Loading stage 0.3 mm (0.012 in.)

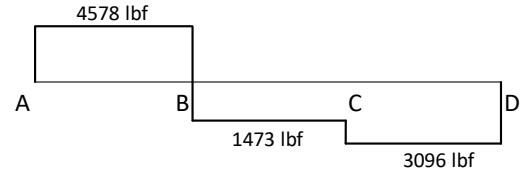

Shear Force Diagram

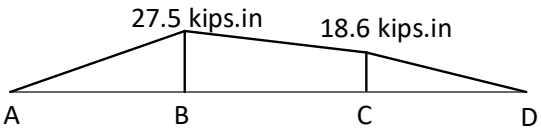

Moment Diagram

Figure 5-35 Shear force diagram and moment diagram

As illustrated in Figure 5-35, under displacement-controlled loading conditions, when the displacement at loading points B and C is 0.3 mm (0.012 in.), a substantial shear force is discernible between these points. Additionally, the moment at points B and C varies. This model affirms that unless the crack occurs precisely at the center, the conditions of zero shear force and constant moment may not be satisfied.

b. Loading Stage 0.65 mm (0.026 in.)

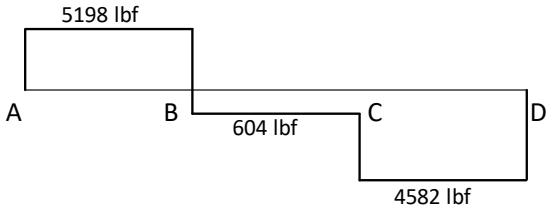

Shear Force Diagram

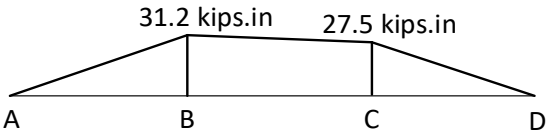

Moment Diagram

Figure 5-36 Shear force diagram and moment diagram

Figure 5-36 demonstrates that under displacement-controlled loading conditions, with the displacement at loading points B and C being 0.65 mm (0.026 in.), a significant shear force persists between these points. Nevertheless, the shear force between points B and C does begin to diminish with the increasing load. Concurrently, the condition of a constant moment cannot be incorporated into the calculations, indicating that the moment varies at these loading points.

c. Loading stage 1.5 mm (0.059 in.)

As depicted in Figure 5-37, under displacement-controlled loading conditions at the loading stage of 1.5 mm (0.059 in.), the shear force between the loading points B and C reduces. However, the shear force cannot be entirely dismissed. This is also true for the constant moment condition.

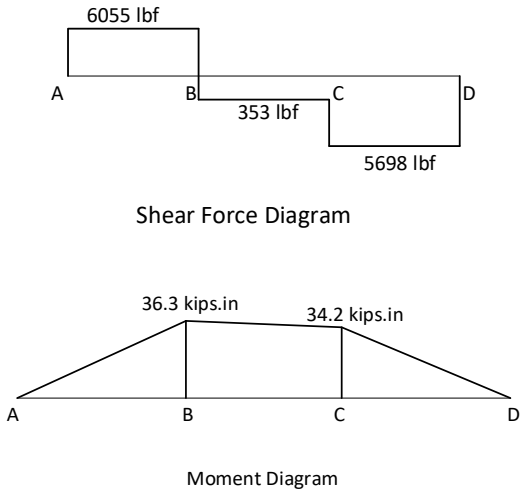

Figure 5-37 Shear force diagram and moment diagram

5.2.4 Conclusion based on FEA analysis VecTor3 model.

For the four-point ASTM beam test, four-point loading is supposed to provide a shear force moment diagram and a moment diagram as shown in Figure 5-38.

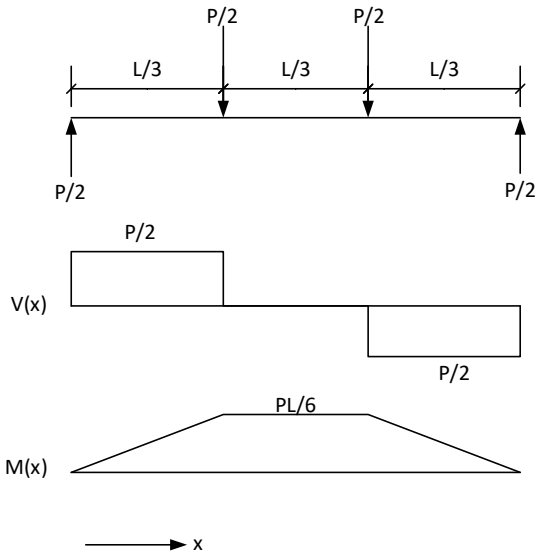

Figure 5-38 Estimated shear force diagram and moment diagram for ASTM beam testing.

However, FEA analysis reveals that during post-cracking, the shear in the central segment of the loading points does not precisely reach zero, and the moment diagram

exhibits differential values at the two loading points, B and C. When the crack is precisely centered on the ASTM beam, virtually all loading stages display an almost zero shear force, with equal moments at points B and C. However, when the crack deviates from the beam's center, manifesting instead at 1 or 2 inches away, a substantial shear force appears within the loading region.

For models where the crack occurs one or two inches from the beam's center, it is evident that as the beam edges closer to failure or as the loading increases, the shear force tends to go towards zero. Simultaneously, a constant moment diagram is observed within the loading regions at increased loading stages. This indicates that the crack initiation location significantly affects the shear force and moment characteristics of the beam under varying loading conditions.

5.3 FEM analysis using Abaqus.

ABAQUS (Abaqus v.2022) is another finite element analysis (FEA) software used for complex computational tasks across a wide range of engineering disciplines. Within the scope of this research, ABAQUS serves a crucial role in examining the strain diagram's linearity across the concrete beam's cross-section subjected to the ASTM C1609 test.

5.3.1 Concrete Model

Concrete presents a modeling challenge due to its inherent nonlinear behavior. Within the ABAQUS software, this nonlinearity is addressed using three distinct models: the concrete smeared cracking model, the concrete damaged plasticity model, and the cracking model for concrete. Of these, the concrete damaged plasticity (CDP) model is widely favored for characterizing concrete nonlinearity and analyzing associated damage.

The CDP model is a continuum and a plasticity-based damage model specifically designed for concrete. It postulates that the primary failure mechanisms in concrete are tensile cracking and compressive crushing. Utilizing the CDP model enables prediction of concrete structural behavior under diverse load conditions. In the context of beam testing, it facilitates modeling and simulation of a concrete beam's behavior under various loading scenarios. Modeling concrete beam behavior can encompass forecasting the load-deflection behavior, analyzing tracking crack propagation, and predicting the ultimate failure of the beam. Thus, the application of the CDP model within ABAQUS forms a robust analytical tool, enabling a detailed exploration of concrete behavior under complex loading conditions, thereby enhancing the understanding of its structural integrity and performance.

In this thesis analysis, a 6" x 6" x 18" beam was used with a concrete flexural strength of 40 MPa. To maintain the nonlinearity of concrete, CDP was implemented. The beam's compressive strength was 6 ksi. To preserve the beam's inherent nonlinearity, the CDP model was applied.

Table 5-6 Concrete Damaged Plasticity

Dilation angle[1] (Ψ)	Eccentricity[2] (ε)	fb_0/fc_0[3]	K[4]	Viscosity parameter[5] (μ)
40°	0.1	1.16	0.6667	0

[1] Ψ is the dilation angle measured in the *p*-*q* plane at high confining pressure, where *p* is the hydrostatic pressure stress (I_1), and *q* is the von Mises equivalent effective stress ($\sqrt{3 J_2}$).

[2] ε is eccentricity, which defines the rate at which the plastic potential function approaches the asymptote.

[3] f_{b0}/f_{c0} is the ratio of the biaxial compressive yield stress to the uniaxial compressive yield stress.

[4] *K* is the ratio of the second stress invariant (I_2) on the tensile meridian to that on the compressive meridian.

[5] μ is the viscosity parameter, which is used for the visco-plastic regularization of the concrete constitutive equation.

In this analysis, a flow potential eccentricity (ε) value of 0.1 was utilized, which is consistent with the default setting. The ratio fb_0/fc_0 was determined using the equation $fb_0/fc_0 = 1.5(fc')^{-0.075}$ as proposed by Papanikolaou and Kappos (2007). The parameter K, recommended by Seow & Swaddiwudhipong (2005) lies between 0.5 and 1, and 2/3 was selected in this study, following common practice in similar research contexts. A viscosity parameter of 0 was chosen, which is the default value. The dilation angle was set at 40°, drawing on the work of Earij et al. (2017), who, after conducting a sensitivity analysis, found negligible differences in outcomes with dilation angles of 30°, 40°, and 50°; hence, 40° was the chosen numerical simulation.

5.3.2 FEM model

The FEM analysis mainly focused on whether the 6" × 6" × 18" deep beam shows a nonlinearity in strain when visualizing a cross-sectional strain diagram based on ASTM requirements. Further analyses with different beam models were completed, and the increasing length (*L*) to depth (*d*) ratio (*L/d*) was done to see the effect of the increased *L/d* ratio on nonlinearity in the strain diagram.

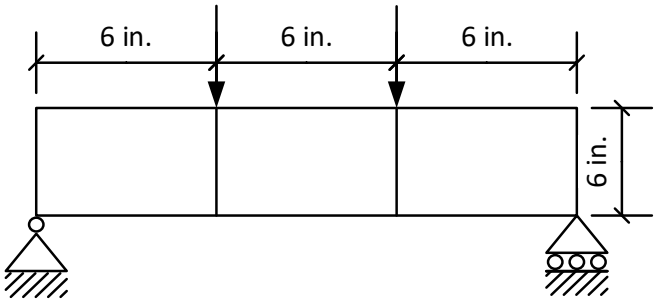

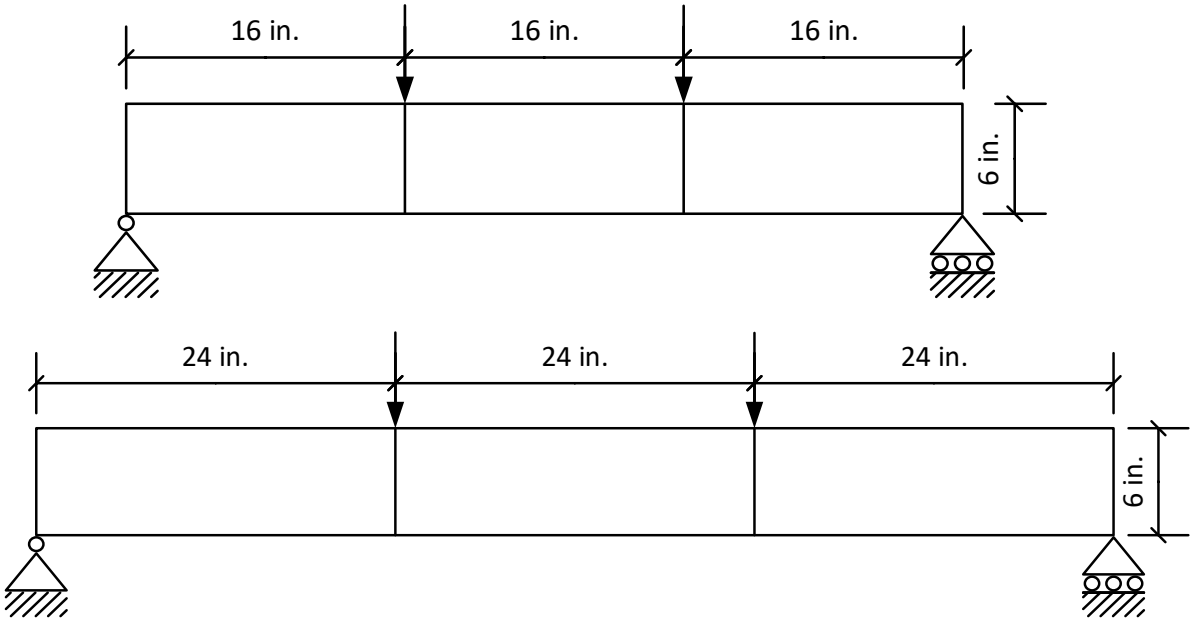

Figure 5-39 FEA model with different L/d ratio

5.3.3 Analytical Results

5.3.3.1 Model where the L/d ratio = 3

For the analysis, the ASTM beam was applied with loading on one-third of its length and the strain diagram was drawn along the cross-section of the beam.

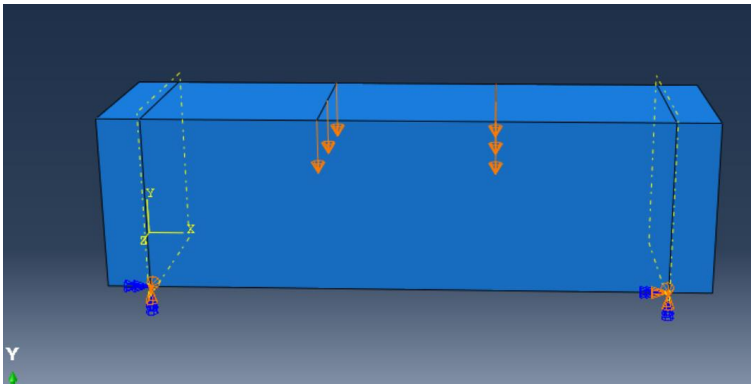

Figure 5-40 Beam with an L/d ratio of 3

In subsequent schematic illustrations, the 'load step' is defined at each progressive stage where incremental displacement at each loading point for displacement-controlled

loading is applied. Three load steps, specifically steps 9, 10, and 11, correspond to the distinct phases in the fracturing process: pre-crack, crack initiation, and post-crack, respectively. Figure 5-41 shows the maximum principal stress for these load steps.

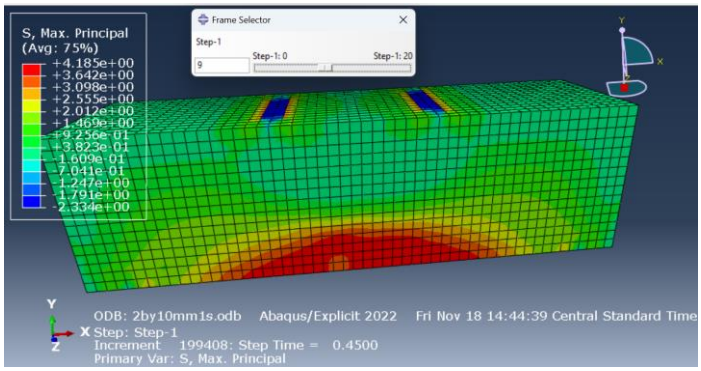

(a)

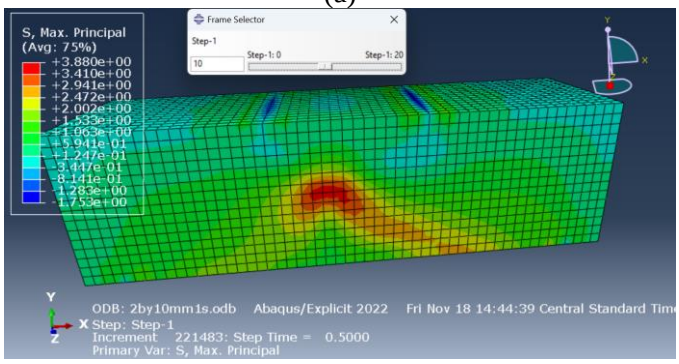

(b)

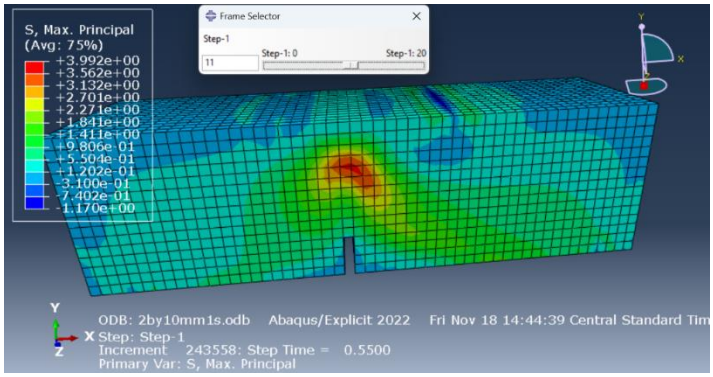

(c)

Figure 5-41 Maximum principal stress at load step: (a) Before cracking, (b) immediately before cracking, and (c) after cracking

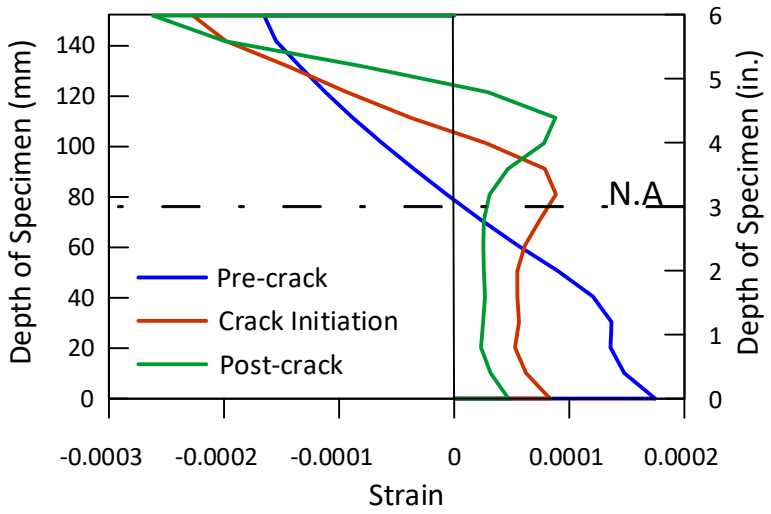

Figure 5-42 Strain Diagram measured at the center of beam (L/d=3)

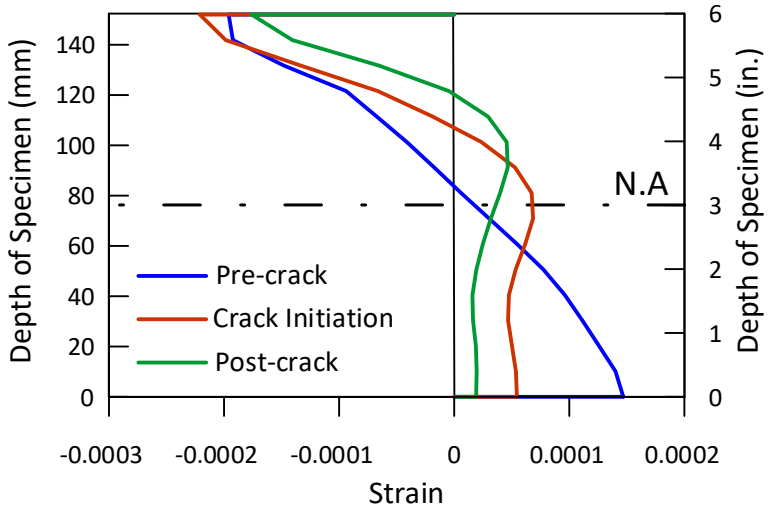

Figure 5-43 Strain diagram measured 1 in. from the center (L/d=3)

The illustrations provided in Figures 5-42 and 5-43 represent the strain profiles along the cross-section of the beam. One of these diagrams is measured at the beam's center, while the other has had one inch taken away from this central point. The depicted strain distribution hints towards a potential deviation from linearity for an ASTM C1609 beam. Such a deviation is theoretically justified due to the beam's "deep beam" categorization. This led to an expected nonlinear strain profile. This finding puts into question the existing assumptions embedded within the ASTM C1609 standard.

5.3.3.2 Model with L/d ratio=8

In this model, modifications were made to extend the beam's length, yielding a length-to-depth (*L/d*) ratio of 8. The load was strategically applied at one-third of the total beam length. The adjusted beam as well as load steps 8, 11, and 12, which correspond to the pre-crack conditions, the inception of the crack, and post-cracking, respectively. These latter load step processes represent various stages of the fracturing process.

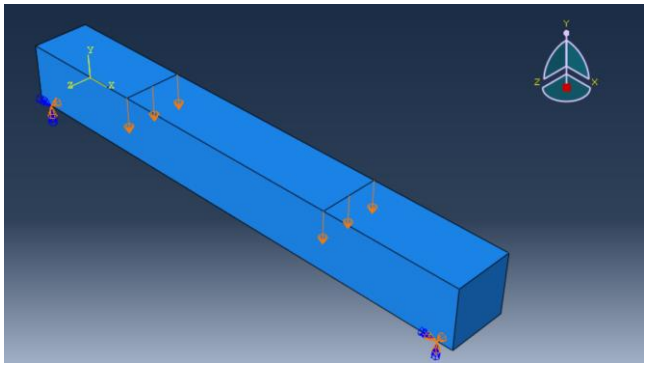

Figure 5-44 Beam with L/d ratio 8

a)

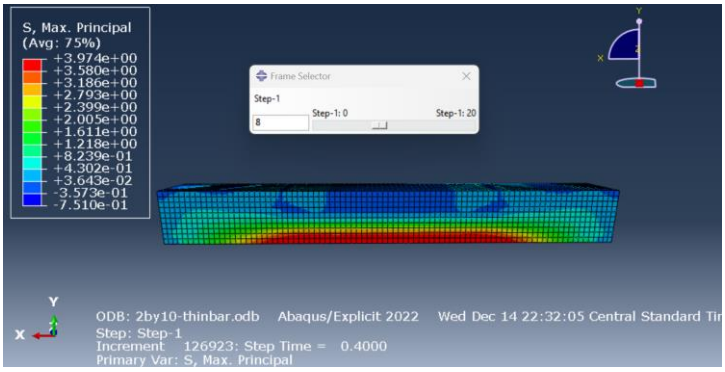

(b)

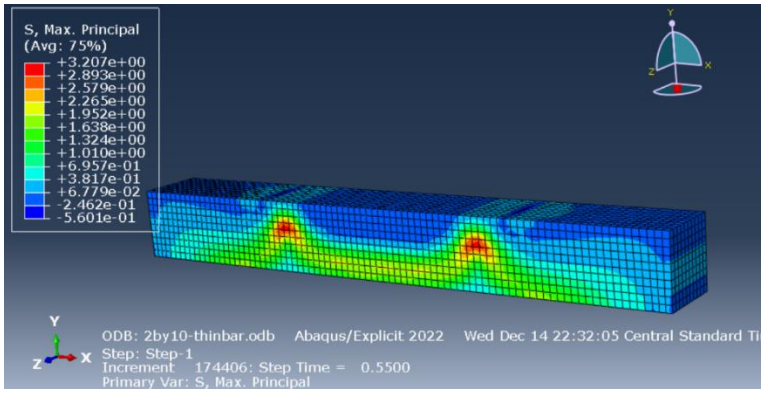

(c)

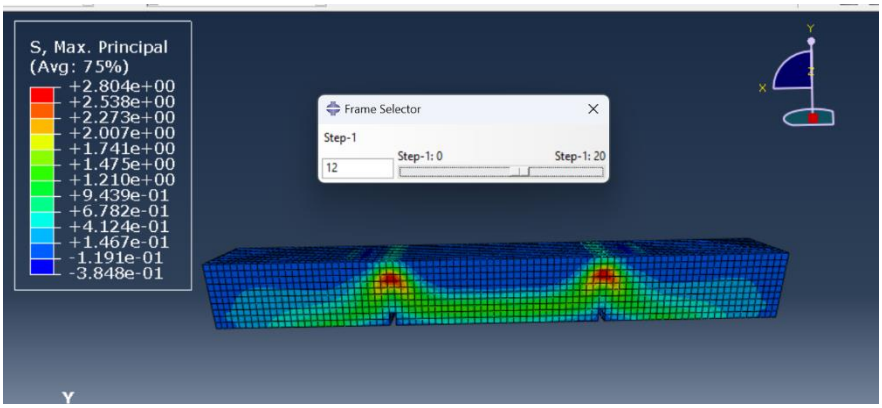

Figure 5-45 Maximum principal stress conditions of load step: (a) Before cracking, (b) immediately before cracking, and (c) after cracking

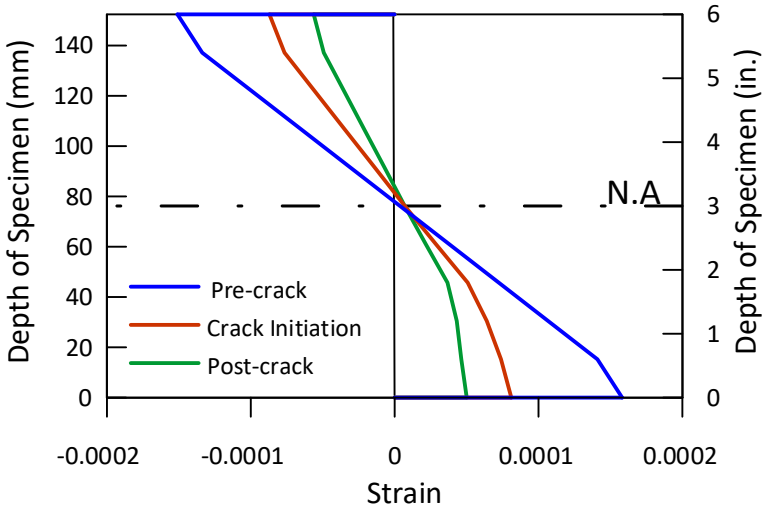

Figure 5-46 Strain diagram measured at the center (L/d=8)

Figure 5-46 shows the strain distribution becoming increasingly linear compared to the model where the length-to-depth ratio (*L/d*) equals 3. This observation substantiates the theoretical understanding that as the beam's length increases relative to its depth, the beam tends to become a more slender structure, having linear strain profile.

5.3.3.3 Model with L/d ratio=12

In this model, the length was increased for the beam such that the length-to-depth ratio would be 12 and the loading was applied to one-third of the length of beam.

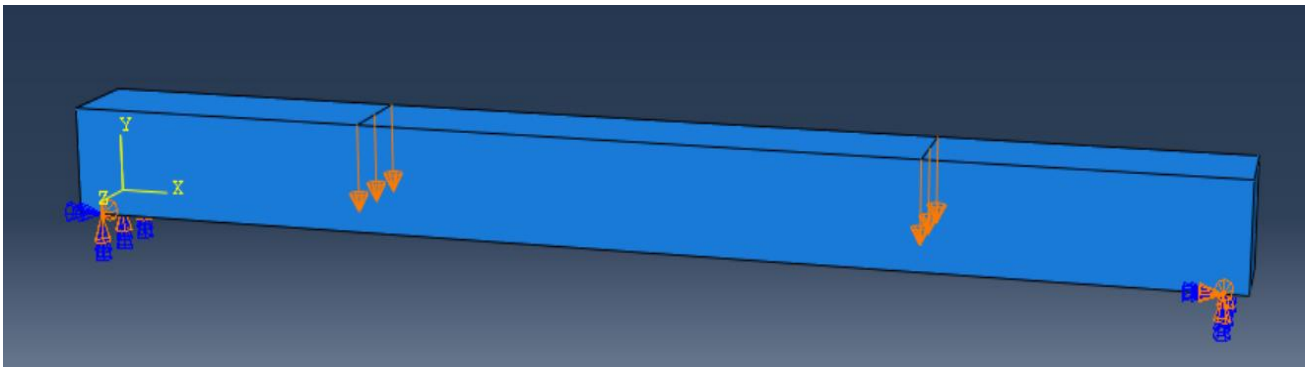

Figure 5-47 Beam with L/d ratio of 12

In this FEA analysis, load steps 10 and 14 are an important focus. These steps correspond to structural conditions before crack formation and the stage directly prior to crack initiation,

(a)

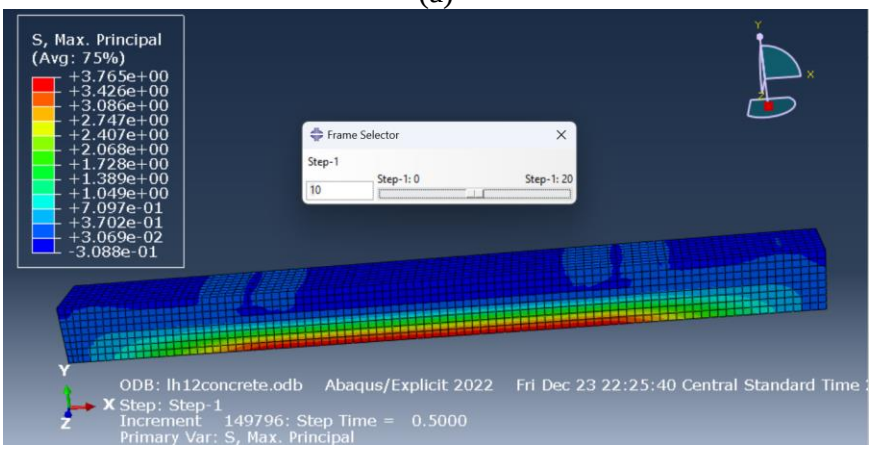

(b)

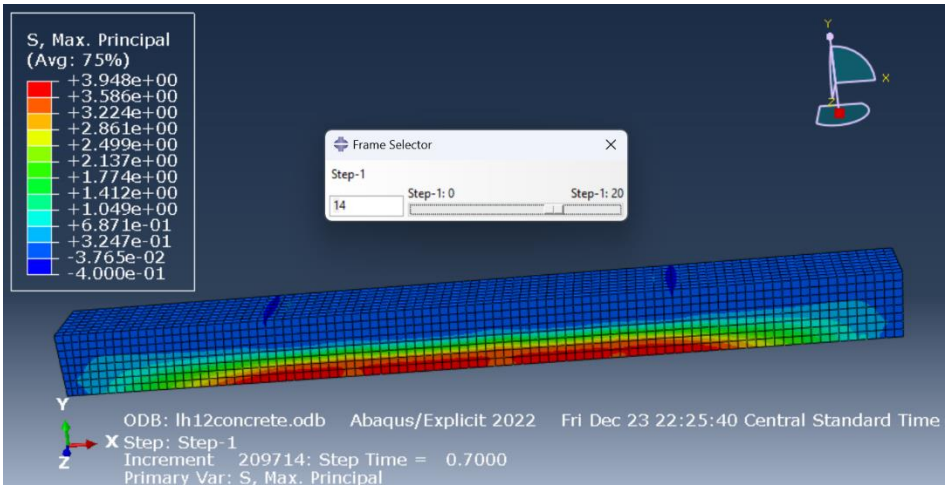

(c)

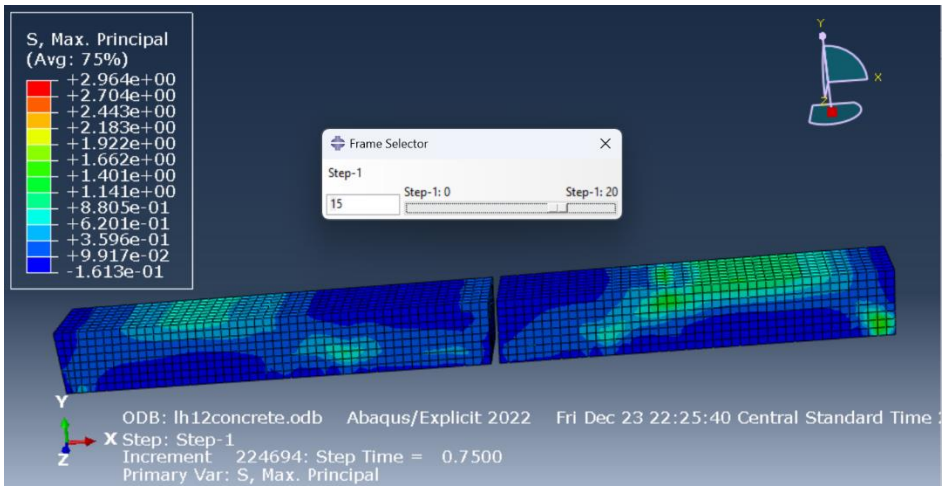

Figure 5-48 Maximum principal stress conditions of load step: (a) before cracking, (b) immediately before cracking, and (c) after cracking

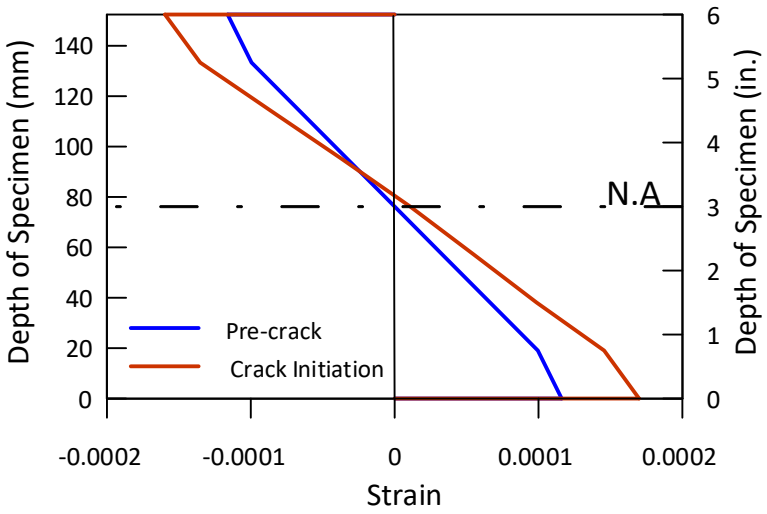

Figure 5-49 Strain diagram measured at the center (L/d=12)

The strain profile increasingly aligns with a linear pattern as the ratio of length to depth (L/d) of the beam escalates. This trend suggests that larger L/d ratios contribute to a more linear strain distribution within the beam.

5.3.4 Comparison of beams with different L/d ratios

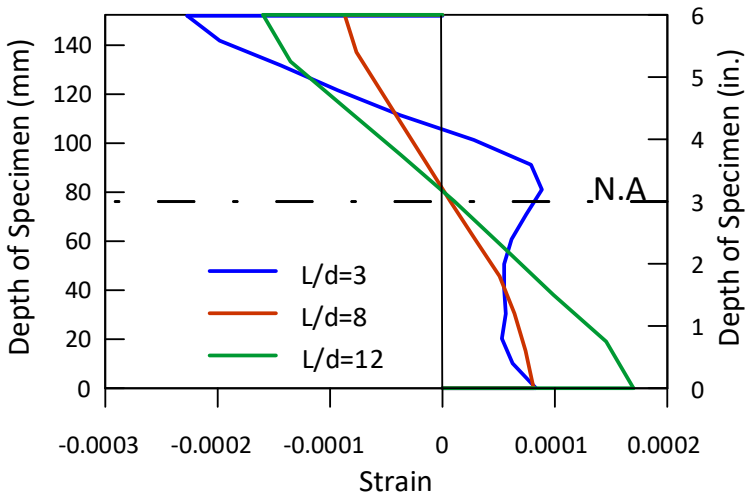

Figure 5-50 Combined strain diagram just before cracking for specimen with a different L/d ratio.

As demonstrated in Figure 5-50, superimposing strain diagrams from distinct Abaqus models elucidate the nonlinearity of the strain profile for the ASTM tested standard beam. Furthermore, it becomes evident that the strain distribution progressively approximates linearity as the length-to-depth ratio (*L/d* ratio) increases. This suggests that the structural behavior of the beam alters with changing *L/d* ratios, thereby progressing towards linearity with increased ratios.

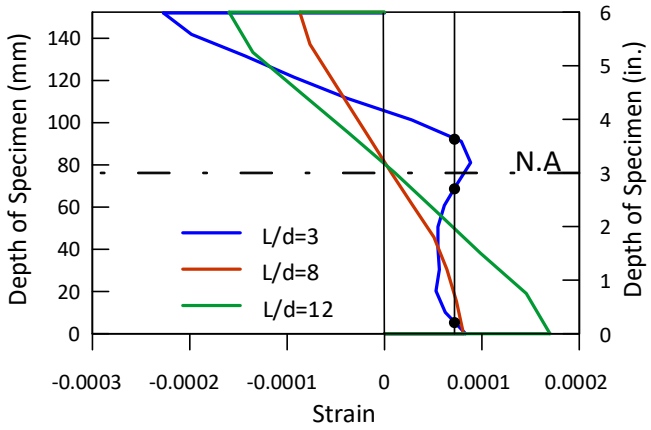

Figure 5-51 Graph showing nonlinearity of strain diagram for ASTM C1609 tested beam.

In Figure 5-51, a straight vertical line is drawn at arbitrary strain values. It is noticeable that for the graph where *L/d* equals 3, the line intersects with three distinct points, all exhibiting the same strain values. This observation stands in contrast with the more linear graphs corresponding to *L/d* ratios of 8 and 12, where the line intersects at just a single point.

The process of generating a stress-strain curve for the tensile response from the flexural beam test, as per the ASTM C1609, requires back calculation, as detailed in the literature review section. This calculation is founded on the basic assumption of a linear strain graph and a one-to-one stress to strain relationship.

However, the results demonstrated in the figure challenge this assumption, as multiple points of the same strain along the cross-section are evident for the graph where *L/d* equals 3. This discrepancy has potential problems for ensuring the accuracy of the stress-strain curve, and consequently, it affects actual tensile response results obtained from the flexural beam test.

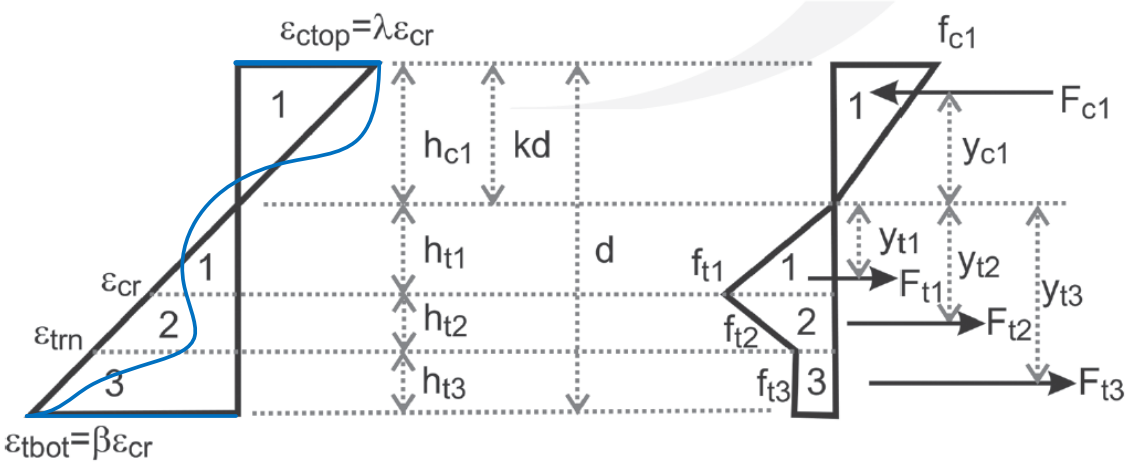

Figure 5-52 Nonlinear strain diagram along the cross-section

When the strain exhibits a nonlinear pattern, we lose the one-to-one correspondence typically expected between stress and strain. Therefore, we calculate ε_{cr} and f_{t1} under the presumption of a linear pre-cracking relationship. However, when it comes to locating ε_{trn} to derive f_{t2}, the task becomes problematic because the strain relationship is not linear, and consequently, ε_{trn} cannot be precisely located along the beam's depth.

Furthermore, the nonlinear strain distribution might result in multiple points along the beam's cross-section exhibiting the same strain value. This creates a challenge in finding the corresponding stress values and could lead to an inaccurate stress-strain curve.

5.3.5 Summary of Abaqus Model Calculations

A critical evaluation of the graphs presented herein reveals that the strain profiles for the 6"× 6" × 6" ASTM tested beams exhibited nonlinearity. This characteristic is in direct contradiction to the presuppositions intrinsic to the ASTM standard's formulation for flexural testing, which assumes a linear strain distribution.

Further scrutiny of the graphs brings to light a trend: As the ratio between the beam's length and depth increases, the strain diagram approximates a more linear pattern. This highlights the potential need for reevaluating the foundational assumptions of ASTM standards in the context of beams with differing length-to-depth ratios.

6 CONCLUSION AND RECOMMENDATIONS

1. Comparative analysis of fibers in UHPC

In this research, the tensile performance of UHPC with high-strength hooked fibers was compared with that of high-strength straight smooth microfibers.

- The UHPC containing high-strength hooked fibers surpassed its straight steel microfiber counterpart in tensile response. This was evident across all testing methods, including the direct tensile test (DTT), double-punch test (DPT), and ASTM C1609 test.
- The single fiber pullout test demonstrated that high-strength hooked fibers exhibit slip-hardening behavior while being pulled out from UHPC. This bonding characteristic is favorable, as it leads to improved strain-hardening properties in composite tensile behavior for UHPC components and contributes to achieving their tensile ductility.
- While performing a direct tensile test (DTT), UHPC with high-strength hooked fibers demonstrated a superior tensile strain capacity, with peak stress-strain ranging from 0.3% to 0.6%, compared to the 0.1% to 0.4% observed in straight microfibers. This superior tensile strain capacity can be utilized to enhance the nominal bending capacity of the UHPC structure and improve ductility.

2. Comparison evaluation of UHPC tensile testing methods

- For direct tensile test (DTT), the average COV for peak stress across all specimens was found to be 6.8%. While the specimens examined in this investigation displayed lower COVs, existing literature has pointed out high COVs for the DTT method. This highlights the need for additional research to validate the results obtained through the DTT method.
- For ASTM C1609 test, the average COVs at the peak load for all specimens at peak load was 15.75%, and the graph for force vs deflection was also scattered and inconsistent.
- For double-punch test (DPT), the average COVs for peak stress was 6.37%, lower than that of ASTM C1609. DPT is shown to be a consistent tensile test method.
- While DPT consistently yielded reliable tensile results, a significant operational challenge lies in the labor-intensive process of cutting 6"×12" cylinders into 6"×6" cylinders and ensuring the specimens are level and uniform. In pursuit of operational efficiency, two specimen preparation techniques were compared: one involving cutting a cylinder in half and another using a direct 6" × 6" mold (mold cut in half). Notably, specimens from the 6" × 6" mold exhibited enhanced consistency, reflected in a reduced COV of 3.8%. The peak stress measurements between the two approaches were largely congruent, registering 0.58 ksi for cut specimens and 0.55 ksi for those prepared from the halved mold.

3. Analysis of UHPC properties: Flowability and Compressive strength

i. Flowability

One of UHPC's defining characteristics is its flowability, especially pertinent given that its water-to-cement (w/cm) ratio is less than 0.2. An investigation on enhancing flowability was undertaken. It involved keeping the silica fume replacement level constant across all samples, with the only variable being the purity grades of the silica fume based on their silicon dioxide (SiO_2) content.

- Results indicated that the purity of silica fume plays a pivotal role in influencing UHPC's flowability. Specifically, a 94% purity level outstripped the 92% and 97% purity levels in terms of higher flowability.
- It is crucial to note that these findings are preliminary and necessitate additional research for comprehensive understanding and validation.

ii. Compressive strength

Compressive strength is an important metric for UHPC, with the material anticipated to possess a strength of approximately 22 ksi.

- However, the mix developed in this study demonstrated strength around 18 ksi, hinting at a need for optimization. Since high temperature allows for the pozzolanic reaction of silica fume, heat treatment with sufficient humidity condition was provided for the UHPC mix. The best results in enhancing the compressive strength of the UHPC mix were achieved with heat treatment involving a 90-degree oven temperature and 24-hour delay time.

4. Analytical Investigation

ASTM C1609 beam test is widely used as indirect tensile test method for assessing the tensile response of the UHPC. However, ASTM C1609 beam test has some problematic assumptions, like zero shear, constant moment condition in the loading region, and linear strain distribution. These assumptions were analyzed using finite element software, and the following conclusions were derived.

- According to ACI 318, the D-region is defined as an area with load or geometric irregularities that extend to a distance roughly equivalent to the depth of the structural element, exhibiting a non-linear strain distribution. Therefore, the specific area of interest within the ASTM C1609 test corresponds to a D-region characterized by a non-linear strain distribution. Furthermore, the ASTM C1609 beam possesses a length-to-depth ratio (L/d ratio) of 3, which is below the L/d ratio of 4 specified as the ACI criteria for a slender beam. As a result, the ASTM test cannot be considered a purely flexural test, as its performance is primarily influenced by shear behavior in accordance with ACI 318 (2019) and AASHTO LRFD Specifications (2020). Consequently, one of the foundational assumptions of flexural behavior, linear strain distribution, does not hold for the ASTM C1609 test. Finite element analysis reaffirms this observation, showing non-linear strain distribution across the beam's cross-section for the specified L/d ratio.
- The ASTM C1609 test is categorized as an indirect tensile test, which necessitates the utilization of a back-calculation method to produce a tensile stress-strain relation of an FRC material. This complexity arises when faced with a non-linear strain distribution. The finite element model identified several positions along the

height of the beam where identical strain values were recorded. This contravenes the fundamental assumption of a linear strain distribution along the height of a slender beam, and consequently results in inaccurate tensile stress-strain relationships for FRC materials when derived through the ASTM C1609 method.

- The most important characteristic of FRC materials lies in their post-cracking behavior. The response of the ASTM C1609 beam is typically governed by a single dominant crack in the case of FRC with low fiber dosage or UHPC characterized by exceptionally high strength. By utilizing nonlinear finite element modeling with the single crack at different locations, the limitations in the assumptions of ASTM C1609 were assessed. The assumptions of zero-shear and constant moment remain applicable solely to a model featuring a centrally positioned crack. However, these assumptions are no longer valid when cracks are away from the center. This discrepancy arises due to forces redistribution themselves towards stiffer portion of the beam (located away from the crack) after the dominating crack develops.

REFERENCES

AASHTO. *LRFD Bridge Design Specifications*. American Association of State Highway and Transportation Officials (AASHTO), Washington, D.C., Standard 9th Edition, 2020.

Abbas, Y. M., & Khan, M. I. (2016). Fiber–Matrix Interactions in Fiber-Reinforced Concrete: A Review. *Arabian Journal for Science and Engineering*, *41*(4), 1183–1198.

Abdel-Nasser, A., Sharaf, T., Ghatass, H., & Abdel-Galil, E. (2017). Analysis of Reinforced Concrete Deep Beams Using Nonlinear Strain Model. *Port Said Engineering Research Journal*, 21(2), 231-240, DOI: 10.21608/PSERJ.2017.3332.

ACI 318-19. (2019). Building code requirements for structural concrete: (ACI 318-19) and commentary (ACI 318R-19). *ACI Committee 318*. Available at 318-19_preview.pdf (concrete.org).

ACI Committee 239 (2018) "Ultra-High-Performance Concrete: An Emerging Technology Report (ACI 239R-18)," American Concrete Institute, Farmington Hills, MI, 2018, 21 pages

ACI 239 Committee in Ultra-High Performance Concrete, "Minutes of Committee Meeting, October 2012," *ACI Annual Conference 2012*,, Toronto, ON, Canada ACI Committee 239, "Ultra-High-Performance Concrete: An Emerging Technology Report (ACI 239R-18)," American Concrete Institute, Farmington Hills, MI, 2018, 21 pp

Aghdasi, P., Heid, A. E., & Chao, S.-H. (2016a). Developing Ultra-High-Performance Fiber-Reinforced Concrete for Large-Scale Structural Applications. *ACI Materials Journal*, *113*(5).

Aghdasi, P., Heid, A. E., & Chao, S.-H. (2016b). Developing Ultra-High-Performance Fiber-Reinforced Concrete for Large-Scale Structural Applications. *ACI Materials Journal*, *113*(5).

Aghdasi, P., Palacios, G., Heid, A. E., & Chao, S. (2015). *Mechanical Properties of a Highly flowable Ultra-High-Performance Fiber-Reinforced Concrete Mixture Considering Large-Size Effects*.

ASTM C1240-20. (2020). Standard Specification for Silica Fume Used in Cementitious Mixtures. *ASTM International*.

ASTM C1437-20. (2020). Test Method for Flow of Hydraulic Cement Mortar. *ASTM International*.

ASTM C1609/C1609M-19a. (2019). Standard Test Method for Flexural Performance of Fiber-Reinforced Concrete (Using Beam With Third-Point Loading). *ASTM International*.

Azmee, N., & Shafiq, N. (2018). Ultra-high performance concrete: From fundamental to applications. *Case Studies in Construction Materials*, *9*.

Carey, A. S., Howard, I. L., & Shannon, J. (2022). Effects of Silica Fume Purity on Behavior of Ultra-High Performance Concrete. *Advances in Civil Engineering Materials*, *11*(1).

Chao, S., Kaka, V., & Shamshiri, M. (2019). Toward A Non-Prestressed Precast Long-Span Bridge Girder Using UHP-FRC. *International Interactive Symposium on Ultra-High Performance Concrete*, *2*(1).

Chao, S., Shamshiri, M., Liu, X., Palacios, G., Schultz, A., & Nojavan, A. (2021). Seismically Robust Ultra-High-Performance Fiber- Reinforced Concrete Columns. *ACI Structural Journal*, *118*(2).

Chao, S.-H., Cho, J.-S., Karki, N. B., Sahoo, D. R., & Yazdani, N. (2011). FRC performance comparison: uniaxial direct tensile test, third-point bending test, and round panel test. *Special Publication*, *276*, 1–20.

Chao, S.-H., Kaka, V., Palacios, G., Kim, J., Choi, Y.-J., Aghdasi, P., Nojavan, A., & Schultz, A. (2016). Seismic Behavior of Ultra-High-Performance Fiber-Reinforced Concrete Moment Frame Members. International Interactive Symposium on Ultra-High Performance Concrete, 1(1).

Choi, Y. &. Yuan, R. L. (2005). Experimental relationship between splitting tensile strength and compressive strength of GFRC and PFRC, Cement and Concrete Research, 35(8,) Pages 1587-1591, ISSN 0008-8846, DOI:10.1016/j.cemconres.2004.09.010. (https://www.sciencedirect.com/science/article/pii/S000888460400417X)

Cunha, V., Barros, J., & Sena-Cruz, J. (2010). Pullout behavior of hooked-end steel fibres in self-compacting concrete. 22.

Earij, A., Alfano, G., Cashell, K., & Zhou, X. (2017). Nonlinear three–dimensional finite–element modelling of reinforced–concrete beams: Computational challenges and experimental validation. *Engineering Failure Analysis*, *82*, 92–115, DOI:10.1016/j.engfailanal.2017.08.025

El-Tawil, S., Alkaysi, M., Naaman, A. E., Hansen, W., & Liu, Z. (2016). Development, Characterization and Applications of a Non Proprietary Ultra High Performance Concrete for Highway Bridges. *Department of Civil and Environmental Engineering University of Michigan*, 60.

Graybeal, B. A. & Baby, F. (2013). Development of Direct Tension Test Method for Ultra-High-Performance Fiber-Reinforced Concrete. In *ACI Materials Journal* (Vol. 110, Issue

2). Available at https://highways.dot.gov/sites/fhwa.dot.gov/files/docs/research/research-programs/infrastructure/1771/f110-m17.pdf.

Graybeal, B. A. (2014a) "Design and Construction of Field-Cast UHPC Connections." FHWA-HRT-14- 084. Contains FHWA ACI Committee 239, "Ultra-High-Performance Concrete: An Emerging Technology Report (ACI 239R-18)," American Concrete Institute, Farmington Hills, MI, 2018, 21 pp of UHPC

Graybeal, B. A. & Baby, F. (2019)*: Tension Testing of Ultra-High Performance Concrete*. Report No. FHWA-HRT-17-053, available at https://www.fhwa.dot.gov/publications/research/infrastructure/structures/bridge/17053/17053.pdf

Haber, Z. B., De la Varga, I., Graybeal, B. A., Nakashoji, B., & El-Helou, R. (2018). *Properties and behavior of UHPC-class materials*. Office of Infrastructure Research and Development, U.S. Federal Highway Administration, Report No. FHWA-HRT-18-036, a Final Report covering 2014-2017, 153 pages, available at https://www.fhwa.dot.gov/publications/research/infrastructure/structures/bridge/18036/18036.pdf.

Hanson, K. (2017). SCMs in Concrete: Silica Fume, *Precast, Inc.* an online National Precast Concrete Association (NCP) magazine, July-August 2017 issue, available at SCMs in Concrete: Silica Fume (precast.org)

JSCE. (2008). *Recommendations for Design and Construction of High Performance Fiber Reinforced Cement Composites with Multiple Fine Cracks (HPFRCC)*.

Kaka, V., Kim, J., & Chao, S.-H. (2016). *Formulating Constitutive Stress-Strain Relations for Flexural Design of Ultra High-Performance Fiber-Reinforced Concrete*. https://doi.org/10.21838/uhpc.2016.46

Kaka, V. B., Laskoski, C.D., Bell, B., & Chao, S.-H. (2016). UHP-FRC for Architectural Structural Columns with Non-Euclidean Geometries. *Proc., First International Interactive Symposium on UHPC*, https://doi.org/10.21838/uhpc.2016.78, available as pdf at Microsoft Word - UHP-FRC for Architectural Structural Columns with Non-Euclidean Geometries-6.docx (iastatedigitalpress.com)

Karmacharya, A. & Chao, S.-H. (2019). Precast Ultra-High-Performance Fiber-Reinforced Concrete (UHP-FRC) for Fast and Sustainable Pavement Repair. *Proc., MATEC Web Conferences*, **271**, 1004. *TranSET* 2019, DOI:10.1051/matecconf/201927101004, Available as pdf at Precast Ultra-High-Performance Fiber-Reinforced Concrete (UHP-FRC) for Fast and Sustainable Pavement Repair (semanticscholar.org)

Karmacharya, A., Shahandashti, M., & Chao, S. (2023). Full-Depth Rapid Repair of Airfield Rigid Pavements with Ultra-High-Performance Fiber- Reinforced Concrete Precast Panels (UHP-FRC-PCP) and Life-Cycle Cost Analysis, *Proc., International Interactive Symposium on Ultra-High Performance Concrete*, DOI:10.21838/uhpc.16716.

Li, Z., Zhou, X., Ma, H., & Hou, D. (2022). *Advanced Concrete Technology*. Wiley.

Liao, W.-C., Chen, P.-S., Hung, C.-W., & Wagh, S. K. (2020). An Innovative Test Method for Tensile Strength of Concrete by Applying the Strut-and-Tie Methodology. *Materials*, *13*.

Naaman, A., Fischer, G., & Krstulovic, N. (2006). *Measurement of Properties of Fiber Reinforced Concrete: ACI Committee 544 on Fiber Reinforced Concrete*.

Naaman, A. E., Namur, G. G., Alwan, J. M., & Najm, H. S. (1991). Fiber pullout and bond slip. I: Analytical study. *Journal of Structural Engineering (United States)*, *117*(9), 2769-2790. https://doi.org/10.1061/(ASCE)0733-9445(1991)117:9(2769)

Nematollahi, B., Saifulnaz, M. R., Jaafar, S., & Voo, Y. L. (2012). A review on ultra high performance 'ductile' concrete (UHPdC) technology. *International Journal of Civil & Structural Engineering*, *2*(3), 1003-1018.

Nguyen, D., Ryu, G. S., Koh, K. T., & Kim, D.-J. (2014). Size and geometry dependent tensile behavior of ultra-high-performance fiber-reinforced concrete. *Composites Part B-Engineering*, *58*, 279–292.

Nilson, A., Darwin, D., & Dolan, C. (2010). *Design of Concrete Structures*. McGraw-Hill Education.

Papanikolaou, V. K. & Kappos, A. J. (2007). Confinement-sensitive plasticity constitutive model for concrete in triaxial compression. *International Journal of Solids and Structures*, *44*(21), 7021–7048, DOI:10.1016/j.ijsolstr.2007.03.022, pdf available at https://www.sciencedirect.com/science/article/pii/S0020768307001783.

Park, J. S., Kim, Y. J., Cho, J. R., & Jeon, S. J. (2015). Early-Age Strength of Ultra-High-Performance Concrete in Various Curing Conditions. *Materials (Basel, Switzerland)*, *8*(8), 5537–5553. https://doi.org/10.3390/ma8085261

Qi, J., Ma, Z. J., Wang, J., & Liu, T. (2016). Post-cracking shear strength and deformability of HSS-UHPFRC beams. *Structural Concrete*, *17*(6), 1033–1046.

Qi, J., Wang, J., & Ma, Z. (2018). Flexural response of high-strength steel-ultra-high-performance fiber reinforced concrete beams based on a mesoscale constitutive model: Experiment and theory. *Structural Concrete*, *19*, 719–734.

Qiao, P., & Zhou, Z. (2018). Direct Tension Test for Characterization of Tensile Behavior of Ultra-High Performance Concrete. *Journal of Testing and Evaluation*.

Qiu, M., Shao, X., Zhu, Y., Hussein, H. H., Li, F., & Li, X. (2022). Effect of Aspect Ratios of Hooked End and Straight Steel Fibers on the Tensile Strength of UHPFRC. *Journal of Materials in Civil Engineering*, *34*(7), 04022131.

Ramezanianpour, A. A., Kazemian, A., Nikravan, M., Mahpur, A., & Moghadam, M. A. (2013). Influence of a low-activity slag and silica fume on the fresh properties and durability of high performance self-consolidating concrete. *Proceedings of 3rd International Conference on Sustainable Construction Materials and Technologies*. Available at http://www.claisse.info/2013%20papers/data/e386.pdf.

Saleh, M. J., & Voo, Y. L. (2012). A review on ultra-high performance "ductile" concrete (UHPdC) technology. *International Journal of Civil and Structural Engineering*, *2*, 1003–1018.

Seow, P. E. C., & Swaddiwudhipong, S. (2005). Failure Surface for Concrete under Multiaxial Load—a Unified Approach. *Journal of Materials in Civil Engineering*, *17*, 219–228. DOI: 10.1061/(ASCE)0899-1561(2005)17:2(219)

Smith, M. (2014). *ABAQUS/Standard User's Manual, Version 6.14*. Dassault Systèmes Simulia Corp.

Soranakom, C. & Mobasher, B. (2008). Correlation of tensile and flexural responses of strain softening and strain hardening cement composites. *Cement and Concrete Composites*, 30(6), 465–477, DOI: 10.1016/j.cemconcomp.2008.01.007

Tai, Y. S., & El-Tawil, S. (2020). Effect of component materials and mixing protocol on the short-term performance of generic ultra-high-performance concrete. *Construction and Building Materials, 238*.

Tao, Z., Wang, Z.-B., & Yu, Q. (2013). Finite element modelling of concrete-filled steel stub columns under axial compression. *Journal of Constructional Steel Research, 89*, 121–131.

Trumbauer, B. E. & Chen, W.-F. (1971). Double-punch test and tensile strength of concrete. *Fritz Laboratory Reports,* Paper 2026. Full text available at http://preserve.lehigh.edu/engr-civil-environmental-fritz-lab-reports/2026.

Tuladhar S. & Chao, S.-H. (2019). A simple tensile testing method for UHP-FRC based on double-punch test. *International Interactive Symposium on Ultra-High Performance Concrete, 2*(1), DOI: 10.21838/uhpc.9662

Vecchio, F.J., Hrynyk, T.D., Guner, S., Sadeghian, V., Ferche, A., Yap, B.,

(2019) VecTor3, available at http://vectoranalysisgroup.com/vector3.html.

Venkatesh, K. & Chao, S.-H. (2018). *Investigation of Eliminating Prestress in Bridge Girders with the Use of Non-Prestressed Ultra-High-Performance Fiber-Reinforced Concrete Girders*. Investigation of Eliminating Prestress in Bridge Girders with the Use of Non-Prestressed Ultra-High-Performance Fiber-Reinforced Concrete Girders | Proceedings | Vol , No (ascelibrary.org)

Villavicencio, T., & Sebastian, E. (2021). Experimental and Analytical Investigation of UHPC Tensile Strength Behavior. In *ProQuest Dissertations and Theses*.

Wang, T., & Hsu, T. T. C. (2001). Nonlinear finite element analysis of concrete structures using new constitutive models. *Computers & Structures, 79*(32), 2781–2791.

Wille, K. & Boisvert-Cotulio, C. (2013). *Development of Non-Proprietary Ultra-High Performance Concrete for Use in The Highway Bridge Sector*, U.S. Federal Highway Administration, Report Number : FHWA-HRT-13-100. Accessed 07/14/2023; pdf is available at https://ntrl.ntis.gov/NTRL/dashboard/searchResults/titleDetail/PB2013110587.xhtml

Wille, K., El-Tawil, S., & Naaman, A. (2014). Properties of strain hardening ultra-high performance fiber reinforced concrete (UHP-FRC) under direct tensile loading. *Cement and Concrete Composites*, *48*, 53–66.

Wille, K., Kim, D. J., & Naaman, A. E. (2011). Strain-hardening UHP-FRC with low fiber contents. *Materials and Structures*, *44*(3), 583–598.

Wille, K., & Naaman, A. (2012). Pullout Behavior of High-Strength Steel Fibers Embedded in Ultra-High-Performance Concrete. *ACI Materials Journal*, *109*(4).

Wille, K., Naaman, A. E., & Parra-Montesinos, G. J. (2011). Ultra-high performance Concrete with compressive strength exceeding 150 MPa (22 ksi): A simpler way. *ACI Materials Journal*, *108*(1).

Wille, K., Naaman, A., & El-Tawil, S. (2011). Optimizing ultra-high-performance fiber-reinforced concrete. *Concrete International*, *33*, 35–41.

Wu, Z., Shi, C., He, W., & Wu, L. (2016). Effects of steel fiber content and shape on mechanical properties of ultra high performance concrete. *Construction and Building Materials*, *103*.

Yoo, D.-Y., Park, J.-J., & Kim, S.-W. (2017). Fiber pullout behavior of HPFRCC: Effects of matrix strength and fiber type. *Composite Structures*, *174*, 263–276.

Zhang, H., Ji, T., Zeng, X., Yang, Z., Lin, X., & Liang, Y. (2018). Mechanical behavior of ultra-high performance concrete (UHPC) using recycled fine aggregate cured under different conditions and the mechanism based on integrated microstructural parameters. *Construction and Building Materials*, *192*, 489–507.

Zheng, W., Kwan, A. K. H., & Lee, P. K. K. (2001). Direct tension test of concrete. *Materials*, *98*, 63–71.